CHAPTER 20

NMR Spectroscopy of Polymers

Alan E. Tonelli* and Jeffery L. White†

*Fiber & Polymer Science Program, North Carolina State University, Raleigh, NC 27695
†Department of Chemistry, Oklahoma State University

20.1 INTRODUCTION

Nuclei of all atoms possess charge and mass, and fortunately some have angular momentum and a magnetic moment. Nuclei with odd mass numbers have spin angular momentum quantum numbers I that are odd-integral multiples of 1/2. Nuclei with even mass numbers and odd nuclear charges have integral spin I, while those with even nuclear charge are spinless.

A nucleus with spin I has an angular momentum $I(h/2\pi)$, where h is Planck's constant. If $I \neq 0$, the nucleus will possess a magnetic moment μ, which is taken parallel to the angular momentum vector. A set of magnetic quantum numbers, m, given by the series

$$m = I, I-1, I-2, \ \ldots - I, \tag{20.1}$$

describes the values of the magnetic moment vector which are permitted along any chosen axis. For spin 1/2 nuclei (^{1}H,^{13}C,^{15}N,^{19}F,^{29}Si,^{31}P), $I = 1/2$ and $m = +1/2$ and $-1/2$. In general there are $2I + 1$ possible orientations of μ, or magnetic states of the nucleus. The ratio of the magnetic moment to the angular momentum is called the gyromagnetic ratio, γ,

$$\gamma = 2\pi\mu/hI \tag{20.2}$$

and is characteristic for a given nucleus (see Table 20.1).

With the exception of ^{2}H, the nuclei common to the NMR studies of polymers usually have spin $I = 1/2$, and are characterized by $2I + 1 = 2$ magnetic states, $m = +1/2$ and $-1/2$. In the absence of an applied magnetic field, both nuclear magnetic states have the same energy, but they correspond to states of different potential energy upon application of a uniform magnetic field B_0. The magnetic moment is either aligned along ($m = +1/2$) or against ($m = -1/2$) the applied field B_0, with the antiparallel state ($m = -1/2$) corresponding to a higher energy. The nuclear magnetic resonance (NMR) phenomenon makes it possible to detect transitions of the magnetic nuclei between these spin states.

TABLE 20.1. *Nuclei of major interest to the NMR spectroscopy of polymers [1].*

Isotope	Abundance (%)	Nuclear charge (z)	Spin	μ^a	$\gamma \times 10^b$	Relative^c *sensitivity*	ν_0 at 1 T (MHz)
^{1}H	99.9844	1	1/2	2.7927	2.6752	1.000	42.577
^{2}H	0.0156	1	1	0.8574	0.4107	0.00964	6.536
^{13}C	1.108	6	1/2	0.7022	0.6726	0.0159	10.705
^{15}N	0.365	7	1/2	−0.2830	−0.2711	0.00104	4.315
^{19}F	100	9	1/2	2.6273	2.5167	0.834	40.055
^{29}Si	4.70	14	1/2	−0.5548	−0.5316	0.0785	8.460
^{31}P	100	15	1/2	1.1305	1.0829	0.0664	17.235

[a]Magnetic moment in units of the nuclear magneton, $eh/(4\mu M_p c)$.
[b]Magnetogyric ratio in SI units.
[c]For equal numbers of nuclei at constant field.

20.2 RESONANCE

In Fig. 20.1 we have schematically drawn a nuclear magnetic moment μ in the presence of an applied field B_0 acting along the z-direction. The angle θ between μ and B_0 does not change, because the torque,

$$L = \mu \times B_0 \tag{20.3}$$

tending to tip μ toward B_0 is exactly balanced by the spinning of the magnetic moment, resulting in a nuclear precession about the z-axis. Attempting to force the alignment of μ along the z-axis by increasing B_0 only results in faster precession. A spinning top experiencing the earth's gravitational field is a good analogy to nuclear precession in a magnetic field. The precessional or Larmor frequency, v, of the spinning nucleus is given by

$$v = (\gamma/2\pi)B_0, \tag{20.4}$$

and is independent of θ. The energy of the system does, however, depend on the angle between μ and B_0:

$$E = -\mu \cdot B_0 = -\mu B_0 \cos\theta. \tag{20.5}$$

By application of a small rotating magnetic field B_1 orthogonal to B_0 (see Fig. 20.1), the orientation θ between μ and B_0 may be altered. μ will now experience the combined effects of B_1 and B_0 if the angular frequency of B_1 coincides with v, the precessional frequency of the nuclear spin. In this situation, the nucleus absorbs energy from B_1 and the orientation between μ and B_0 changes; otherwise B_1 and μ would not remain in phase and no energy would be transferred between them.

If the rotation rate of B_1 is varied through the Larmor frequency of the nucleus, a resonance condition is achieved (NMR), and a transfer of energy from B_1 to the spinning nucleus occurs producing an oscillation of the angle θ between μ and B_0. At $B_0 = 1$T (1 T = 1 Tesla = 10 kilogauss) the resonant frequencies (v_0) of the nuclei commonly observed in polymers are listed in Table 20.1.

20.3 NUCLEAR SPIN INTERACTIONS AND RELAXATION

Figure 20.2 illustrates the magnetic energy levels for a spin-1/2 nucleus in a magnetic field B_0. The energy separation between spin states is

$$\Delta E = 2\mu B_0, \tag{20.6}$$

and the relative populations of the upper (+) and lower (−) energy states is given by the Boltzmann expression

$$N_+/N_- = \exp(-\Delta E/kT) = \exp(-2\mu B_0/kT). \tag{20.7}$$

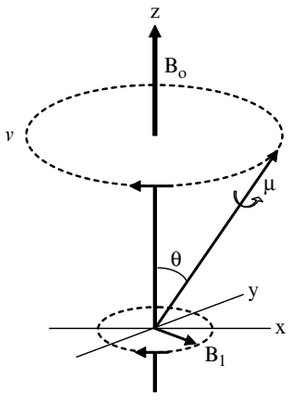

FIGURE 20.1. Nuclear magnetic moment μ in a magnetic field B_0.

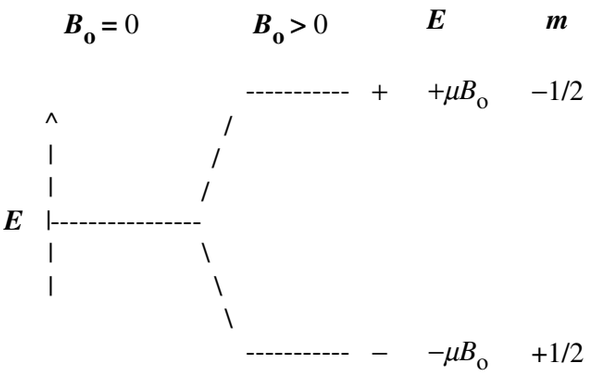

FIGURE 20.2. Energy levels for a spin 1/2 nucleus in a magnetic field B_0.

If we make the approximation $e^{-x} = 1 - x$ for small x, then the excess population of the lower energy spin state (−) is

$$(N_- - N_+)/N_- = 2\mu B_0/kT. \tag{20.8}$$

At a field strength of $B_0 = 2.34$T, $\nu_0 = 100$ MHz for ^{1}H nuclei, the separation between magnetic energy levels for proton nuclei is ca. 10^{-2} cal, which results in an excess population of ca. 2×10^{-5} spins of lower energy aligned parallel with B_0. This small spin population difference leads for an assemblage of nuclei to a correspondingly small macroscopic magnetic moment directed along B_0. (NMR spectroscopy is a relatively low sensitivity technique for this reason, and usually requires extensive signal averaging.) Because the magnetic energy levels are degenerate in the absence of B_0, removal of the applied field results in a loss of the macroscopically observable net magnetic moment.

What mechanisms are responsible for establishing the Boltzmann distribution of spin states following application of B_0, and how long does it take? Such a relaxation is possible because each spin is not completely isolated or decoupled from the rest of the molecules in the sample, referred to as the lattice. Molecular motions of the neighboring nuclei, which constitute the lattice, provide the mechanism for transferring thermal energy between the spins and their surroundings. The relative motion of neighboring nuclei generates fluctuating magnetic fields which are felt by the observed nucleus as it precesses about the direction of the applied field B_0. A broad range of frequencies will be associated with the fluctuating fields produced by the lattice motions, because, relative to the observed nucleus, these motions are nearly random. Components of the fluctuating magnetic fields generated by the lattice motions which lie along B_0 (see Fig. 20.1) and have frequency ν_0 will, like B_1, induce transitions between the magnetic energy levels of the observed nuclei. Therefore, the rates of spin–lattice relaxation must be directly connected to the rates of molecular motions in the lattice.

T_1, the spin–lattice relaxation time, is the time required for the difference between excess and equilibrium spin populations to be relaxed by a factor of e. In liquids, T_1 usually ranges from 10^{-2} to 10^2s, while T_1 may be as long as hours in rigid solid samples. Spin–lattice relaxation produces a change in energy by redistributing magnetic moments with components along the applied field B_0.

Consequently, T_1 is often called the longitudinal relaxation time and is associated with a decay of the macroscopic nuclear moment along the direction (longitudinal or z-axis direction) of the applied field B_0.

A second mode by which nuclear magnetic moments may interact is illustrated in Fig. 20.3. Here a pair of nuclear moments precess about the B_0-axis and each is decomposed into a static component along B_0 (a) and a component rotating in the xy-plane (b) transverse to B_0. If the rotating component precesses at the Larmor frequency ν_0, then a neighboring nucleus may be induced to undergo a spin transition, or flip, *via* a spin exchange, i.e., from $\uparrow\downarrow$ to $\downarrow\uparrow$ for example. Though no net change in the total energy of the system or in the net macroscopic magnetization is produced by the exchange of neighboring nuclear spins, clearly the lifetimes of the interacting spins are affected. Exchange, or flipping, of neighboring nuclear spins is called spin–spin relaxation and is characterized by T_2, the spin–spin relaxation time. Because T_2 is concerned with the rate of change of magnetization in the xy-plane, transverse to B_0, it is also called the transverse relaxation time.

In general spin–lattice relaxation (T_1), through molecular motions, effects NMR signal intensities, while spin–spin relaxation (T_2), is reflected in the broadening of NMR signals.

20.4 NMR FREQUENCIES AND CHEMICAL SHIFTS

By application of a rotating magnetic field B_1 transverse to the static field B_0, about which a spinning nuclear magnetic moment is precessing at $\nu_0 = (\gamma/2\pi)B_0$, we can flip the nuclear spin by rotating B_1 at ν_0. However, if all nuclei of the same type, e.g., all protons, were to flip or resonate at the same field strength B_0, then NMR would not be a spectroscopic tool useful for the study of molecular structure or for observing the relative mobilities of different portions (micro- and/or macroscopic) of a sample.

Fortunately, the resonant frequency of a nucleus depends on its chemical and/or structural environment in addition to its nuclear characteristics (γ).

When placed in a magnetic field B_0, the cloud of electrons about each nucleus produces orbital currents which are accompanied by small local magnetic fields proportional to B_0 but in the opposite direction (diamagnetic), thereby effectively shielding the nucleus from B_0. A slightly higher value of B_0 is needed to achieve resonance, because the actual local magnetic field B_{loc} experienced by a nucleus is expressed as

$$B_{loc} = B_0(1 - \sigma), \tag{20.9}$$

where σ is the electronic screening constant. (Subsequently we will point out that σ is not strictly a constant, but actually is a vector due to the anisotropic distribution of electrons that shield nuclei.) σ is highly sensitive to molecular structure, but is independent of B_0. The resonant Larmor frequency becomes

$$\nu_0 = \mu B_{loc}/hI = \mu B_0(1 - \sigma)/hI, \tag{20.10}$$

and the separation between nuclear spin energy levels is reduced to (see Eq. (20.6))

$$\Delta E = 2\mu B_{log} = 2\mu B_0(1 - \sigma). \tag{20.11}$$

Clearly, nuclear screening decreases the spacing of nuclear magnetic energy levels. An increase in magnetic shielding

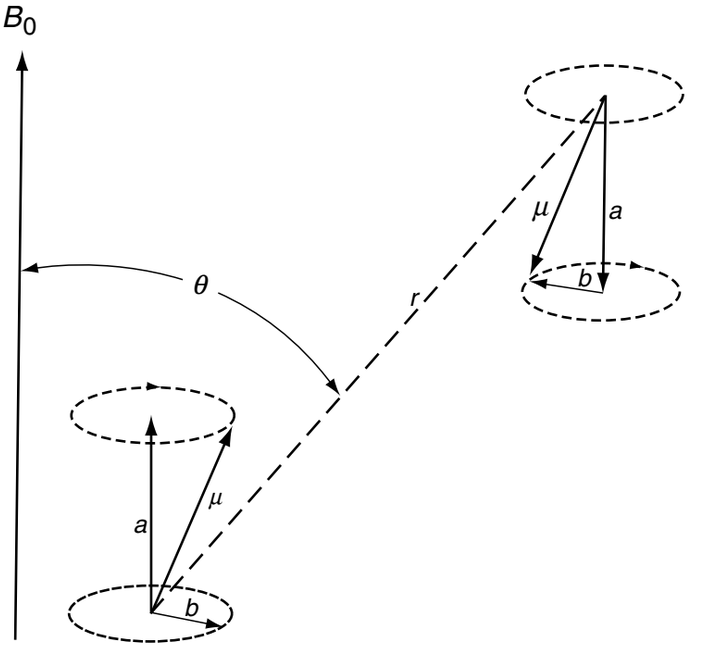

FIGURE 20.3. A pair of precessing nuclear moments with static (a) and rotating (b) components.

(σ) requires an increase in B_0 at constant v_0 or a decrease in v_0 at constant field strength B_0 to achieve resonance.

The numbers and types of atoms and groups of atoms attached to or near the observed nucleus influence nuclear shielding. It is this dependence of σ upon molecular structure that lies at the heart of NMR's utility as a probe of molecular structure and permits the observation of the spin relaxation behavior and therefore the mobility of each nucleus with a distinct resonance frequency. We can see from Eq. (20.10) that the resolution of NMR spectra can be improved by maximizing the static applied field B_0. Increasing B_0 also increases the sensitivity of the NMR experiment (see Chapter 2 of [1], for example). Consequently, the manufacture of superconducting, high-field strength magnets ($B \geq 20$ T) continues.

There is no natural fundamental scale unit in NMR spectroscopy. Both the energies of transition between spin quantum levels and the nuclear shielding produced by the screening constant σ are proportional to the applied field B_0. In addition, there is no absolute zero ''reference point'' in NMR. These difficulties are avoided by expressing the resonant frequencies of nuclei in parts-per-million (ppm, or relative changes in B_0), and referring the observed changes or displacements in resonance frequencies, called chemical shifts, to the ppm relative change in the resonant frequency of an arbitrary reference substance added to the sample. In ^{1}H and ^{13}C NMR spectroscopy, for example, it is customary to use tetramethylsilane (TMS) as the reference compound, where the chemical shifts δ of both ^{1}H and ^{13}C nuclei of TMS are taken as $\delta = 0$ ppm. TMS is selected because both its protons and ^{13}C nuclei are more shielded (resonate at higher magnetic fields) than the nuclei of nearly all other organic molecules.

20.5 SPIN–SPIN COUPLING

Nuclei with magnetic moments may be coupled to each other either directly through space (dipolar coupling) or indirectly through their intervening chemical bonds (scalar coupling). As mentioned previously, two nuclei will feel, in addition to B_0, a local magnetic field B_{loc} produced by each other. B_{loc} is given by

$$B_{loc} = \pm\mu r^{-3}(3\cos^2\theta - 1), \qquad (20.12)$$

where r is the distance between the nuclei and θ is the angle between B_0 and the line joining them (see Fig. 20.3).

Note that B_{loc} in Eq. (20.12) is distinct from the B_{loc} in Eq. (20.9), where nuclear shielding is produced by the motion of the surrounding cloud of electrons. The θ angles in Figs. 20.1 and 20.3 are distinct, because in Fig. 20.1 θ describes the angle of precession between the nuclear magnetic moment μ and the applied magnetic field B_0. The fact that B_{loc} may add to or subtract from B_0 depending upon whether the neighboring magnetic dipole is aligned with or against B_0 is reflected in the $\pm$ sign in Eq. (20.12). This form of spin–spin coupling is called dipolar coupling and can act to broaden the resonance line of a specific nucleus.

There are two important circumstances where dipolar coupling does not contribute to the broadening of resonances.

The first is when all nuclei are rigidly oriented to each other at the magical angle of $\theta = 54.7°$, because then $\cos^2\theta = 1/3$, and $3\cos^2\theta - 1$ and $B_{\text{loc}} = 0$ (see Eq. (20.12)). If the relative orientations of neighboring nuclear spins vary rapidly with respect to the time a nucleus spends in a given spin state (along or opposed to B_0), then B_{loc} is given by its space-average

$$B_{\text{loc}} = \mu r^{-3} \int_0^{\pi} (3\cos^2\theta - 1)\sin\theta \, d\theta, \qquad (20.13)$$

which also vanishes. Both of these circumstances are important for observing high-resolution NMR spectra of polymers and will be discussed further.

Nuclear spins may also be coupled by orbital motions of their valence electrons or polarization of their spins occurring indirectly through their intervening chemical bonds. Unlike direct dipolar coupling of nuclear spins, this indirect or scalar coupling is not affected by molecular tumbling and is also independent of B_0. Two spin-1/2 nuclei so coupled will each split the other's resonance into a doublet, because in a large collection of such nuclear pairs, the probabilities of finding each other's spin with $(+1/2)$ or against $(-1/2)\,B_0$ are nearly equal (see Eqs. (20.7) and (20.8)). If one nucleus of this pair is further coupled to a second group of two identical nuclei with $++$, $+-(-+)$, and $--$ spin orientations, then the resonance of the first nucleus will appear as a 1:2:1 triplet, while the resonances of the identical pair will be a doublet. A single nucleus scalar-coupled to three equivalent neighboring spins with $+++$; $++-$, $+-+$, $-++$ $(--+, -+-, +--)$; and $---$ orientations would exhibit a 1:3:3:1 quartet of resonances. A spin-1/2 nucleus with n equivalently coupled neighbors also each of spin-1/2 will have its resonance split into $n + 1$ peaks.

Typically, in the NMR spectra of polymers, only ^{1}H–^{1}H, ^{13}C–^{1}H, ^{13}C–F^{19} , ^{15}N–^1H, ^{19}F–^{19}F, ^{19}F–^1H, ^{29}Si–^1H, and ^{31}P–^{1}H scalar couplings are important. The magnitude and sign of the scalar coupling of two magnetic nuclei depend on their local substituents and geometries. The strength of the coupling in Hz is designated ^xJ, where the superscript x denotes the number of intervening chemical bonds between the coupled nuclei. A particularly useful relation is based on the observed geometry; conformation-dependent vicinal ^{1}H–^{1}H couplings ^3J, which are observed to be large ($\sim$ 12 Hz) when vicinal protons are *trans*, exhibit markedly smaller ($\sim$ 2 Hz) values in their *gauche* conformation.

20.6 EXPERIMENTAL OBSERVATION OF NMR

A drawing of a superconducting magnet used in modern high-field NMR spectrometers is presented in Fig. 20.4. The magnet is bathed in liquid helium to maintain its superconductivity, thereby alleviating the exorbitant electrical power operating requirements of electromagnets producing these same high magnetic fields. The radio frequency coil provides the rf energy appropriate to excite the nuclei in the sample to resonance. The degeneracy of the nuclear magnetic spin energy levels is removed by the static magnetic field B_0. Application of the rotating magnetic, or electromagnetic, field B_1 excites transitions between these energy

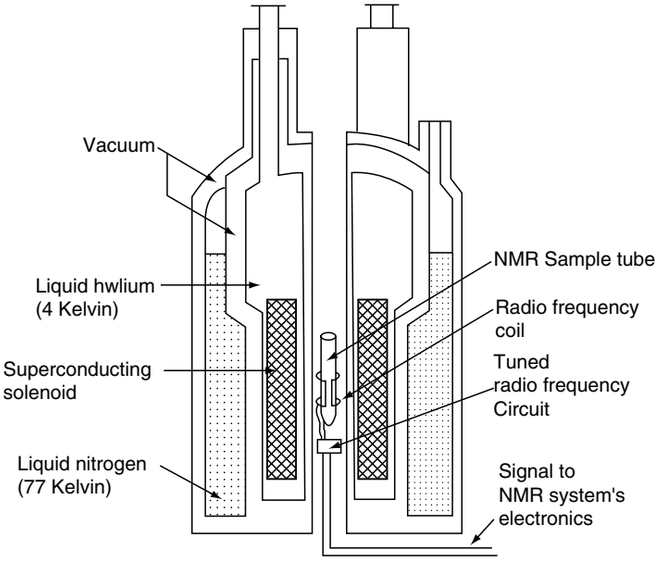

FIGURE 20.4. Cross-section of a superconducting NMR magnet (adapted from Bovey and Jelinski [2]). Magnet assembly has a diameter of 70 cm, while the sample tude is 1 cm in diameter. B_0 and B_1 lie along the horizontal and vertical directions, respectively, in this diagram.

levels. When the frequency of the B_1 field (radio frequency, or rf, in megahertz) is equal to the Larmor frequency of the observed nucleus, the resonance condition occurs, i.e., when

$$B_1 = \nu_0 = \gamma(B_{\text{loc}}/\pi). \tag{20.14}$$

Most samples will have nuclei with multiple Larmor frequencies, because most molecules have more than a single magnetically equivalent group (CH, CH_2, CH_3, for example), leading to several resonance frequencies or chemical shifts.

The method used to excite the nuclei and achieve resonance must clearly be capable of covering all of the Larmor frequencies in the sample. This is achieved in the Fourier transform (FT) method by simultaneously exciting all the Larmor frequencies by application of a pulse (short burst) of rf signal (B_1) at or near all ν_0s, which results in the equalization of the populations of the nuclear spin energy levels. Equilibrium spin populations are reestablished in a free-induction-decay (FID) process following the rf pulse. The vector diagram in Fig. 20.5 can be used to visualize the effect of the rf pulse (B_1) on the nuclear spins and their subsequent FID to equilibrium.

In general terms, T_2 influences the line widths and T_1 influences the relative intensities of signals observed in a NMR spectrum. T_2 is the decay time constant of the FID, and the inverse relationship between time and frequency leads to

$$\Delta\nu \text{ (Hz)} = 1/(\pi T_2), \tag{20.15}$$

where $\Delta\nu$ is the line-width-at-half-height.

Figure 20.6 gives a pulse sequence representation of the vector diagram in Fig. 20.5. The detected signal, or FID, is obtained as a voltage in the time domain. The rf pulse is repeated many times to improve signal-to-noise ratio, and the delay time between pulses must be long enough for T_1 processes to be complete. Fourier transformation of the time-domain signal results in the usual frequency-domain spectrum. The FT method of acquiring NMR signals saves time by collecting data (all ν_0s) simultaneously, and is well suited to signal averaging by collecting multiple FIDs from weak signals before Fourier transformation.

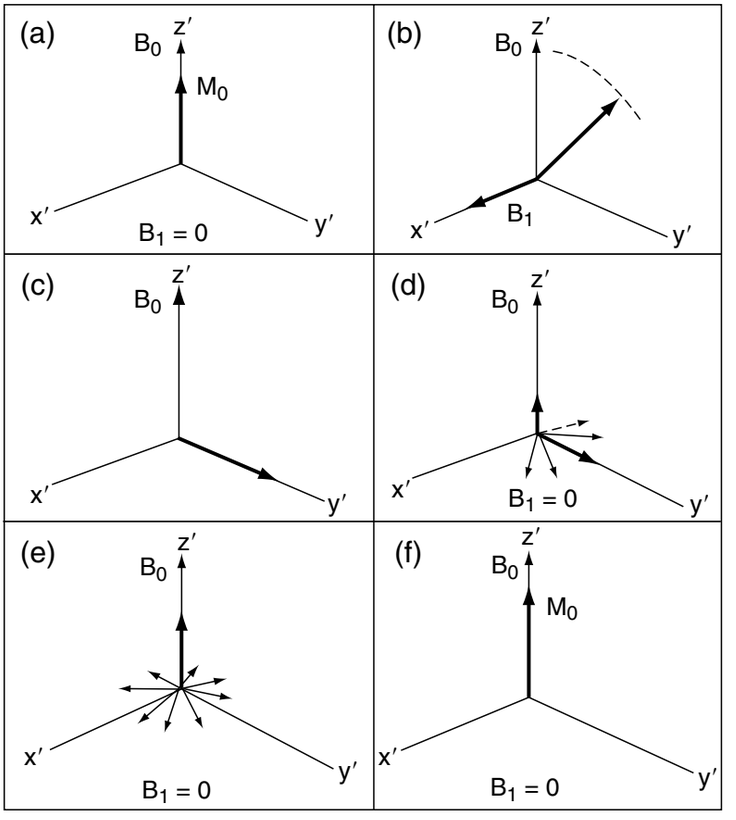

FIGURE 20.5. Rotating frame diagrams describing the pulsed NMR experiment. (The "primed" axes are used to indicate a coordinate system that is rotating at the Larmor frequency.) (a) The net equilibrium nuclear magnetization M_0 is aligned along the direction of the static magnetic field B_0. (b) and (c) An rf field B_1 is applied perpendicular to B_0. The duration of B_1 is sufficient to tip the net magnetization by 90°. (d) and (e) The spins begin to relax in the x', y' plane by spin–spin (T_2) processes and in the observable z′ direction by spin–lattice (T_1) processes. (f) The equilibrium magnetization M_0 is reestablished along B_0.

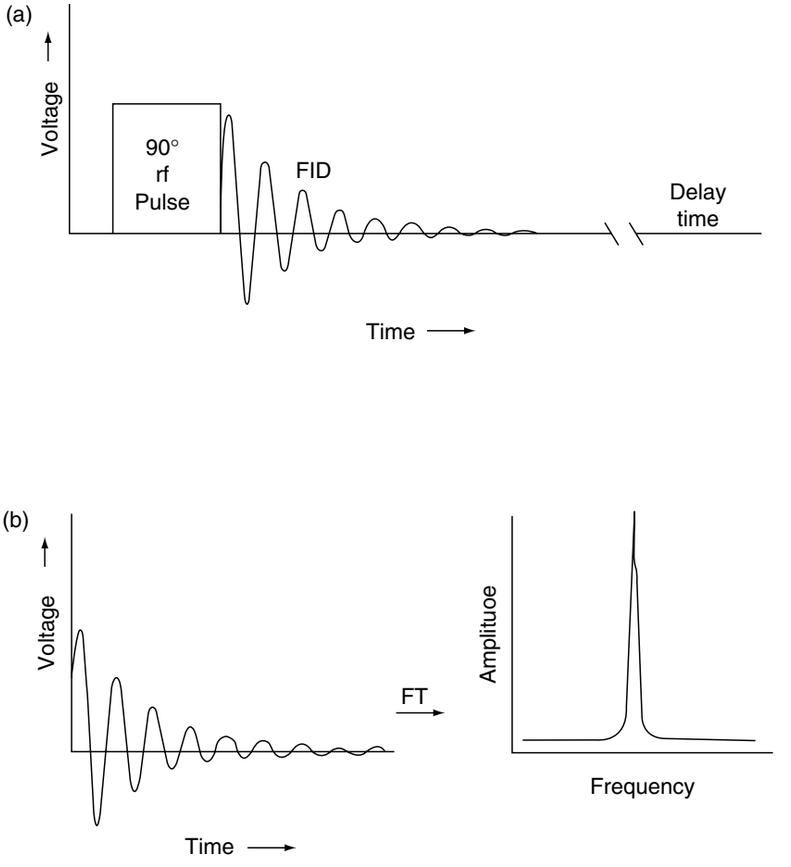

FIGURE 20.6. (a) Representation of a 90° rf pulse (B_1) and the ensuing Free-induction-decay (FID). (b) Fourier transformation of the time-domain FID into the frequency-domain signal.

20.7 HIGH RESOLUTION NMR OF POLYMERS

Unlike small molecules, the volumes pervaded and influenced by dissolved and randomly coiled macromolecules are much larger (ca. 100 times) than the sum of their hard-sphere molecular volumes. This leads to entrapment of surrounding solvent molecules and polymer–polymer entanglements, resulting in solutions with very high viscosities. However, both the frequency at which a magnetic nucleus resonates and the width or resolution of the resulting resonance peak depend on the local polymer microstructure and its motional dynamics in the immediate vicinity of the observed nucleus. The local segmental motions of dissolved polymers are usually rapid (nano- to picosecond range), so NMR serves as a local microscopic probe of polymer microstructures and their motions. As a consequence, NMR can even provide highly resolved spectra for dissolved polymers whose overall motion may be sluggish (high solution viscosities), but whose local segmental motions are rapid.

20.8 ^{1}H NMR

The 500 MHz proton NMR spectra recorded with a superconducting magnet (11.7 T) for two samples of poly (methyl methacrylate) (PMMA) as 10% solutions in chlorobenzene-d_5 at 100 °C are presented in Fig. 20.7 [3]. A free radical initiator was used in the polymerization of the syndiotactic sample (s-PMMA) in (a), while the isotactic sample (i-PMMA) in (b) was obtained with an anionic initiator [4]. It is apparent from the methylene proton portions of both spectra that free radical and anionic initiated polymerization of methyl methacrylate results in PMMA samples with very different microstructures.

The methylene protons in the *racemic* (*r*) diad drawn in Fig. 20.7(a) are magnetically equivalent because of the twofold axis of symmetry present in an *r*-diad. They resonate at the same frequency, leading to a singlet, despite the strong two-bond geminal ^2J coupling between them. In the *meso* (*m*) diad of Fig. 7(b), which lacks a symmetry axis, the methylene protons are magnetically nonequivalent and

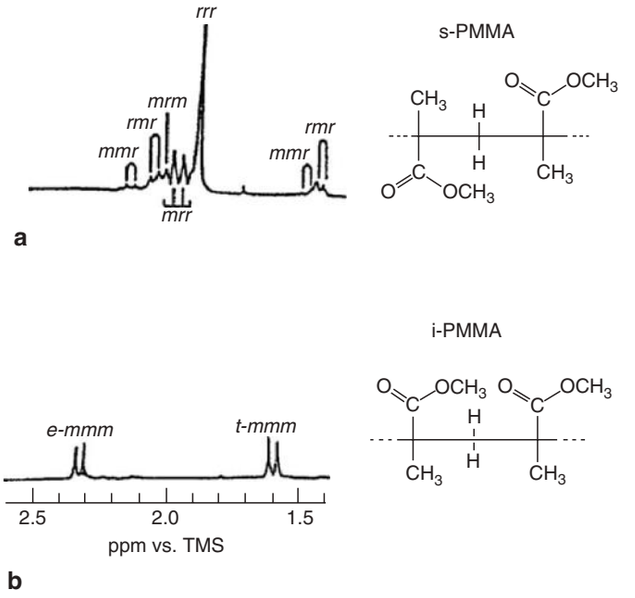

FIGURE 20.7. 500 MHz ^{1}H NMR spectra of (a) s-PMMA and (b) i-PMMA. Only the methylene proton regions are shown. (Adapted from Schilling *et al.* [3].) *e*, *t* methylene protons lie on the same side of the planar, zigzag backbone as the $-\overset{\overset{O}{\|}}{C}-O-CH_3$, $-CH_3$ side chains.

therefore appear as a pair of doublets, each with a spacing of ~15 Hz produced by their ^2J geminal coupling.

The PMMA sample produced by anionic initiation does show (b) almost exclusively a pair of doublets, indicating that nearly all of its diads are *m*, so this sample of PMMA is very highly isotactic. The principal methylene proton resonance observed for the free radical PMMA is a singlet at 1.9 ppm (a), meaning that most of its diads are *r* and that this sample is predominantly syndiotactic, though more stereochemically irregular than the anionically initiated sample. It is clear from this example that ^{1}H NMR can provide information about the absolute stereoregularity of a vinyl polymer (isotactic versus syndiotactic), which is often impossible to obtain by other methods (including x-ray diffraction from crystalline polymer samples).

The 220-MHz ^{1}H NMR spectra of three polypropylene (PP) samples are presented in Fig. 20.8 [5–7]. Note the apparent greater resolution of the spectra in (a) and (c) recorded for the stereoregular samples (isotactic and syndiotactic) than for atactic PP in (b). The impression of degraded resolution in the spectrum for atactic PP is a consequence of the overlapping of many slightly different resonance frequencies or chemical shifts corresponding to the various triad and tetrad stereosequences present in the atactic sample. Only the *rr* (*rrr*) and *mm* (*mmm*) triads (tetrads) are present in the stereoregular syndiotactic and isotactic samples, respectively.

In addition to the geminal coupling (^2J) of methylene protons in meso diads, the methine and methyl and the methylene and methine protons show significant vicinal, three-bond scalar couplings (^3J) in nearly all stereosequences. By application of ^{1}H–^{1}H homonuclear decoupling or double resonance, some of these couplings can be removed. The scalar, or *J*, coupling between magnetically nonequivalent nuclei A, B can be removed by irradiating B with a strong transverse rf field B_2 tuned to its resonance frequency, while observing A with the weaker B_1 field. B_2 causes a rapid oscillation of nucleus B between its spin states such that it no longer couples to nucleus A. Unfortunately, in PP the methine protons are coupled to both methylene and methyl protons, requiring a triple resonance experiment to simultaneously remove all vicinal couplings. Because the methylene protons in *m*-diads resonate at widely separated frequencies, which in turn are also distinct from the resonance frequency of methylene protons in *r*-diads (see Fig. 20.8), complete removal of the vicinal couplings observed in the ^{1}H NMR spectra of PPs is very unlikely.

20.9 ^{13}C NMR

The ^{13}C nucleus occurs at a natural abundance of only 1.1% and has a small magnetic moment, about one-fourth that of the proton. Both factors tend to mitigate the observation of high resolution ^{13}C NMR spectra (see Table 20.1). However, employing a greater number of spectral accumulations during the FT recording of spectra can compensate for the decrease in the sensitivity of the ^{13}C nucleus. Suitable signal-to-noise ratios can also be achieved in ^{13}C NMR

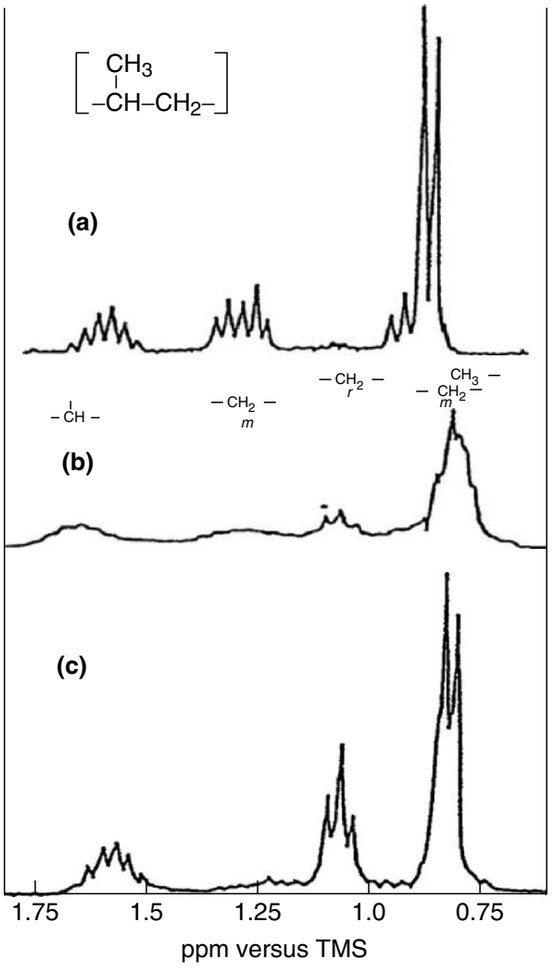

FIGURE 20.8. 200 MHz ^{1}H NMR spectra of (a) isotactic, (b) atactic, and (c) syndiotactic polypropylenes [5–7].

spectra, but at the expense of considerably longer observation times due to this necessary signal averaging.

Further increase in signal intensity is obtained by removing the heteronuclear spin coupling between ^{13}C nuclei and their directly bonded protons, as well as the resulting nuclear Overhauser enhancement (NOE) [8]. Removal of the strong (125–250 Hz) ^{13}C–^{1}H heteronuclear coupling, through application of a second transverse rf field at the proton resonance frequencies, results in the collapse of ^{13}C multiplets and an improved signal-to-noise ratio. Saturation of nearby protons produces a nonequilibrium polarization of the ^{13}C nuclei, which exceeds their thermal value, and increases the observed signal strength. It has been demonstrated [9] that the dipolar coupling mechanism dominates for the ^{13}C isotope, and a maximum NOE factor of 3 for the ^{13}C intensity is provided by a directly bonded proton.

An additional means of increasing the sensitivity of ^{13}C NMR spectroscopy can be realized by transferring the polarization of a sensitive nucleus, such as ^{1}H (large γ) to the insensitive ^{13}C (small γ) nucleus. This is achieved by the technique of selective population transfer (SPT) [10] and can enhance the ^{13}C signal intensity by a factor of $\gamma H/\gamma C = 4$. In practice, this is achieved in modern NMR via two-dimensional heteronuclear correlation and polarization transfer experiments (*vide infra*).

Though requiring the application of several additional observational techniques to overcome the inherent insensitivity of the ^{13}C nucleus, ^{13}C NMR spectroscopy can be, and is, used to greater advantage for probing the molecular structures of organic molecules, including polymers. The reason is the much greater sensitivity of ^{13}C nuclear shielding to molecular structure, in the 200 ppm range for neutral organics compared with 10–12 ppm for ^{1}H shielding. The increased sensitivity of ^{13}C resonance frequencies/chemical shifts to local microstructural environments has generally made ^{13}C NMR spectroscopy the method of choice for investigating molecular structure.

The ^{13}C NMR spectra presented in Fig. 20.9 [11] for the same PP samples whose ^{1}H NMR spectra appear in Fig. 20.8 make the superior microstructural sensitivity of ^{13}C NMR plainly evident. While ^{13}C resonances are spread over an $\sim$30 ppm range, all ^{1}H resonances observed for PPs are within $<$ 1 ppm of each other. In addition, the absence of homonuclear (^{13}C–^{13}C) and the easy removal of heteronuclear (^{13}C–^{1}H) scalar couplings further simplify the ^{13}C spectra. Both of these advantages result in the kind of microstructural sensitivity seen in the methyl carbon region of the PP spectra; note that in atactic PP sample all ten possible pentad stereosequences (*mmmm*, *rrrr*, *mmrm*, etc.) are distinctly observed. (Also see in Fig. 20.10 an expansion of the methyl region of the atactic PP spectrum observed at a higher magnetic field, which we will subsequently discuss.)

^{13}C NMR solution spectra of polymers are often recorded at high temperatures for reasons of solubility (especially for crystalline polymers) and segmental mobility (reduction of dipolar line-broadening). At high temperatures a solvent of low volatility (e.g., tetrachloroethene or trichlorobenzene) and with carbon atoms that resonate in spectral regions distinct from the polymer are most advantageous. Since TMS evaporates at high temperatures, an alternative NMR chemical shift reference material, hexamethyldisiloxane (HMDS), is often used.

To insure acquisition of quantitative ^{13}C NMR spectra, the rf B_1 field pulses must be sufficiently separated by delay times that insure spin relaxation is realized for all carbon nuclei in the sample (see Fig. 20.5). If the repetition rate of the rf pulses approaches the T_1s of some of the ^{13}C nuclei in the sample, then incorrect relative intensities will be recorded. As a practical rule [12], the delay between rf pulses should be five times the T_1 of the slowest relaxing carbon nucleus in the sample.

20.10 ^{13}C NMR SPECTRAL ASSIGNMENTS

Of the nuclei, ^{1}H and ^{13}C, which both possess nuclear spin and are common to synthetic polymers, ^{13}C is by far the more sensitive spin probe for polymer NMR studies. ^{13}C NMR spectra suffer neither from a narrow dispersion of chemical shifts (see Figs. 20.8 and 20.9) nor from extensive homonuclear spin–spin (scalar) coupling, both of which complicate the analyses of ^{1}H NMR spectra. (See below how two-dimensional observations increase the sensitivity of ^{1}H NMR to molecular microstructures.) It is the sensitivity of ^{13}C resonance frequencies or chemical shifts, $\delta^{13}C$, to the microstructures of polymers which makes ^{13}C NMR so useful as a structural probe. We noted in Fig. 20.9 that the methyl carbon resonances observed in the 25 MHz ^{13}C

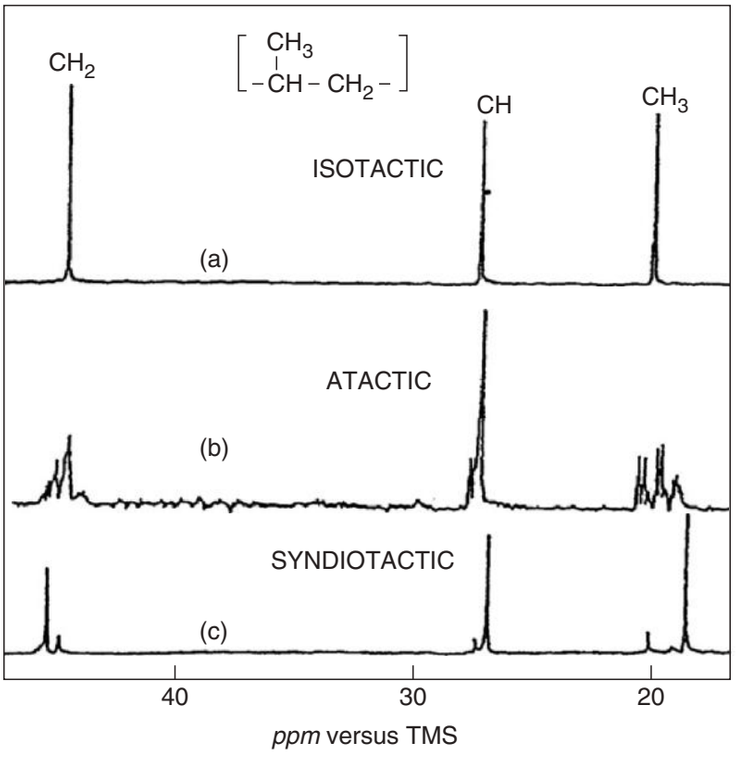

FIGURE 20.9. 25 MHz ^{13}C NMR spectra of the same (a) isotactic, (b) atactic, and (c) syndiotactic PPs [11], whose ^{1}H NMR spectra are also presented in Fig. 20.8.

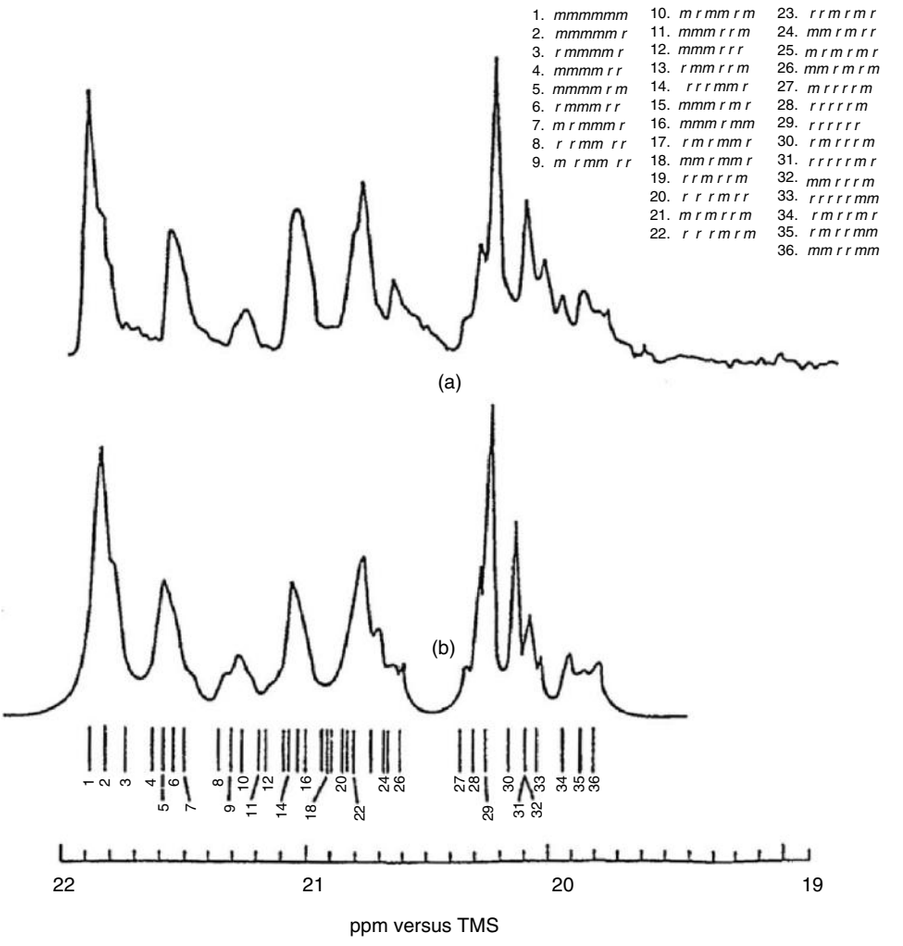

FIGURE 20.10. (a) Methyl carbon region of the ^{13}C NMR spectrum of the same atactic PP shown in Figs. 20.8 and 20.9 recorded at 90 MHz in *n*-heptane at 67°C. (b) Simulated methyl carbon spectrum obtained from chemical shifts calculated using the γ-*gauche* effect method, as represented by the line spectrum below, and assuming Lorentzian peaks of < 0.1 ppm width at half-height [11].

NMR spectrum of atactic PP were sensitive to pentad stereosequences. At 90.5 MHz (see Fig. 20.10), the methyl carbon resonances show sensitivity to heptad stereosequences (*mmmmmm*, *rrrrrr*, *mrmmrr*, etc.) [13]. The ^{13}C NMR spectra of PPs are sensitive to stereosequences extending over 4 (pentads) and 6 (heptads) bonds in both directions along the PP backbone. This long-range sensitivity to microstructural detail makes ^{13}C NMR a valuable tool in the determination of polymer structures.

To realize the full potential of ^{13}C NMR in microstructural studies of polymers, the connections between constituent microstructural features and their corresponding effects on chemical shifts must be established. Traditionally synthesis and NMR spectroscopic analysis of model compounds and polymers with known microstructures have provided the means for assigning the NMR spectra of polymers to their underlying microstructural features. These laborious approaches to the assignment of the NMR spectra of polymers could be eliminated if it were possible to predict the ^{13}C NMR chemical shifts expected for each type of carbon nucleus residing in all potential structural environments.

We have seen that the magnetic field B_i required to obtain the resonance condition for nucleus i at a particular irradiating rf field (B_1) is not equal to the applied static field B_0, but is instead $B_i = B_0(1 - \sigma)$ [see Eq. (20.9)], where the nuclear screening constant, σ, depends on the chemical structural environment of nucleus i. The local electron density in the vicinity of the nucleus shields it from the applied field B_0 by producing small local magnetic fields (diamagnetic currents). Any structural feature that alters the electronic environment of a nucleus will affect its screening constant σ and lead to an alteration in its resonance frequency or chemical shift δ_i.

To date it has not been possible to make sufficiently accurate predictions of ^{13}C NMR chemical shifts

even when applying the most sophisticated ab initio quantum mechanical methods [14,15, and especially 16]. Instead, the effects of substituents and local conformation have been used to correlate the ^{13}C chemical shifts and the microstructures of molecules, including polymers [17,18].

^{13}C NMR studies of paraffinic hydrocarbons [19–23] have led to the following substituent effect rules. Carbon substituents attached at α, β, and γ positions to an observed carbon produce a deshielding of ca. 9 ppm, a deshielding of ca. 9 ppm, and a shielding of ca. -2 ppm, respectively, compared with an observed carbon that is unsubstituted. In PP, for example, the CH_3 carbons possess 1α, 2β, and 2γ carbon substituents; the CH carbons possess 3α, 2β, and 4γ carbon substituents; and CH_2 carbons 2α, 4β, and 2γ carbon substituents. Based on $\alpha = \beta = 9$ ppm and $\gamma = -2$ ppm, we would expect the CH_2 carbons to resonate down-field from the CH carbons by $-1\alpha + 2\beta - 2\gamma = -9 + 18 + 4 = 13$ ppm, while the CH carbons should resonate $2\alpha + 2\gamma = 18 - 4 = 14$ ppm downfield from the CH_3 carbons. This pattern of ^{13}C resonances expected on the basis of these substituent effects is indeed observed (see Fig. 20.9).

The extensive, though smaller, splitting of resonances belonging to the same carbon type (CH, CH_2, or CH_3) observed in the ^{13}C NMR spectra of atactic PP (see Figs. 20.9 and 20.10), must be produced by the presence of different stereosequences, because the numbers of α, β, and γ substituents possessed by each carbon type are independent of stereosequence. On the other hand, it is well known that the local conformations in vinyl polymers like atactic PP are sensitive to stereosequence [24]. The local magnetic field B_i experienced by a carbon nucleus i must be dependent upon the local conformation in its vicinity, Thus,

$$\text{Microstructure} \rightarrow \text{Conformation} \rightarrow B_i \rightarrow \delta^{13}C_i$$

To make the connection between polymer microstructures and $\delta^{13}C_i$s, we need to know the dependence of the local magnetic field B_i on the local conformation. The γ-substituent effect, which shields an observed carbon nucleus, is the source of the dependence of the local magnetic field B_i on the local conformation. Because the observed carbon C^o and its γ-substituent C^γ are separated by three intervening bonds ($-C^o-C-\bigcirc^{\phi}-C-C^\gamma-$), their mutual distance and orientation are variable, depending on the conformation (ϕ) of the central bond. Note that the distance between C^o and C^γ is reduced from 4 to 3 Å on changing their arrangement from *trans* ($\phi = 0°$) to *gauche* $^{\pm}$ ($\phi = \pm 120°$).

Grant and Cheney [25] first suggested the conformational origin of the γ-substituent effects on $\delta^{13}Cs$. In their model it is the polarization of the C^o–H and C^γ–H bonds, resulting from their compression caused by proton–proton (o–γ) repulsion, that leads to a shielding of both carbons. More recently Li and Chestnut [26] presented evidence that correlate shielding γ-effects with attractive van der Waals forces and not repulsive steric interactions, though their results still suggest that their gauche arrangement is required for shielding. Using both semiempirical and ab initio quantum mechanical calculations Seidman and Maciel [27] concluded that the γ-substituent effect is conformational in origin, but cannot be attributed solely to the proximity of the interacting C^o and C^γ carbons. Thus it seems apparent that the γ-substituent effect on δ^{13} Cs has a conformational origin and is, as we will shortly demonstrate, useful in characterizing both the local microstructures and conformations of polymers.

For a γ-substituent to shield a carbon nucleus, we have suggested that they must be in a *gauche* arrangement. The methyl carbons in butane and higher *n*-alkanes have a single γ-substituent, while the methyl carbons in propane have none, but the same number and kinds of α- and β-substituents. The methyl carbons in liquid butane and higher *n*-alkanes resonate at ~13 ppm, while in liquid propane the methyls resonate at ~15 ppm [8]. In their solids the *n*-alkanes crystallize in the fully extended all *trans* conformation, and so here the methyl carbons of butane and the higher *n*-alkanes are not *gauche* to their γ-methyl or methylene carbon substituents. Thus we would expect that $\delta CH_3(\text{solid}C_nH_{2n+2}, n \geq 4) = \delta CH_3(\text{liquid propane})$. Vander-Hart [28] has observed the methyl carbons in the solid *n*-alkanes with $n = 19$, 20, 23, and 32 to resonate at ~15 ppm just like the methyls in liquid propane which have no γ-substituents.

If we know how much *gauche* character (P_g = fractional population of $\Phi = \pm 120°$ conformations (See J. D. Honeycutt in this volume who describes the methodology used to calculate the bond conformational populations), then we can estimate the γ-*gauche* shielding (γ_{C-C}) produced at the methyl carbons in butane, for example. When the observed shielding $\Delta\delta CH_3 = \delta CH_3(\text{butane}) - \delta CH_3(\text{propane}) = 13.2 - 15.6 = -2.4$ ppm is divided by the *gauche* character of the intervening bond ($P_g = 0.46$), $\gamma_{C-C} = \Delta\delta CH_3/P_g = -2.4/0.46 = -5.2$ ppm. When this procedure is applied to *n*-butane, 1-propanol, and 1-chloropropane, the following γ-*gauche* shielding effects are derived: $\gamma_{C-C} = -5.2$ ppm, $\gamma_{C-O} = -7.2$ ppm, and $\gamma_{C-Cl} = -6.8$ ppm [18]. Thus, the shielding produced at a carbon nucleus by a γ-substituent in a *gauche* arrangement can be comparable in magnitude (-5 to -7 ppm) to the $+9$ ppm deshielding produced by the more proximal α- and β-substituents. More important, however, is the conformational dependence of the γ-substituent effect on ^{13}C NMR chemical shifts. Any microstructural variation in a molecule which effects its local conformation can be expected to be reflected in its δ^{13}Cs *via* the γ-*gauche*-effect.

The conformationally sensitive γ-*gauche*-effect permits us to draw the connection between a polymer's microstructure and its ^{13}C NMR spectrum:

$$\text{Microstructure} \rightarrow \text{Conformation} \rightarrow B_i \rightarrow \delta^{13}C_i.$$

By means of the methods described in sections A and B of this handbook, it is possible to establish the connection between the microstructures and the conformations of polymers. The γ-*gauche*-effect establishes the connection between the local polymer conformation and the local magnetic field experienced by a ^{13}C nucleus, so finally

$$\text{Microstructure} \xrightarrow[\text{Effect}]{\gamma\text{-gauche}} \delta^{13}\text{Cs} \qquad [18].$$

To predict the ^{13}C chemical shifts observed for the methyl carbons in a-PP (see Fig. 20.10), which show sensitivity to heptad stereosequences, we simply have to calculate the *trans* and *gauche* probabilities for the backbone bonds in each of the 36 heptad stereosequences. When this is carried out with the Suter–Flory rotational isomeric state (RIS) conformational model for PP [29] and the resultant probabilities of finding CH_3 in a *gauche* arrangement with its γ-substituents (CHs) are multiplied by $\gamma_{CH_3-CH} = -5.2$ ppm, we obtain the δCH_3s shown as the stick spectrum in Fig. 20.10.

Because the γ-*gauche*-effect method of calculating δ^{13}Cs only leads to relative stereosequence-dependent chemical shifts, we are free to translate the calculated shifts as a group to achieve the best agreement with the observed δ^{13}Cs. This has been done in Fig. 20.10, where the agreement between observed and calculated $\delta^{13}CH_3$s has been used to make the stereosequence assignments indicated there. The γ-*gauche*-effect method of assigning resonances in the methyl carbon region of the ^{13}C NMR spectrum of a-PP to heptad stereosequences has been achieved without recourse to the syntheses and study of PP model compounds or stereoregular PPs and without assuming a particular statistical model to describe the expected frequencies of stereosequences produced during polymerization.

Having assigned all heptad stereosequence dependent ^{13}C NMR resonances in a-PP [11,13], integration of the resonances provides us with a detailed accounting of how much of each stereosequence is present. Such information is needed to test various statistical models of PP polymerization [18]. Furthermore, the close agreement between observed and calculated chemical shifts provides strong confirmation of the Suter–Flory rotational isomeric state (RIS) conformational model for PP [29].

20.11 TWO-DIMENSIONAL NMR

If, instead of transforming (FT) the free-induction decay (FID) immediately after the 90° rf pulse in the usual way (see Fig. 20.6), we allow a time interval for the nuclear spins to precess in the transverse x', y'-plane (see Fig. 20.5) and for the evolution of interactions between them, then it is possible to obtain important information concerning the nuclear spin system. We may divide such an NMR experiment into three time domains as indicated in Fig. 20.11. The nuclear spins are permitted to equilibrate with their surroundings *via* spin–lattice relaxation during the preparation period. Following the $90^\circ_{x'}$ pulse, the x',y', and z' components of the nuclear spins (see Fig. 20.5) evolve under all the forces acting upon them, including their direct through-space, dipole–dipole and through-bonds, scalar (J) couplings. This time domain, t_1, is termed the evolution period and defines, along with the acquisition or detection time t_2 common to all pulse experiments, the two-dimensional (2D) character of this experimental approach.

Systematic incrementation of the evolution time t_1 (see Fig. 20.11) provides the second time dependence. After each t_1 period a second $90^\circ_{x'}$ pulse is applied, and the exchange of nuclear spin magnetization may occur. The FID is acquired during t_2 and transformed.

The pulse sequence illustrated in Fig. 20.11 is appropriate for observation of a chemical shift correlated or COSY spectrum, where the correlating influence between nuclear spins is their scalar J-coupling. In a typical experiment we might utilize 1 k, or 1,024, t_1-increments, with $t_1 = 0.5$–500 ms. The FID following each t_1 is different because the interacting spins modulate each other's response.

Each FID detected in t_2 is transformed, producing a series of 1,024 matrix rows, one for each t_1-value. Each row may consist of 1,024 points (square data matrix) representing the frequency-domain spectrum for a particular value of t_1, while the columns provide information about how the FIDs were modulated as a function of t_1.

1024 new FIDs are constructed by looking down the columns of the data matrix in an operation called the ''transpose'' in Fig. 20.11. (Note that at this stage the spectrum is represented for simplicity as a single resonance.) A second Fourier transformation is performed on the newly transposed FIDs, leading to a 2D data matrix which is actually a surface in three-dimensional space. The surface may be represented as either a stacked plot or a contour plot. The contour plot is usually preferred, because recording of the stacked plot is time intensive and it does not clearly demonstrate the complex relationships between the interacting nuclear spins.

Nuclei which do not exchange magnetization have the same frequencies, F_1 and F_2, respectively, during t_1 and t_2 (i.e. $F_1 = F_2$) and yield the normal 1D spectrum along the diagonal of the contour plot. Scalar-coupled nuclei exchange their magnetization and have a final frequency different from the initial frequency, i.e. $F_1 \neq F_2$. These coupled nuclei give rise to the off-diagonal or cross peaks shown in Fig. 20.11. The 2D COSY spectrum provides a diagram of all the J-coupled connectivities in a molecule, and is consequently a very useful technique for assigning the resonances of complex molecules.

A closely related 2D NMR technique, termed NOESY, permits the establishment of through-space connectivities. This technique relies on the through-space dipolar coupling of nuclear spins and uses a 2D version of the nuclear

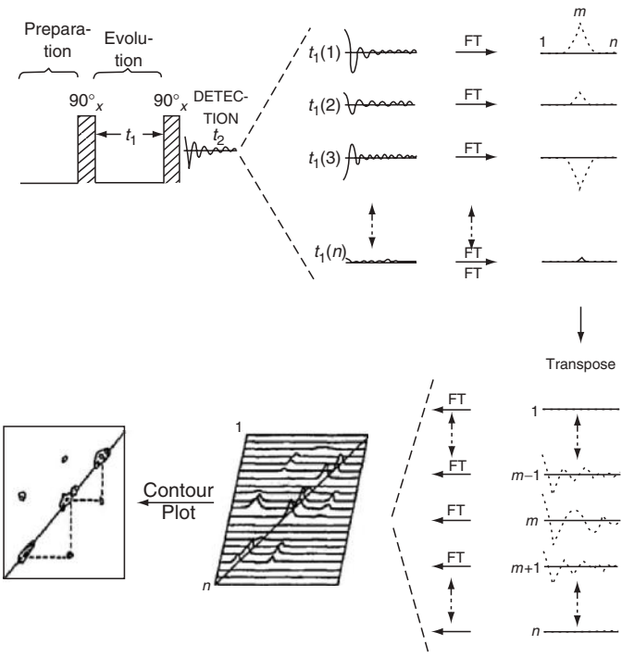

FIGURE 20.11. Schematic repesentation of a two-dimensional (2D) correlated (COSY) NMR experiment and spectrum after Jelinski [30].

Overhauser effect (NOE, see Section 20.9) to map, in effect all intra- and internuclear distances (usually protons) less than ~4 Å.

The advent of these and related multidimensional NMR techniques [31] has resulted in a rebirth of ^{1}H NMR as a means to study molecular structure. Extensive homonuclear J-coupling of protons, which unduly complicate 1D ^{1}H NMR spectra, are used to advantage in 2D ^{1}H NMR to map the atomic connectivities of molecules. Furthermore, the significantly improved resolution observed in 2D ^{1}H NMR spectra somewhat ameliorates the narrow dispersion of ^{1}H chemical shifts.

20.12 NMR OF SOLID POLYMERS

There exist two interactions between nuclear spins and their neighbors or with the applied magnetic field that result in severe broadening of their solid-state NMR spectra when recorded under conditions that produce high-resolution NMR spectra for their solutions. Both of these nuclear interactions, the direct through-space dipolar coupling and the anisotropic electronic shielding of nuclei from the applied magnetic field, are also present in the liquid. They do not lead to resonance line-broadening there because they are averaged to zero (see Eqs. (20.12) and (20.13)) by the rapid and essentially isotropic motions occurring in the liquid. In rigid solid samples like glassy or crystalline polymers, the motional averaging of these nuclear interactions are incomplete and produce spectra like the one shown in Fig. 20.12(a).

^{13}C nuclei observed at natural abundance are dipolar coupled to the usually abundant and nearby ^{1}H nuclei. (see Fig. 20.13) resulting in the splitting (D) of ^{13}C resonances given (in Hz) by

$$D = [h\gamma_C\gamma_H/2\pi r^3](3\cos^2\theta - 1). \qquad (20.16)$$

This splitting is illustrated in Fig. 20.13(b) and corresponds to the dipolar coupling of a ^{13}C nucleus with the two spin states (up and down) of a ^{1}H nucleus located at a distance r and orientation θ (to B_0). The magnitude of this splitting is ca. 10 kHz [34]. In a rigid glassy or crystalline solid polymer powder, the ^{13}C nuclei and their nearby protons are randomly arranged and their C–H vectors assume all possible angles with respect to the external applied magnetic field. This results in a Pake pattern [35] of ^{13}C resonances, as depicted in Fig. 20.13(c), assuming all C–H vectors are of the same magnitude, distance r. Because the ^{13}C nuclei in rigid, solid polymers are dipolar-coupled to protons located at more than a single internuclear distance r, when their dipolar interaction (Eq. (20.16) is averaged over both the distances (r) and orientations (θ) of all the C–H vectors present in the sample, the broad Gaussian lineshape presented in Fig. 20.13(d) is produced.

As a result of their dipolar interactions with nearby abundant protons, the ^{13}C resonance linewidths observed in rigid organic polymers are typically tens of kHz. Since the range of ^{13}C NMR resonance frequencies, or chemical shifts, observed in a given polymer is usually less than 200 ppm, which at an applied field strength of 4.7 T (50 MHz for ^{13}C)

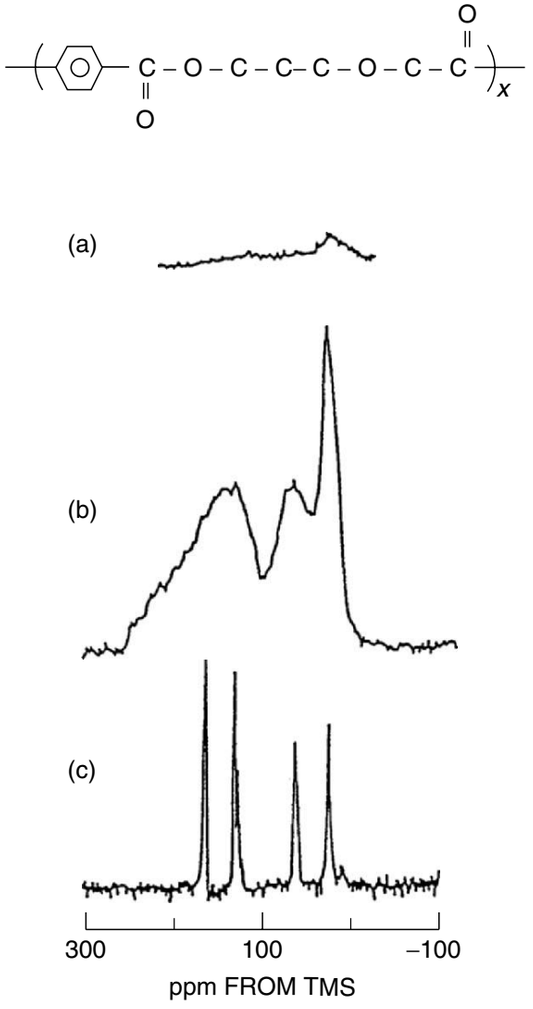

FIGURE 20.12. ^{13}C NMR spectra of bulk poly(butylene terephthalate) (PBT) obtained with low-power dipolar decoupling (a), high-power dipolar decoupling (b), and high-power dipolar decoupling with rapid sample spinning at the magic angle (c) [32].

corresponds to a frequency range of 10 kHz, ^{13}C NMR spectra of solids whose lines are broadened by ^{1}H dipolar coupling (ca. 20 kHz) cannot resolve their chemically shifted, resonance frequencies. Without removing this ^{13}C–^{1}H coupling, ^{13}C NMR spectra of solid polymers, like poly-(butylene terephthalate) (PBT) in Fig. 20.12, cannot provide useable structural information.

If the proton spins could be driven to flip at a rate that is rapid compared to the static ^{13}C–^{1}H dipolar interaction, which occurs naturally in mobile polymer solutions, then the resonance lines observed in solid-state ^{13}C NMR spectra would likewise no longer be broadened by these heteronuclear, spin–dipolar interactions. The ^{13}C NMR spectrum of PBT shown in Fig. 20.12(b) was recorded by applying an rf field B_1 at the resonance frequency of protons, with a field strength of 50 kHz, in a direction perpendicular to the applied field B_0 (analogous to the broadband ^{1}H scalar-J decoupling of ^{13}C NMR solution spectra). Note the substantial increase in spectral resolution [compare (a) and (b) in Fig. 20.12] produced by high-power ^{1}H dipolar decoupling (DD), though falling far short of the resolution observed in spectra recorded in solution. The remaining line broadening in solid-state spectra is due primarily to chemical shift anisotropy (CSA).

CSA reflects the anisotropy inherent in the distribution of electronic currents about nuclei which screen (σ) them from the applied magnetic field B_0. The local magnetic field experienced by a nucleus is anisotropic and therefore three dimensional, so the nuclear screening constant σ is in fact a tensor and may be described [1,32] by

$$\sigma = \sigma_{11}\lambda_{11}^2 + \sigma_{22}\lambda_{22}^2 + \sigma_{33}\lambda_{33}^2. \tag{20.17}$$

The principal values of the chemical shift tensor (σ_{11}, σ_{22}, σ_{33}) give the magnitudes of nuclear shielding in

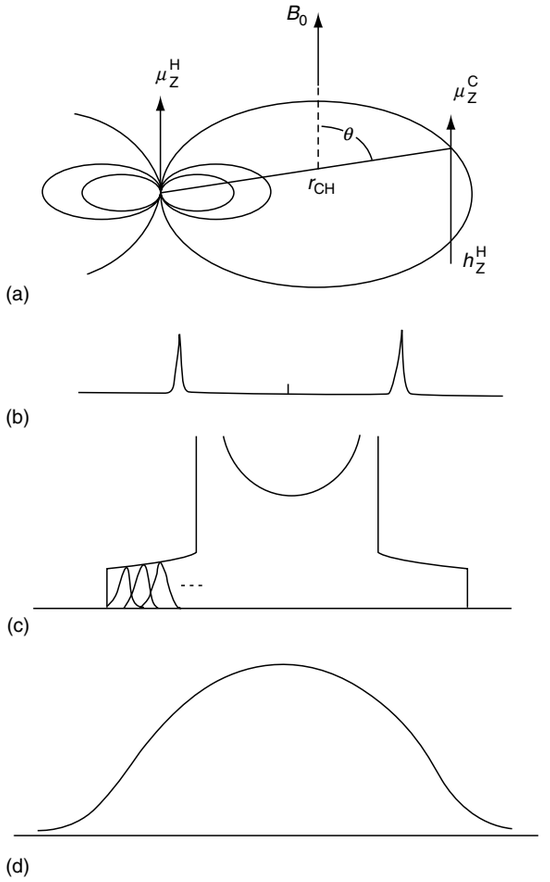

FIGURE 20.13. (a) The through-space dipolar interaction between a ^{13}C and a ^{1}H nuclear spin. The μ_z are the z components of the magnetic moments and h is the z component of the proton dipolar field at the ^{13}C nucleus. (b) Dipolar splitting of isolated C–H pairs at one angle θ relative to the applied magnetic field. (c) Pake pattern expected for isolated C–H pairs distributed at all angles as in polycrystalline or glassy materials. Several components are schematically illustrated. (d) Approximate Gaussian lineshape observed for nonisolated C–H pairs, where all dipolar interactions are operating [33].

three mutually perpendicular directions (Cartesian coordinates), and the λ_s are direction cosines specifying the orientation of the molecular coordinate system with respect to the applied field B_0. Rapid molecular motion experienced by polymer segments in solution results in the observation of isotropic chemical shifts, σ_i, because averaging σ over all orientations yields

$$\sigma_i = 1/3(\sigma_{11} + \sigma_{22} + \sigma_{33}) = 1/3 \text{ trace}(\sigma). \qquad (20.18)$$

It is apparent from Eq. (20.17) that in a rigid, solid sample the chemical shift will depend on its orientation with respect to the applied field. A sample having all like carbon nuclei with the same orientations—as in a single crystal—will exhibit chemical shifts that vary as the crystal is rotated in the applied magnetic field. In a powdered sample, all possible crystalline orientations are present, so the NMR spectrum will consist of the chemical shift tensor powder pattern.

Two theoretical [36] chemical shift tensor powder patterns are illustrated in Fig. 20.14. Principal values σ_{11}, σ_{22}, σ_{33} are indicated, and their isotropic averages, σ_i, are given as dotted lines. In the axially symmetric case (b), $\sigma_{\|}$ and $\sigma_{\perp}$ are the resonance frequencies observed when the principal molecular-axis system is aligned $\|$ and $\perp$ to the applied field. Molecular motion will narrow the chemical shift tensor, by partial averaging, and the resultant powder pattern will then contain information concerning both the axis and angular range of the motion. However, the chemical shift powder pattern contributes to significant broadening of solid-state NMR spectra [see Fig. 20.12(b)] and often obscures the structural information available from the isotropic chemical shifts as observed in solution. This broadening can, however, be removed by high-speed sample spinning at the magic angle.

If a solid powder sample is rotated rapidly about an axis making an angle β with respect to the applied field B_0 [see Fig. 20.14 (c)], the direction cosines (λ_{11}, λ_{22}, λ_{33}) in

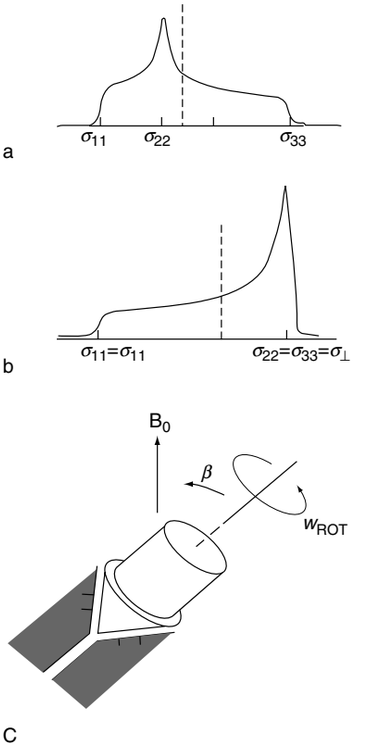

FIGURE 20.14. Schematic CSA tensor powder pattern for an axially asymmetric (a) and axially symmetric (b) tensor. Isotropic chemical shifts (σ_i) are indicated by dashed lines. (c) Typical Andrews [37] sample holder (rotor) rotating on air bearings within a stator (shaded).

Eq. (20.17) vary during each rotation period. For rapid sample rotation, the time average of Eq. (20.17) becomes

$$\sigma = 1/2\sin^2\beta(\sigma_{11}+\sigma_{22}+\sigma_{33}) + 1/2(3\cos^2\beta - 1)$$
$$\times(\text{functions of the direction cosines}). \qquad (20.19)$$

When the angle β between the sample rotation axis and the applied magnetic field is 54.7° (the magic angle), $\sin^2\beta = 2/3$, $3\cos^2\beta - 1 = 0$, and thus $\sigma = \sigma_i$, the isotropic chemical shift.

Rapid magic-angle spinning (MAS) reduces the anisotropic chemical shift tensor powder patterns [see Fig. 20.12(b) and (c)] to their isotropic averages. Chemical shift anisotropies (CSA) of ^{13}C nuclei in different structural environments vary from $\sim$30 ppm for CH_2 carbons to $\sim$200 ppm for aromatic carbons. MAS spinning at a few kHz reduces the CSAs of the aromatic and carbonyl carbons in PBT to their isotropic averages, leading to the ''high resolution'' spectrum seen in Fig. 20.12(c).

Application of high-power ^{1}H-DD and rapid MAS techniques to record the ^{13}C-NMR spectra of solid polymers can produce high-resolution spectra. However, to practically achieve signally averaged, pulsed FT spectra, the rate at which signal averaging can be repeated or the pulse repetition rate is dictated by the spin–lattice relaxation times, T_1, of the ^{13}C nuclei. Because most solids exhibit little motion in the MHz frequency range, which is required for coupling of the ^{13}C spins to their surrounding nuclei or to the lattice, ^{13}C T_1s are long for solids, typically minutes or longer. Rare nuclei, such as ^{13}C (1.1% natural abundance), require extensive signal averaging and the repetition rate of rf pulses becomes an important consideration in their observation by NMR.

The long signal accumulation times required by the low repetition rate for ^{13}C nuclei with long T_1s in solids can be circumvented by transferring polarization from abundant ^{1}H nuclear spins with short T_1s to the ^{13}C nuclei. The repetition rates for signal averaging are now determined by the shorter ^{1}HT_1s (ms–s), because energy is transferred from the proton to the carbon nuclei, a process termed cross-polarization (CP) [38].

Hartmann and Hahn [39] showed that CP can be achieved when two rf fields B_{1H} and $B_{1C} = 4B_{1H}$ are simultaneously applied. $\gamma_H/\gamma_C = 4$, so, when $B_{1C} = 4B_{1H}$ energy is transferred between them, or they are cross-polarized, because $\gamma_C B_{1C} = \gamma_H B_{1H}$ (which is called the Hartmann–Hahn match of heteronuclear rotating-frame frequencies). In the CP experiment ^{13}C nuclei obtain their spin polarization from ^{1}H nuclei, so, not only do the shorter proton spin–lattice relaxation times determine the repetition rate of

the experiment, but their signals also show enhancement by a factor as large as $\gamma_H/\gamma_C = 4$. The CP experiment results in both a time savings and an improvement in the signal-to-noise ratio in the ^{13}C NMR spectroscopy of solid samples.

The initial truly high-resolution ^{13}C NMR spectra of solid polymers were reported by Schaefer and Stejskal [40]. They combined for the first time the three previously developed techniques of high-power proton dipolar decoupling (DD), rapid magic-angle sample spinning (MAS), and cross-polarization (CP), or (CPMAS/DD), to obtain these spectra, which can be utilized to probe the conformations, packing, and motions of solid polymer samples.

20.13 SOLID-STATE NMR APPLICATIONS IN POLYMER SCIENCE

The applications of solid state NMR to polymer science range from simple solution-like experiments, in which the chemical shifts for specific nuclei are observed following the application of a single pulse of radio frequency energy, to complex multidimensional experiments involving hundreds of pulses, which detect both the temporal and spatial relationship of multiple interactions among many dissimilar nuclear spins in a polymer sample. In this brief review, we will make quick mention of well-established methods, with a greater focus on more recent developments that have increased the range of polymer science questions addressable by NMR. The spatial arrangement of polymer chains in bulk crystalline, semicrystalline, or amorphous macromolecules is controlled both by intramolecular energies, e.g., conformational barriers based on the structure of the monomer units, and intermolecular contributions, such as attractive chemical forces between specific chemical moieties. Solid-state NMR can address many of these structural variables, with length scales ranging from monomeric dimensions up to hundreds of nanometers. We summarize recent contributions in the literature that describe the use of solid-state NMR to elucidate chain structure, conformation and stereochemistry, local versus long-range chain dynamics and structural or temporal heterogeneities, and the organization of polymer chains in pure polymers, blends, and composite materials. Recognizing that only an extremely small fraction of recent work may be mentioned here, the more specialized NMR reader may wish to examine Refs. [41–44] for additional details about specific NMR experiments, as well as an extensive source of reference topics.

Why should the polymer scientist consider solid-state NMR as a critical component in the search for new materials or structure–property insights? In almost all cases, polymeric materials are used as solids. Increasingly, these materials are complex mixtures of both crystalline and amorphous components, thereby limiting the efficacy of traditional diffraction techniques. Solid-state NMR is equally adept at interrogating local structure and dynamics in crystalline, amorphous, or mixed physical states composed of both organic and inorganic constituents (i.e., polymer nanocomposites). In addition to this flexibility in the type of sample amenable to analysis, the shear magnitude of possible types of experiments probing local structure, morphology, and dynamics (subhertz to gigahertz frequency ranges) makes solid-state NMR an indispensably powerful tool for polymer science. In particular, the reader will note the large number of references in this review dealing with multicomponent systems, reflecting both the growing importance of blends, copolymers, and composites in polymer material science and the increased selectivity afforded by modern solids NMR techniques.

20.13.1 Conformation and Extended Chain Structure

Syndiotactic polystyrene, s-PS, is a highly stereoregular, semicrystalline vinyl polymer that normally melts at $\sim 270\ ^{\circ}C$ [45,46]. S-PS shows a large number of crystalline polymorphs [47–50] obtained by melt crystallization and solvent-exposure techniques. However, s-PS assumes only two distinct crystalline conformations [all *trans*, planar zigzag (. . . *ttttttt* . . .) and 2_1-helical (. . . *ttggttgg* . . .); $t = trans$ and $g = gauche$], which are characterized by fiber repeats of 5.1 and 7.5 Å, respectively.

Figure 20.15 presents the high resolution CPMAS/DD ^{13}C NMR spectra of two s-PS crystalline polymorphs [51], one with s-PS chains adopting the . . . *tttt-tttt* . . . conformation (a) and the other the . . . *ttggttgg* . . . conformation. We note in spectrum (b) that two CH_2 carbon resonances appear at 38 and 49 ppm, while in spectrum (a) only a single CH_2 carbon resonance at 49 ppm is evident. In the . . . *ttggttgg* . . . polymorph half of the CH_2 carbons are *gauche* to both of their γ-substituent CH carbons, while the other half are *trans* to both γ-CH carbons. We expect, as was also observed for s-PP crystallized in the 2_1-helical . . . *ttggttgg* . . . conformation [52], two CH_2 resonances separated by $\sim 2\times 5.2$ ppm ~ 10 ppm in agreement with spectrum (b). Also the single CH_2 resonance observed for the . . . *ttttttt* . . . polymorph in (a) comes at nearly the same frequency ($\sim$49 ppm) as the most downfield CH_2 resonance observed for the . . . *ttggttgg* . . . polymorph in spectrum (b). These and other observations [18] confirm the validity of the conformationally sensitive γ-*gauche* substituent effects on ^{13}C chemical shifts, with extension of their applicability to solid polymer samples. This strongly implies that the ^{13}C chemical shifts observed for solid polymers are in general primarily influenced by the conformations adopted by their rigid backbones and only to a very minor extent by the crystalline packing of their chains.

Though all of the crystalline polymorphs of s-PS exhibit distinct x-ray diffraction patterns, they exhibit only one or the other of the two $^{13}CPMAS/DD^{13}C$ NMR spectra seen in Fig. 20.15, which correspond to their distinct . . . *ttttttt*

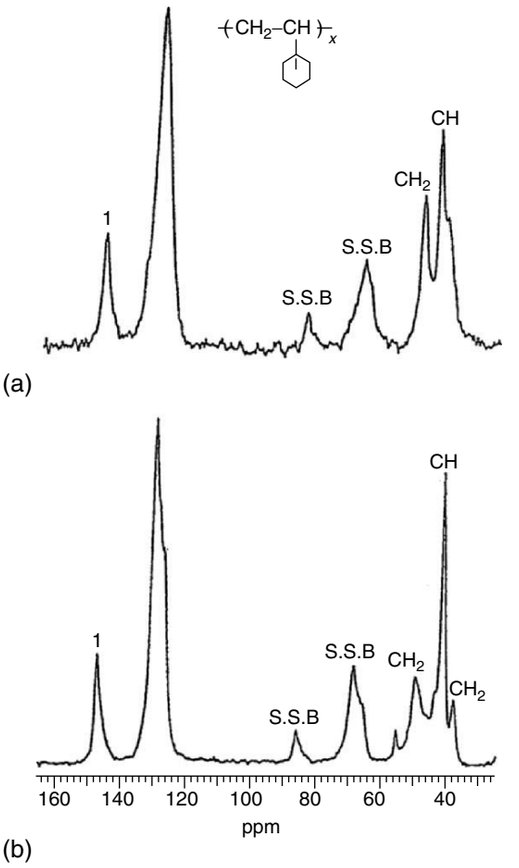

FIGURE 20.15. CPMAS/DD ^{13}C NMR spectra of form I (. . . *ttttttt* . . .) (a) and form II (. . . *ttggttgg* . . .) (b) s-PS crystalline polymorphs [51].

. . . and . . . *ttggttgg* . . . conformations with fiber repeats of 5.1 and 7.5 Å, respectively. As a consequence, we can conclude that among all the crystalline polymorphs observed for s-PS only two chain conformations are represented. Apparently differences in packing of s-PS chains in these two crystalline conformations result in the variety of crystalline polymorphs observed for s-PS [47–50].

However, CPMAS/DD ^{13}C NMR can still be utilized to distinguish among these many crystalline polymorphs. In Table 20.2 the ^{13}C spin–lattice relaxation times (T_1s) observed at room temperature [51] for several of these polymorphs are presented. Samples S_a, $S_{\alpha 1}$ and $S_{\alpha 2}$, and S_0 and $S_{\delta 1}$ represent amorphous, . . . *ttttttt* . . . crystalline, and . . . *ttggttgg* . . . crystalline s-PSs, respectively. Clearly the . . . *ttttttt* . . . polymorphs have longer T_1s (2–10 times longer) than the . . . *ttggttgg* . . . polymorphs. Even amorphous s-PS has longer T_1s than the . . . *ttggttgg* . . . polymorphs. When the T_1 results are coupled with the observation of small solvent peaks in the CPMAS/DD and MAS/DD spectra of the S_0 *and* $S_{\delta 1}$ samples (not presented here [51]), we can conclude that small quantities of the solvents used to induce crystalinity in these s-PS samples are retained in both their crystalline and amorphous glassy regions. Solvent incorporated in the crystalline regions of the . . . *ttggttgg* . . . polymorphs may act as defects causing the crystalline chains to be at least as mobile as those in the completely disordered, glassy portions of these samples.

While straightforward one-dimensional spectra are extremely useful in the analysis of solid polymer chain conformations, recent two-dimensional techniques applied to s-PS and PET (polyethylene terephthalate) demonstrate that correlation of specific spin interactions can provide extremely detailed quantitative information regarding conformer population distributions [53,54].

Polymer Morphology, Organization, and Phase Behavior

Spin-Diffusion Techniques

Spin-diffusion NMR techniques, typically involving abundant homonuclei like ^1H and ^{19}F, are an important and powerful avenue for interrogating heterogeneous systems. Excellent reviews of this area have recently been published [55,56]. While the general use of spin-diffusion to probe length scales of mixing in polymer blends, or to

TABLE 20.2. ^{13}C *spin–lattice relaxation times,* T_1*(s), for the crystalline carbons in s-PS polymorphs [51].*

Sample	C_1	C_{2-6}	CH_2 (~49 ppm),	CH	CH_2 (~38 ppm),
S_a	78	60	83	65	
$S_{\alpha 1}$	400	120	400	200	
$S_{\alpha 2}$	140	134		280	
S_0	74	54	58	59	55
$S_{\delta 1}$	32	24	30	28	30

determine crystallite dimensions in semicrystalline polymers, is not new, recent improvements in spin-diffusion experiments that address some long-standing limitations warrant mention. In general, spin-diffusion techniques require that specific polarization originating from only one component or phase of the sample be generated, or selected, as an initial condition, subsequent redistribution of that magnetization gradient throughout the entire sample during a controlled mixing time, and a final spectroscopic detection step in which the extent of polarization redistribution is quantified as a function of the mixing time. Based on analogies with physical or thermal diffusion models, rate equations describing the diffusion process, along with spin-diffusion coefficient values, may be used to determine approximate length scales (or domain sizes) associated with the diffusion process in a heterogeneous polymer system. Typical dimensions accessible by this static dipole–dipole method range from 1 to 200 nm. While dipolar spin-diffusion between rare nuclei does occur, this review will be limited to ^1H–^1H examples due to their more general interest and applicability.

Following publication of the aforementioned reviews, two limiting problems have been addressed which increase the applicability of this already successful experimental strategy to a wider range of materials. First, insufficient contrast (either spectroscopic chemical shift contrast or dynamic relaxation-based contrast) between many different types of polymers often precludes generation of a polarization gradient and/or detection of its redistribution. In practice, ^{13}C detection of the spin-diffusion process is most amenable to polymeric systems, given the extremely small chemical shift range and large dipolar couplings between abundant ^1H spins. While polymers or blends containing both rigid and mobile regions can easily be interrogated using ^{13}C-detected Goldman-Shen or dipolar filter methods [57], polymer systems with similar molecular dynamics and similar ^1H chemical shifts are difficult to interrogate. Building on a previous 2D ^{13}C exchange experiment employing ^1H spin-diffusion by Spiess and coworkers [58], Schmidt-Rohr and coworkers recently described a triple cross-polarization experiment that correlates individual ^{13}C resonances with one another *via* ^1H spin-diffusion [59]. Figure 20.16 shows the resulting correlation spectra for a blend of polystyrene (PS) and poly(2,6-dimethylphenyleneoxide) (PXE), in which the quantitative extent of spin-diffusion is assessed *via* extraction of specific rows or columns from the 2D contour plot. The method is attractive since no isotopic labeling is required, and the high-resolution characteristic of ^{13}C spectra is preserved in each dimension. Although sensitivity is improved relative to previous multiple cross-polarization experiments by a factor of 4, the overall efficiency is still quite low. In addition, the technique requires long values of $T_{1\rho H}$ (>5 ms), which potentially excludes many polymer systems of interest.

A second problem that has hindered the application of spin-diffusion methods to a broader range of polymeric materials involves the variation in values of spin diffusion coefficients (D) that have been reported in the literature, and the difficulty with experimentally determining D for any sample of interest. Until recently, the strategy for determination of spin-diffusion coefficients in amorphous polymers involved comparisons of static ^1H linewidths (for rigid polymers) or $^1HT_2$ values (for low T_g polymers) to those obtained for well-characterized, model block copolymers [60]. The model block copolymers have either lamellar, cylindrical, or spherical morphologies, as measured by SAXS or electron microscopy. By ratioing the measured values of linewidth or T_2 obtained for the sample of interest to similar parameters in the literature for these standards, appropriately scaled values of the spin-diffusion coefficient may be estimated for the sample. While this approach is viable, and provides accurate values for D in some cases, an alternative strategy in which direct measurement of spin-diffusion rates in the polymers of interest, and calculations of D based on that measurement, would be attractive. Such an approach would be particularly important for polymer systems in which scattering and microscopy contrast is poor or nonexistent, e.g., blends of amorphous polymers with similar chemical structures, or for which well-characterized block copolymers of similar structure and molecular dynamics were not available.

White and coworkers have recently described an experimental approach in which intramonomer spin-diffusion is used to quantitatively define upper limits on the value of spin-diffusion coefficients D in mobile and rigid homopolymers, as well as in copolymers and blends [61–63]. The independent determination of the diffusion coefficient using only NMR data would be possible if a unique, invariant reference volume or distance existed in the polymer sample that could be used to quantitatively define the diffusive length scale. In other words, an internal distance calibration on the sample itself would eliminate the need for independent

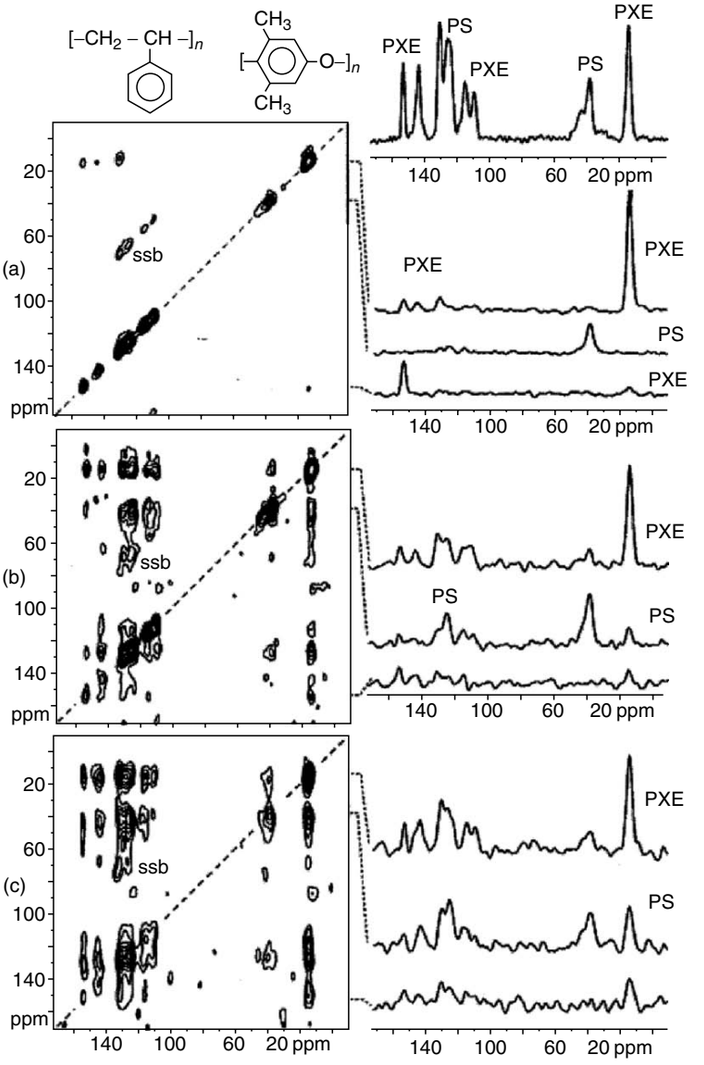

FIGURE 20.16. Series of 2D MAD $^{13}C(HH)^{13}C$ spectra and ^{13}C slices of PS/PXE blends as a function of spin-diffusion mixing time equal to (a) 0.01, (b) 0.5, and (c) 2 ms). [Adapted from Ref. [59] with permission.]

validation of the mixing length scale by scattering or microscopy experiments. White and coworkers reported that the dimensions of the cylinder inscribing a monomer unit in a chain-extended polymer serves as this reference distance, thereby resulting in calculation of an accurate spin-diffusion coefficient in cases where a polarization gradient may be prepared within the monomer itself. While there are several strategies available for generating an initial ^1H polarization gradient in a monomer, particular attention is devoted to using 2D solid-state heteronuclear correlation (Hetcor) methods for measuring intramonomer spin-diffusion in rigid polymers. The main advantage of this experiment is that naturally occurring ^1H magnetization gradients are exploited. In other words, no special manipulation of the proton spin reservoir is required to generate an initial polarization gradient; all local ^1H magnetization is preserved prior to the spin-diffusion period and therefore one can be confident that the sampled spin-response is representative of the bulk. The benefit of the Hetcor spin-diffusion experiment relative to direct ^1H-observe methods is much greater resolution in the ^1H dimension due to ^{13}C chemical shift separation, allowing different polarization-transfer processes (occurring over different length scales) to be detected simultaneously as might occur in blends or block polymers. Figure 20.17 shows example results for a pure glassy homopolymer and amorphous polymer blends.

The two preceding types of experiments directly measure spin-diffusion, i.e., employ a specific mixing time during which spin-diffusion occurs. Several groups have recently employed direct measurement of ^1H spin-diffusion to probe domain sizes in blends containing either polar or nonpolar polymers, inclusion compounds, and composites [64–70].

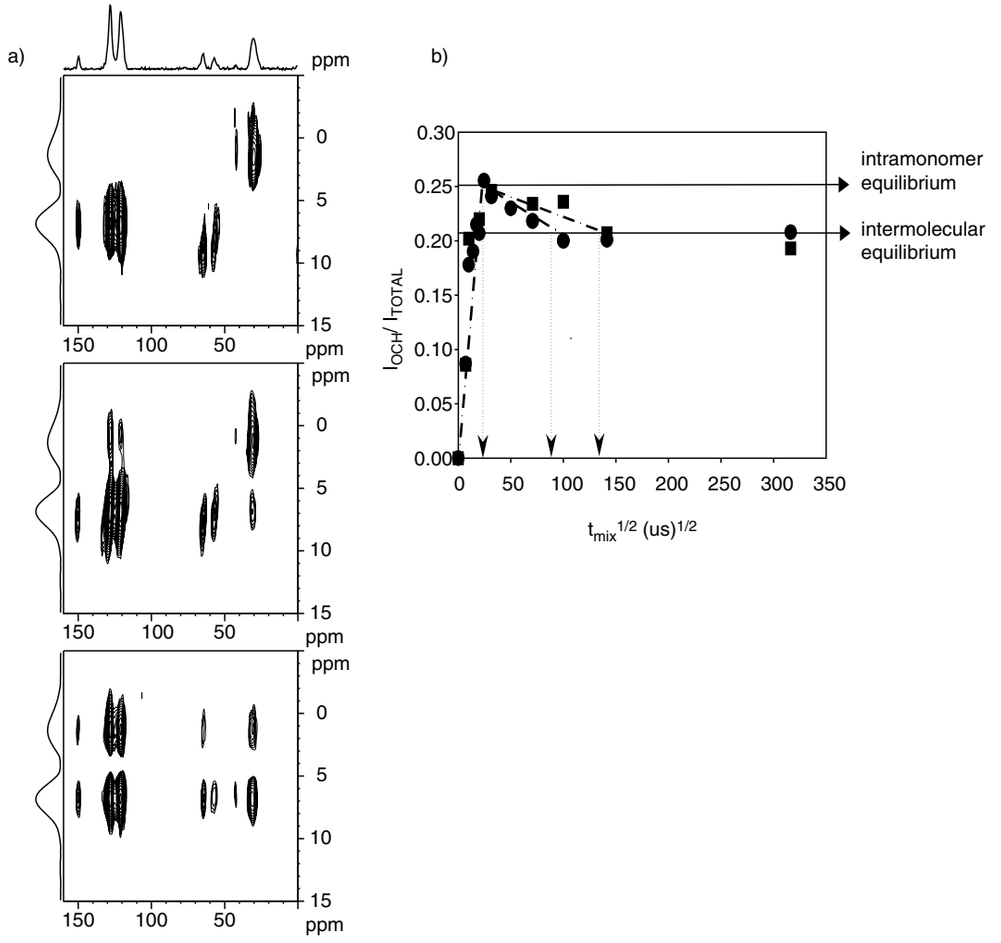

FIGURE 20.17. (a) Series of ^{1}H–^{13}C spin-diffusion Hetcor data for polycarbonate at mixing times of (top) 0 ms, (middle) 0.1 ms, and (bottom) 2.0 ms. (b) Representative spin-diffusion curves extracted from Hector spin-diffusion data, like that in (a), for two different poly(ε-caprolactone)/poly-(L-lactic acid) blends. Note the clear distinction between intramolecular and interchain/interdomain equilibration, the latter occurring at longer times for one blend versus the other. [Adapted with permission from Refs. [62] and [63].

As shown above, ^{1}H spin-diffusion may be detected *via* ^{13}C observation; ^{19}F has also been used to follow ^{1}H spin-diffusion in fluoropolymers [71]. An interesting case of homonuclear spin-diffusion between ^{13}P nuclei has been reported for domain size determination in phosphazene polymers [72]. In general, most researchers still use traditional $^{1}HT_{1\rho}$ and T_1 measurements to indirectly access the limits of spin-diffusion in an approximate fashion, as reported in many recent applications of these methods to a variety of semicrystalline polymers, blends, and composites [73–78].

Chain Packing

As an example of recent developments in the use of solid-state NMR to probe interchain packing relationships, the independent works of Schaefer and Suter deserve mention [79–84]. Polycarbonate (PC) is an industrially important polymer, and its excellent impact properties have been attributed to low-frequency molecular motions which serve as a mechanism for energy dissipation. Using a variety of dipolar recoupling/magic-angle spinning-based techniques, Schaefer and coworkers have found strong evidence for local ordering, or "bundles," in amorphous PC. These bundles are composed of ordered chain pairs over short distances (<10 Å), but the bundles themselves are irregularly spaced/oriented, consistent with the overall glassy structure [79–81]. In contrast, Suter and coworkers used static or slow magic-angle spinning 2D solids NMR to obtain homonuclear dipolar coupling data consistent with a "melt-like" structure with little or no order unless the polymer is mechanically deformed [82–84]. In all cases, direct dipolar couplings were measured between specifically labeled nuclear spins (e.g., ^{13}C, ^{2}H, ^{19}F), and computational structure simulations were used in conjunction with the solid-state NMR data in each approach (Fig. 20.18).

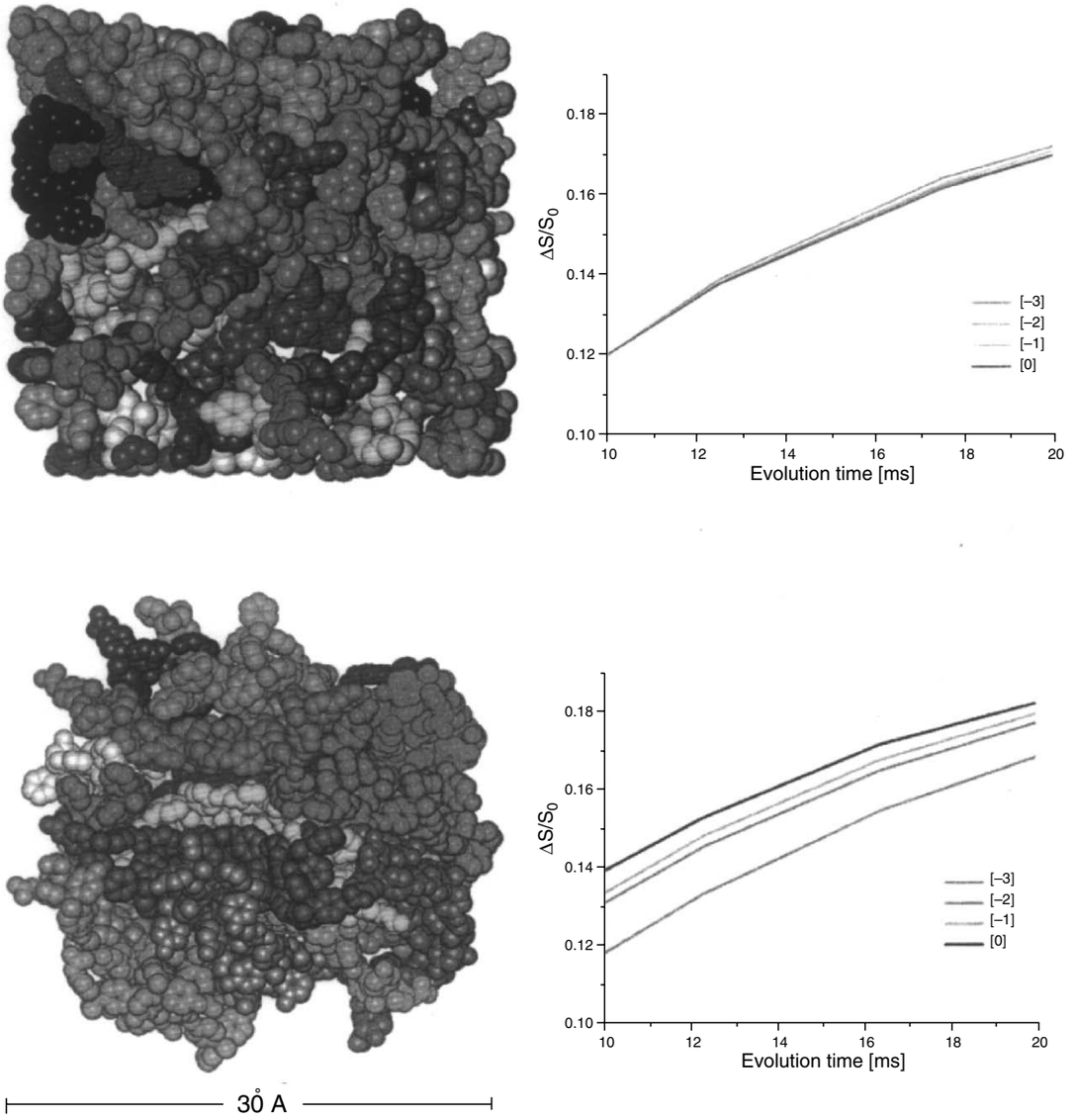

FIGURE 20.18. Comparison of molecular simulations of random (top row) and paired segment (bottom row) chain packing in phenol-substituted polycarbonate, extracted from orientation-dependent REDOR data. [Adapted from Ref. [81] with permission.]

Polymer Dynamics in the Solid State

An excellent review text has recently been published by Tycko outlining various experimental NMR approaches to molecular dynamics, both in small and macromolecules [85]. In terms of the application of these various methods to polymers, one can generally categorize the techniques as direct (e.g., 2D exchange, ^{2}H labeling and lineshape analysis) or indirect (e.g., relaxation, cross-relaxation) probes of molecular dynamics, and additionally, rank them in terms of whether they probe a specific, local type of motion or longer range, correlated chain dynamics. Finally, solid-state NMR experiments can probe an extremely wide range of characteristic timescales for the molecular or chain motion, ranging from nanosecond to many seconds. For example, isolated CH_3 group motion, typically in the form of a tunneling or rotation about the C_3 axis, occurs in essentially all rigid solids, including polymers. As a result, several authors have used methyl groups as ''motional labels'' to interrogate local structure in polymers and blends *via* dipolar or deuterium quadrupolar interactions [86–90]. While the relaxation or cross-relaxation methods measure very fast dynamic events, 2D solid-state exchange techniques are among the most useful for direct inspection of slower events, i.e., on

the order of milliseconds to seconds, which are believed to be most relevant to mechanical properties [91]. Typically, conformational interchange between adjacent segments of the polymer chain, or local substituent reorientations, is accessible by the 2D solid-state exchange technique. References [41–43] contain many examples of ^{13}C, ^{2}H, and ^{31}P 2D exchange data, demonstrating that exchange may be followed between resolved isotropic peaks, similar to traditional solution exchange data, or also within an anisotropically broadened lineshape. Here, we mention only a few more recent examples. Solid-state ^{2}H exchange was used to interrogate the molecular contributions to differential mechanical relaxations in polyacrylates [92], while Horii and coworkers used ^{13}C exchange experiments to determine the activation energy for backbone dynamics in a phenoxy resin [93]. These methods are also useful for interrogation of blend miscibility, as has been recently demonstrated for the case of polyolefin blends [94]. In addition to homonuclear exchange methods, heteronuclear 2D correlation methods, also known as wideline separation (WISE) allow indirect detection of differential chain or side-group dynamics *via* resolved line-shape analysis combined with spin diffusion [95,96].

Two-dimensional exchange techniques offer many advantages for direct detection and analysis of polymer dynamics. However, they often suffer from long acquisition times or insufficient spectral resolution between the polymer chain sites one wishes to interrogate. Several high-resolution one-dimensional methods offer alternatives. Subtle variations in polycarbonate chain dynamics with changes in ring functionalization have recently been reported by Wu *et al*. using heteronuclear dipolar recoupling experiments [97 and references therein]. Hu and coworkers determined that large amplitude chain flips occur in polyethylene crystallites using homonuclear ^{13}C dipolar coupling techniques, in agreement with earlier 2D exchange data [98,99]. These examples illustrate the complimentary information accessible by a variety of dynamic solid-state NMR techniques.

REFERENCES

1. F. A. Bovey, *Nuclear Magnetic Resonance Spectroscopy,* second ed., Academic Press, San Diego, CA, 1988, p. 3.
2. F. A. Bovey and L. W. Jelinski, *Nuclear Magnetic Resonance*, Encyclopedia of Polymer Science, vol. 10, Wiley, New York, 1987, p. 254.
3. F. C. Schilling, F. A. Bovey, M. D. Bruch, and S. H. Kozlowski, *Macromolecules* 1985, *18*, 1418.
4. See Chapter on "Chain Structures" by P. R. Sundararajan in this Handbook.
5. R. C. Ferguson, *ACS Polym. Preprs*. 1967, *8*, 1026.
6. R. C. Ferguson, *Trans. N.Y. Acad. Sci*. 1967, *29*, 495.
7. F. Heatley and A. Zambelli, *Macromolecules* 1969, *2*, 618.
8. J. B. Stothers, *C-13 NMR Spectroscopy,* Academic Press, New York, 1972.
9. K. F. Kuhlman and D. M. Grant, *J. Am. Chem. Soc*. 1968, *90*, 7355.
10. A. E. Derome, *Modern NMR Techniques for Chemistry Research*, Pergamon, New York, 1987.
11. A. E. Tonelli and F. C. Schilling, *Acc. Chem. Res*., 1981, *14*, 233.
12. T. C. Farrar and E. D. Becker, *Pulse and Fourier Transform NMR*, Academic Press, New York, 1987.
13. F. C. Schilling and A. E. Tonelli, *Macromolecules*, 1980, *13*, 270.
14. R. Ditchfield, *Nucl. Magn, Reson*., 1976, *5*, 1.
15. P. V. Schastnev and A. A. Cheremisin, *J. Struct. Chem*., 1982, *23*, 440.
16. J. R. Cheeseman, G. W. Trucks, T. A. Keith, and M. J. Frisch, *J. Chem. Phys*., 1996, *104*, 5497.
17. H. Duddeck, in *Topics in Stereochemistry,* vol. 16, E. I. Eliel, S. H. Wilen, and N. L. Allinger, eds., Wiley-Intersceince, New York, 1986, p. 219.
18. A. E. Tonelli, *NMR Spectroscopy and Polymer Microstructure: The Conformational Connection*, Wiley-Interscience, New York, 1989.
19. H. Spiesecke and W. G. Schneider, *J. Chem. Phys*., 1961, *35*, 722.
20. D. M. Grant and E. G. Paul, *J. Am. Chem. Soc*. 1964, *86*, 2984.
21. L. P. Lindeman and J. Q. Adama, *Anal. Chem*., 1971, *43*, 1245.
22. D. E. Dorman, R. E. Carhart, and J. D. Roberts, in *Proceedings of the International Symposium on Macromolecules, Rio de Janerio, July 26–31, 1974*, E. B. Mano, ed., Elsevier, New York, 1974.
23. F. A. Bovey in *Proceedings of the International Symposium on Macromolecules, Rio de Janerio, July 26–31, 1974*, E. B. Mano, ed., Elsevier, New York, 1974, p. 169.
24. P. J. Flory, *Statistical Mechanics of Chain Molecules*, Wiley-Interscience, New York, 1969.
25. D. M Grant and V. B. Cheney, *J. Am. Chem. Soc*., 1967, *89*, 5315.
26. S. Li and D. B. Chesnut, *Magn. Reson. Chem*., 1985, *23* 625.
27. K. Seidman and G. E. Maciel, *J. Am. Chem. Soc*., 1977, *99*, 659.
28. D. L. VanderHart, *J. Magn. Reson*., 1981, *44*, 117.
29. U. W. Suter and P. J. Flory, *Macromolecules*, 1975, *8*, 765.
30. L. W. Jelinski, *Chem. Eng. News, Nov*, 1984, p. 26.
31. A. Bax, *Two-Dimensional Nuclear Magnetic Resonance in Liquids*, D. Reidel Pub. Co., Hingham, MA, 1982.
32. L. W. Jelinski, in *Chain Structure and Conformation of Macromolecules*, F. A. Bovey, ed., Academic Press, New York, 1982.
33. A. E. Tonelli, *NMR Spectroscopy of Polymers,* R. N. Ibbett, ed., Blackie, Glasgow, 1993.
34. T. M. Duncan and C. R. Dybowski, *Surf. Sci. Repts*., 1981, *1*, 57.
35. G. E. Pake, *J. Chem. Phys*., 1948, *16*, 327.
36. M. Mehring, *High Resolution NMR in Solids*, second ed., Springer-Verlag, Berlin, 1983.
37. E. R Andrews, A. Bradbury, and R. G. Eades, *Nature*, 1959, *183*, 1802.
38. A. Pines, M. G. Gibby, and J. S. Waugh, *J. Chem. Phys*., 1972, *56*, 1776; *Chem. Phys. Lett*., 1972, *15*, 373.
39. Hartman and Hahn, *Phys. Revs*., 1962, *128*, 2042.
40. J. Schaefer and E. O. Stejskal, *J. Am. Chem. Soc*., 1976, *98*, 1031.
41. K. Schmidt-Rohr and H. W. Spiess, *Multidimensional Solid-State NMR and Polymers*, Academic Press, New York, 1994.
42. I. Ando and T. Asakura, *Solid State NMR of Polymers*, Elsevier, Tokyo, 1998.
43. F. A. Bovey and P. A. Mirau, *NMR of Polymers*, Academic Press, New York, 1996.
44. S. P. Brown and H. W. Spiess, *Chem. Rev*, 2001, *101*, 4125.
45. N. Ishihara, T. Seimiya, N. Kuramoto, and M. Uoi, *Macromolecules*, 1986, *19*, 2462.
46. C. Pellecchia, P. Longo, A. Grassi *et al*., *Makromol. Chem. Rapid Commun*., 1987, *8*, 277.
47. A. Immirizi, F. deCandia, P. Ianelli *et al*., *Makromol. Chem. Rapid Commun*., 1988, *9*, 761.
48. O. Greis, Y. Xu, T. Arsano, and J. Peterman, *Polymer*, 1989, *30*, 590.
49. R. A. Nyquist, *Appl. Spectrosc*., 1989, *43*, 440.
50. N. M. Reynolds, J. D. Savage, and S. L. Hsu, *Macromolecules*, 1989, *22*, 2867.
51. M. A. Gomez and A. E. Tonelli, *Macromolecules*, 1990, *23*, 3385.
52. A. Bunn, E. A. Cudby, R. K. Harris *et al*., *J. Chem. Soc*., 1981, *15*.
53. M. G. Dunbar, D. Sandstrom, and K. Schmidt-Rohr, *Macromolecules*, 2000, *33*, 6017.
54. K. Schmidt-Rohr, W. Hu, and N. Zumbulyadis, *Science*, 1998, *280*, 714.
55. D. L. VanderHart and G. M. McFadden, *Solid State NMR*, 1996, *7*, 45.
56. J. Clauss, K. Schmidt-Rohr, and H. W. Spiess *Acta Polym*., 1993, *44*, 1.
57. N. Egger, K. S. Schmidt-Rohr, B. Blumich, W. D. Domke and B. Stapp, *J. Appl. Polym. Sci*., 1992, *44, 289*.
58. M. Wilhelm, H. Feng, U. Tracht, and H. W. Spiess, *J. Magn. Reson*., 1998, *134*, 255.

59. S. S. Hou, Q. Chen, and K. Schmidt-Rohr, *Macromolecules*, 2004, *37*, 1999.
60. F. Mellinger, M. Wilhelm, and H. W. Spiess, *Macromolecules*, 1999, *32*, 4686.
61. X. Wang and J. L. White *Macromolecules*, 2002, *35*, 3795.
62. X. Jia, J. Wolak, X. Wang, and J. L. White, *Macromolecules*, 2003, *36*, 712.
63. X. Jia, X. Wang, A. E. Tonelli, and J. L. White, *Macromolecules*, 2005, 38, 2775.
64. K. Beshah and L. K. Molnar, *Macromolecules*, 2000, *33*, 1036.
65. T. M. Werkhoven, F. M. Mulder, C. Zune, R. Jerome, and H. J. M. de Groot, *Macromol. Chem. Phys*., 2003, *204*, 46.
66. W. G. Hu and K. Schmidt-Rohr, *Polymer*, 2000, *41*, 2979.
67. K. Landfester, V. L. Dimonie, and M. S. El-Aasser, *Macromol. Chem. Phys*., 2002, *203*, 1772.
68. P. A. Mirau, S. A. Heffner, and M. Schilling, *Solid State NMR*, 2000, *16*, 47.
69. A. Buda, D. E. Demco, M. Bertmer, B. Blumich, B. Reining, H. Keul, and H. Hocker, *Solid State NMR*, 2003, *24*, 39.
70. W. Heinen and H. J. M. deGroot, *Macromolecules*, 1998, *31*, 7404.
71. P. Holstein, G. A. Monti, and R. K. Harris, *Phys. Chem. Chem. Phys*., 1999, *1*, 3549.
72. S. Taylor, J. L. White, R. Crosby, G. C. Campbell, N. Elbaum, J. F. Haw, and G. Hatfield, *Macromolecules*, 1992, *25*, 3369.
73. C. Neagu, J. E. Puskas, M. A. Singh, and A. Natansohn, *Macromolecules*, 2000, *33*, 5976.
74. J. Z. Yi and S. H. Goh, *Polymer*, 2003, *44*, 1973.
75. P. J. M. Serrano, J. P. M. van Duynhoven, R. J. Gaymans, and R. Hulst, *Macromolecules*, 2002, *35*, 8013.
76. A. E. Tonelli, *J. Mol. Struct*., 1995, *355*, 105.
77. M. I. B. Tavares, *J. Appl. Polym. Sci*., 2003, *87*, 473.
78. N. J. Clayden, *J. Appl. Polym. Sci*., 1994, *32*, 2321.
79. C. A. Klug, W. Zhu, K. Tasaki, and J. Schaefer, *Macromolecules*, 1997, *30*, 1734.
80. J. M. Goetz, J. Wu, A. F. Yee, and J. Schaefer, *Macromolecules*, 1998, *31*, 3016.
81. R. D. O'Conner, B. Poliks, D. H. Bolton, J. M. Goetz, J. A. Byers, K. L. Wooley, and J. Schaefer, *Macromolecules*, 2002, *35*, 2608.
82. P. Robyr, Z. Gan, and U. W. Suter, *Macromolecules*, 1998, *31*, 6199.
83. M. Utz, A. S. Atallah, P. Robyr, A. H. Widmann, R. R. Ernst, and U. W. Suter, *Macromolecules*, 1999, *32*, 6191.
84. M. Utz, P. Robyr, and U. W. Suter, *Macromolecules*, 2000, *33*, 6808.
85. R. Tycko, *Nuclear Magnetic Resonance Probes of Molecular Dynamics*, Kluwer Academic Press, The Netherlands, 1994.
86. J. L. White and P. A. Mirau, *Macromolecules*, 1993, *26*, 3049.
87. K. Saalwachter, *Chem. Phys. Lett*., 2002, *362*, 331.
88. M. Wachowicz, J. Wolak, H. Gracz, E. O. Stejskal, S. Jurga, and J. L. White, *Macromolecules*, 2004, *37*, 4573–4579.
89. W. Lin and F. D. Blum, *J. Am. Chem. Soc*., 2001, *123*, 2032.
90. K. Schmidt-Rohr, A. S. Kulik, H. W. Beckham, A. Ohlemacher, and H. W. Spiess, *Macromolecules*, 1994, *27*, 4733.
91. X. Qiu and M. D. Ediger, *J. Polym. Sci. B: Polym. Phys*., 2000, *38*, 2634.
92. S. C. Kubler, D. J. Schaefer, C. Boeffel, U. Pawelzik, and H. W. Spiess, *Macromolecules*, 1997, *30*, 6597.
93. H. Kaji, T. Tai, and F. Horii, *Macromolecules*, 2001, *34*, 6318.
94. J. E. Wolak, X. Jia, and J. L. White, *J. Am. Chem. Soc*., 2003, *125*, 13660.
95. K. Schmidt-Rohr, J. Clauss, and H. W. Spiess, *Macromolecules*, 1992, *25*, 3273.
96. X. Qiu and P. A. Mirau, *J. Magn. Reson*, 2000, *142*, 183.
97. J. Wu, C. Xiao, A. F. Yee, J. M. Goetz, and J. Schaefer, *Macromolecules*, 2000, *33*, 6849.
98. W. G. Hu, C. Boeffel, and K. Schmidt-Rohr, *Macromolecules*, 1999, *32*, 1611.
99. K. Schmidt-Rohr and H. W. Spiess, *Macromolecules*, 1991, *24*, 5288.

CHAPTER 21

Broadband Dielectric Spectroscopy to Study the Molecular Dynamics of Polymers Having Different Molecular Architectures

F. Kremer

Universität Leipzig, Germany

21.1 INTRODUCTION

Broadband dielectric spectroscopy (BDS) is a versatile experimental tool to study the dynamics of polymeric systems. In its modern form it covers the extraordinary frequency range from 10^{-3} Hz to 10^{9} Hz with the option to extend both limits to lower and higher values, respectively. This enables one to analyse the molecular dynamics on a large time scale especially if the temperature of the sample is varied as well. In the present review article examples will be discussed for polymers of widely varying molecular architectures (linear and cyclic chains, star-branched systems, and liquid crystalline polymers).

21.2 BROADBAND DIELECTRIC SPECTROSCOPY (BDS)

In principle in a dielectric experiment [1a,b] an electric field is applied to a material under study and the resulting polarisation current is measured (Fig. 21.1). It is composed out of two contributions, the induced (time constant $\cong 10^{-12}$s) and the orientational polarisation (time constant $> 10^{-12}$s). Modern broadband dielectric measurements are carried out in the frequency domain. The sample geometry has to be adapted to the spectral range in which the measurements are carried out (Fig. 21.2).

Dielectric spectra are usually fitted by the empirical relaxation function suggested by Havriliak and Negami:

$$\varepsilon^*(\omega) = \varepsilon_\infty + \frac{\Delta\omega}{\left(1 + (i\omega\tau_{\mathrm{HN}})^{\beta}\right)^{\gamma}} \qquad (21.1)$$

in which $\Delta\varepsilon$ is the relaxational strength, τ_{HN} the mean relaxation time and ε_∞ the value of the real part of the dielectric function in the limit $\omega \gg \frac{1}{\tau_{\mathrm{HN}}}$. The parameters β and γ describe the symmetric and asymmetric broadening of the relaxation time distribution function. Details are discussed in Chapter 3 of [1a].

21.3 THE DYNAMICS OF POLYMERS HAVING DIFFERENT MOLECULAR ARCHITECTURES

21.3.1 Linear and Cyclic Chains of Poly(methylphenylsiloxane)

The fact that poly(methylphenylsiloxane) (PMPS) has a dielectrically active relaxation process originates from the dipole moment of the Si–O bond [2]. Due to the chemical structure of PMPS (Fig. 21.3) the dipole components in the main axis of the polymer cancel each other, while they add up in the perpendicular direction.

Thus, one has to expect *one* dielectric relaxation process, assigned to a local motion of the Si–O bond. It corresponds to the dynamic glass transition (α-relaxation) of the bulk polymer. Measured from temperatures between -25 °C to 33 °C this relaxation process shifts from about 1 Hz to about 10^{8} Hz (Fig. 21.4).

On the low-frequency side the measurement is limited by a conductivity contribution, on the high frequency side by

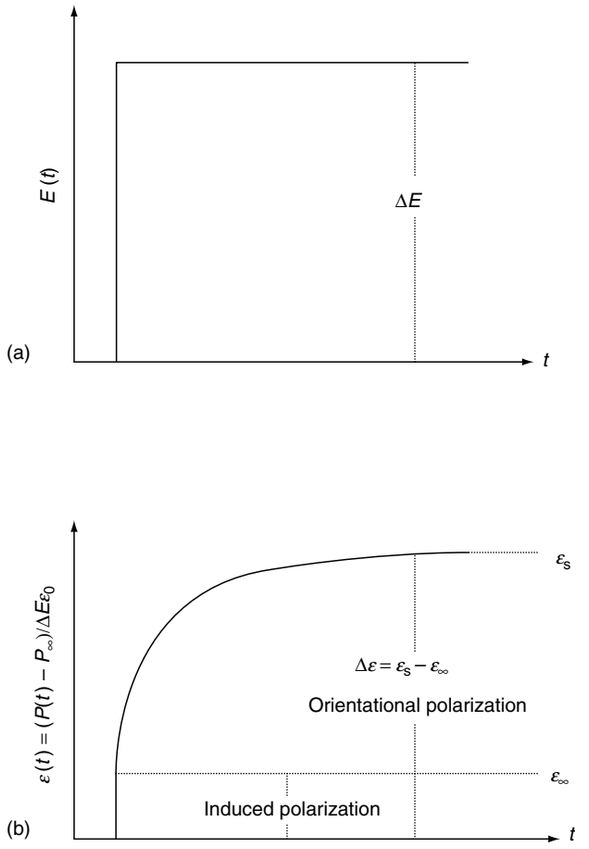

FIGURE 21.1. Scheme of time dependence of the electric field $E(t)$ and the resulting polarisation being composed out of the induced and the orientational contribution.

resonance effects of the sample cell. In order to deduce the mean relaxation rate and the shape parameter of the relaxation time distribution from the measured data the ansatz of Havriliak-Negami in Eq. (21.1) is used. The experimental data can be described by this fit-function within experimental accuracy—over the entire frequency range (Fig. 21.5) leading to the fit parameters listed in Table 21.1. The latter shows a pronounced temperature dependence proving that time-temperature superposition is *not* fulfilled for this system.

The temperature dependence of the mean relaxation time τ_{HN} can be described by the empirical function according to Williams, Landel and Ferry (WLF):

$$\log a_{\mathrm{T}} = \frac{C_1(T - T_0)}{C_2 + T - T_0}. \tag{21.2}$$

Here a_{T} is a shift factor ($a_\tau = \tau_{\mathrm{HN}}/\tau_{\mathrm{reference}}$). If for $1/\tau_{\mathrm{reference}}$ the relaxation rate at the glass transition temperature is chosen $C_1 = 11.8\,\mathrm{K}$ and $C_2 = 67.9\,\mathrm{K}$ is obtained. The WLF dependence is typical for the dynamic glass transition (Fig. 21.6). It covers nearly 10 decades in the relaxation rate and scales with the calorimetric glass transition temperature as $\tau(T_{\mathrm{g}}) \simeq 10^{-2}\,\mathrm{Hz}$. The dynamic glass transition

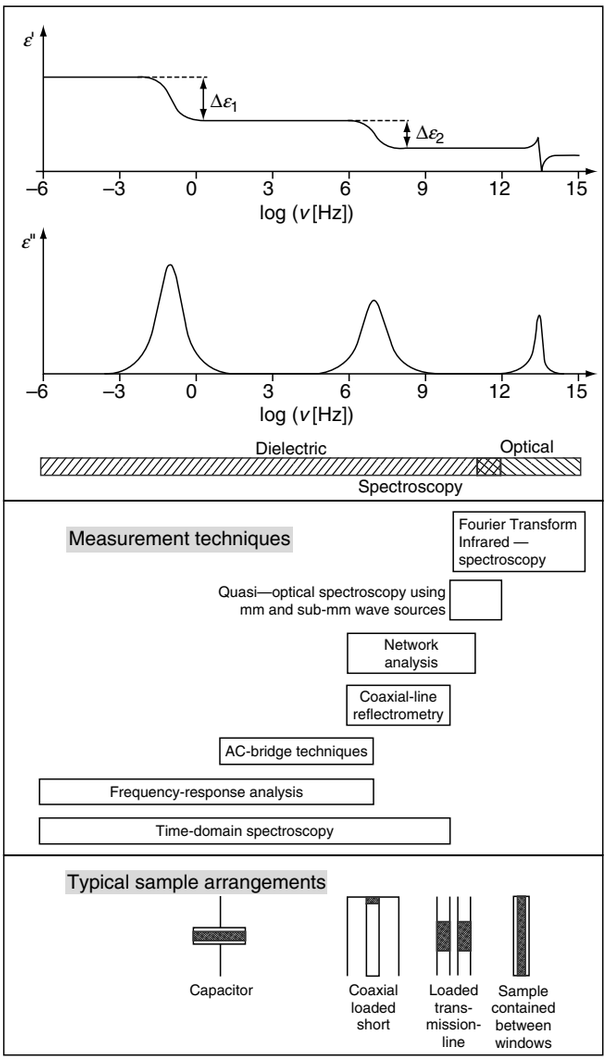

FIGURE 21.2. Survey of measurement techniques used in the frequency range from 10^{-6} Hz–10^{15} Hz. Taken from [1a] with permission.

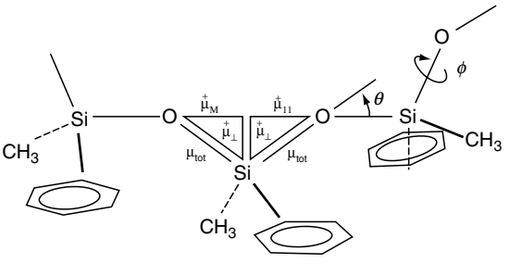

FIGURE 21.3. Chemical structure of poly(methylphenylsiloxane). Taken from [2] with permission.

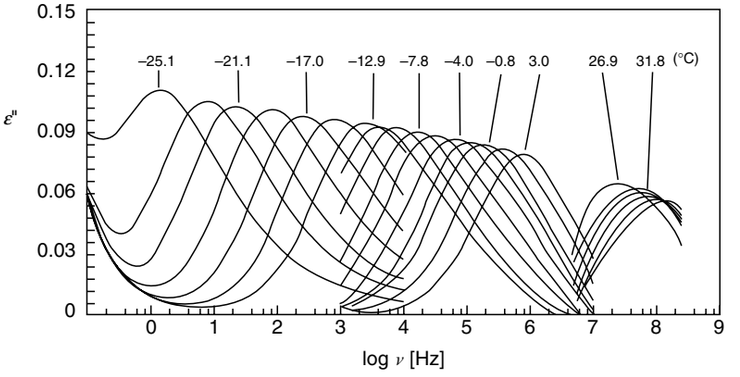

FIGURE 21.4. Dielectric loss $\varepsilon''(\nu)$ versus frequency for PMPS ($M_n = 28500$ with $T_g = -26$ °C) at different temperatures as indicated. The accuracy of the measurement of the dielectric loss is $\pm$ 5% in the low frequency region; above 1 MHz the measurement accuracy is $\pm$ 10%. Taken from [2] with permission.

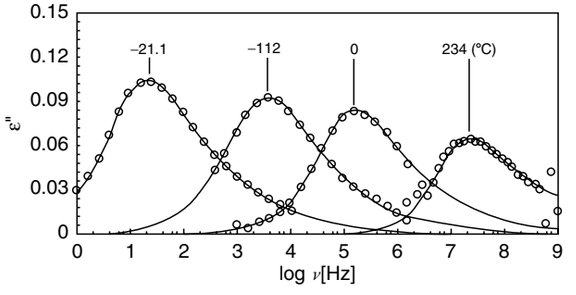

FIGURE 21.5. Data from Fig. 21.4 as fitted (solid line) using the Havriliak-Negami equation [Eq. (21.1)]. The fit parameters are shown in Table 21.1. Taken from [2] with permission.

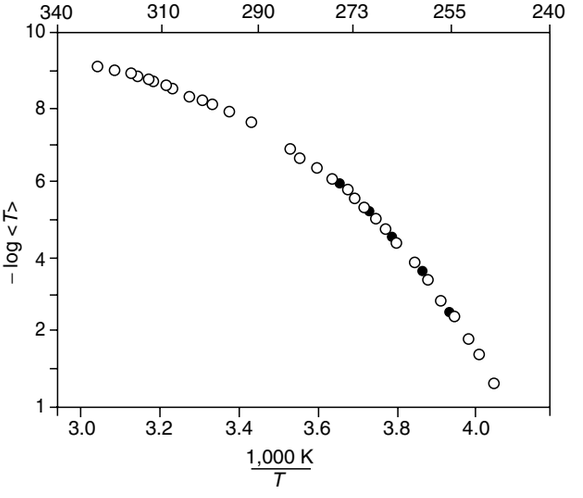

FIGURE 21.6. Plot of the logarithm of the mean relaxation times vs. the reciprocal temperature. The open symbols (○) denote the dielectric data, the solid symbols (●) are the results obtained by quasielastic light scattering. Taken from [2] with permission.

TABLE 21.1. *Temperature dependence of the HN-fit parameters (s. Eq. (21.1)) for the segmental relaxation of poly(methylphenylsiloxane) having a molecular weight of* $M_n = 28{,}500$.

T [C]	$\Delta\varepsilon_{HN}$	β	γ	τ_{HN} [s]
−22.8	0.42	0.76	0.56	4.7×10^{-2}
−21.1	0.41	0.80	0.46	1.7×10^{-2}
−19.1	0.40	0.82	0.43	5.1×10^{-3}
−17.0	0.40	0.84	0.39	1.7×10^{-3}
−11.2	0.35	0.76	0.56	7.6×10^{-5}
−9.7	0.35	0.77	0.55	4.1×10^{-5}
−7.8	0.34	0.83	0.46	2.3×10^{-5}
−6.0	0.34	0.85	0.43	1.3×10^{-5}
−4.0	0.34	0.89	0.36	7.1×10^{-6}
0	0.31	0.85	0.46	2.1×10^{-6}
23.4	0.25	0.96	0.34	1.7×10^{-8}
28.7	0.25	0.99	0.29	1.1×10^{-8}

is assigned to fluctuations of an ensemble of 2–3 segments between structural substates.

The temperature at a relaxation rate of 1 Hz shows a pronounced dependence on the molecular weight M_n and the molecular architecture (Fig. 21.7). While linear polymers follow the Fox–Flory equation this is not the case for cyclic systems.

21.3.2 Linear and Star-Branched Chains of Poly(*cis*-1,4-isoprene)

Poly(*cis*-1,4-isoprene) has due to the lack of symmetry in its chemical structure (Fig. 21.8) non-zero components of

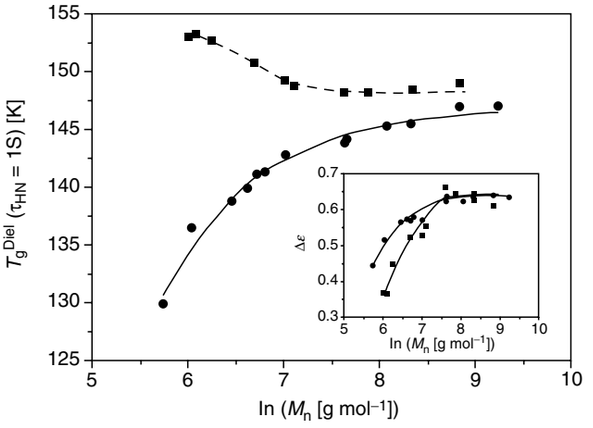

FIGURE 21.7. T ($\tau_{HN} = 1$ s) versus molecular weight: ●, linear chains; ■, rings; the solid line is a fit of Fox/Flory equation to the data ($T_{g,\infty} = 147$ K,K = 5057 K mol g^{-1}), the dashed line is a guide for the eyes. The inset shows $\Delta\varepsilon$ versus molecular weight at T = 298 K: ●, linear chains; ■, rings, lines are guides for the eyes. All data are taken from [4].

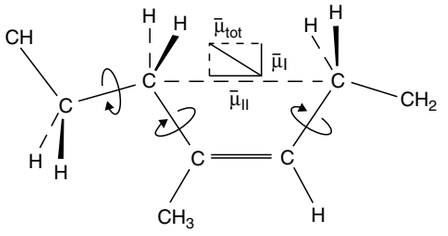

FIGURE 21.8. Chemical structure and dipole moment of poly(*cis*-1,4-isoprene).

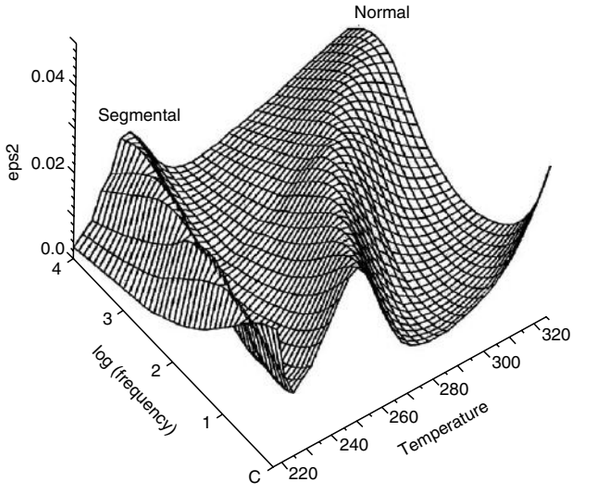

FIGURE 21.9. 3D representation of the frequency and temperature dependence of the dielectric loss ε'' for *cis*-1,4-polyisoprene PIP-12. Taken from [5b] with permission.

the dipole moment both perpendicular and parallel to the chain axis.

Thus *two* dielectric relaxation processes, a segmental and a normal mode process, are present [5]; they are well-separated on the frequency and temperature scale (Fig. 21.9). The relaxation process around 220 K originates from a local segmental motion perpendicular to the main axis, while the second relaxation process at higher temperatures is assigned to fluctuations of the dipole components parallel to the chain contour (normal mode).

It is to expect that the segmental mode does not depend on the molecular weight of the chain (Fig. 21.10). In contrast

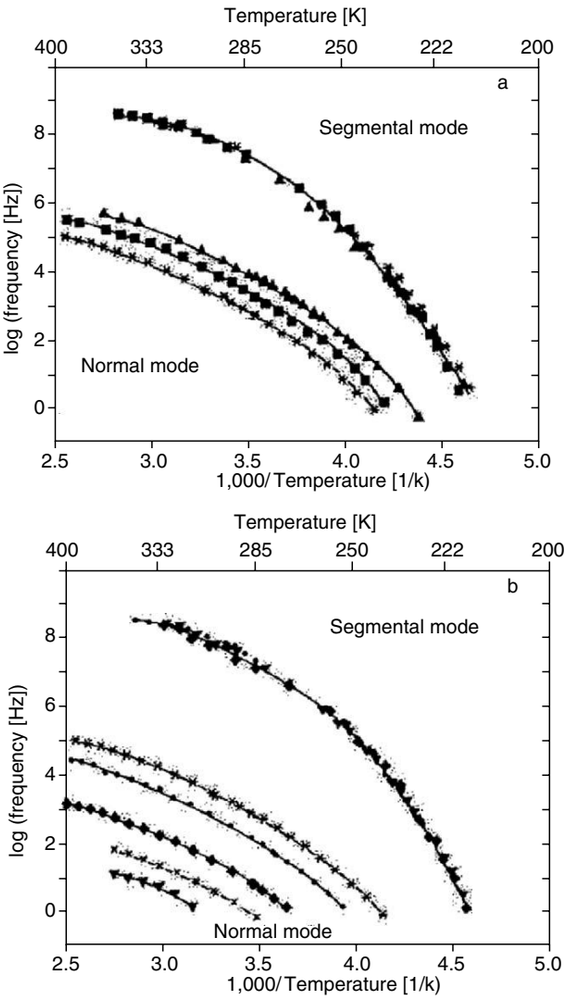

FIGURE 21.10. (a) Activation plot for the segmental mode and the normal mode of *cis*-1,4-polyisoprene samples with molecular weights of $M_w < M_c$: ▲, PIP-05; ■, PIP-08; **x**, PIP-12. The solid lines represent the WLF fit with the fit parameters given in Table 21.3. (b) Activation plot for the segmental mode and the normal mode of *cis*-1,4-polyisoprene samples with molecular weights of $M_w > M_c$: *, PIP-12; ●, PIP-17; ◆, PIP-38; ★, PIP-65; ▼, PIP-97. The solid lines represent the WLF fit with the fit parameters given in Table 21.3. Taken from [5a] with permission.

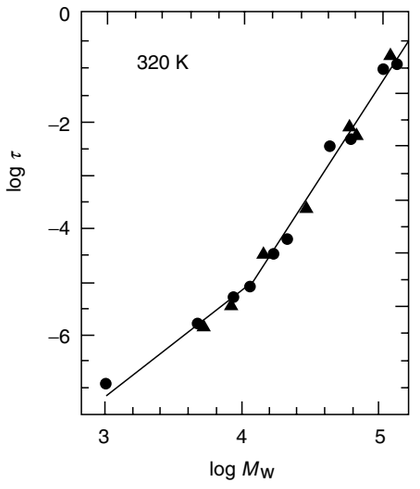

FIGURE 21.11. Dependence of the mean dielectric relaxation time, $\tau = (2\pi\nu_{max})^{-1}$, on molecular weight, M_w, for the normal mode process of *cis*-1,4-polyisoprene (▲) at 320 K; data are reported by Adachi and Kotaka (●) in [5a]. Taken from [5b] with permission.

TABLE 21.2. *Temperature dependence of the HN-fit parameters (s. Eq. (21.1)) for the segmental and normal mode of linear poly(cis-1,4-isoprene) having a molecular weight of* 17,000 gmol^{-1} *[5a].*

T [K]	$\Delta\varepsilon_{HN}$	β	γ	τ_{HN} [s]
			Segmental Mode	
222.3	0.117	0.70	0.50	2.2×10^{-2}
224.3	0.115	0.68	0.51	8.7×10^{-3}
226.4	0.114	0.65	0.55	3.0×10^{-3}
229.5	0.111	0.65	0.56	8.8×10^{-4}
240.4	0.097	0.64	0.59	2.2×10^{-5}
244.4	0.097	0.64	0.68	8.5×10^{-6}
253.9	0.091	0.62	0.66	9.0×10^{-7}
			Normal Mode	
263.9	0.127	1.0	0.38	4.6×10^{-2}
272.5	0.118	1.0	0.40	1.2×10^{-2}
283.7	0.105	1.0	0.42	3.5×10^{-3}
297.7	0.096	1.0	0.44	9.4×10^{-4}
324.4	0.085	1.0	0.45	1.3×10^{-4}
341.7	0.082	1.0	0.45	6.1×10^{-5}
359.4	0.078	1.0	0.44	3.2×10^{-5}
376.6	0.077	1.0	0.44	2.0×10^{-5}

the normal mode must depend sensitively on the molecular weight M_W: The critical molecular weight M_c where Rouse-like fluctuations change into a reptation-like dynamics has for PI a value of 10^4. Thus one finds

$$\begin{matrix} \langle\tau\rangle \infty\ M^{2.0} \text{ for } M_w < M_c \\ \langle\tau\rangle \infty M^{3.7\pm0.1} \text{ for } M_w \geq M_c \end{matrix} . \qquad (21.3)$$

These molecular weight dependencies are explained by the Rouse theory and by the reptation theory in its recent modifications.

As for PMPS the data can be fitted within the limits of experimental accuracy by the empirical HN-function. The fit parameters (Table 21.2) for the normal and segmental mode of PI having a molecular weight of 17,000 g mol^{-1} show that the distribution parameters β and γ are strongly temperature dependent. This means that again the conjecture of time-temperature superposition is *not* fulfilled.

Both, the segmental and the normal mode can be described in its temperature dependence by the WLF-equation (Eq. (21.2)). While the former is only weakly dependent on temperature, the normal mode shows especially for the parameter C_2 a strong effect (Tab. 21.3). Star-branched polymers of PI have in principle similar dynamics as linear chains: Two relaxation processes are observed being assigned to the segmental and normal mode. Linear chains have free ends in

TABLE 21.3. *WLF-fit parameters of the segmental and the normal mode of linear PI having molecular weight varying between* $M_w = 1{,}000$ *(PI-01) to* $M_w = 130{,}000$ *(PI-130) [5a].*

	Segmental mode $T_0 = 250$ K			Normal mode $T_0 = 300$ K		
Code	C_1	C_2 [K]	$10^{-5}\nu_0$ [Hz]	C_1	C_2 [K]	ν_0 [Hz]
PIP-01				4.0	151.6	2.0×10^6
PIP-05	5.7	80.0	1.2	4.0	133.9	3.1×10^4
PIP-08	5.7	70.0	2.1	4.3	136.2	7.4×10^3
PIP-12	5.8	76.0	2.5	4.2	132.3	2.0×10^3
PIP-13	5.8	74.3	2.2	4.2	128.8	1.3×10^3
PIP-14	6.0	69.7	1.5	4.4	130.5	8.1×10^2
PIP-17	6.1	70.9	1.4	4.4	129.5	3.9×10^2
PIP-38	6.0	71.2	1.6	4.2	119.9	2.2×10^1
PIP-65	6.1	73.4	1.7	3.6	97.5	3.1
PIP-97	6.1	70.9	1.4	0.9	57.9	0.02
PIP-130	6.1	72.5	1.6			

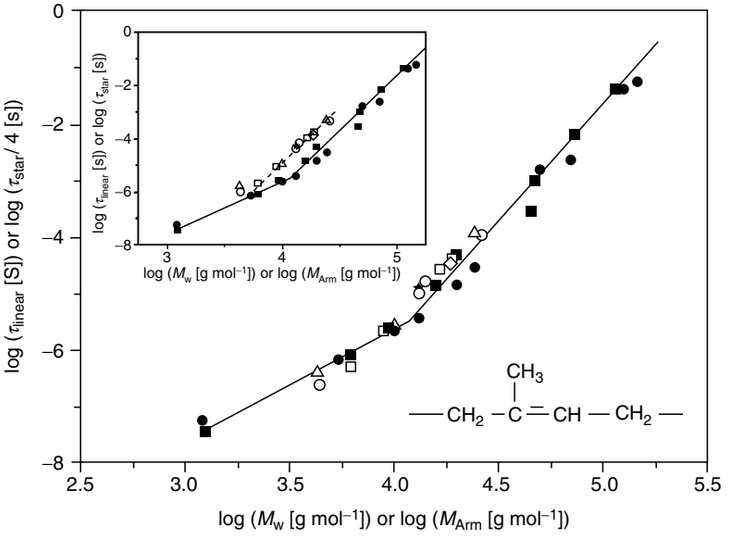

FIGURE 21.12. τ_{Linear} and $\tau_{Star}/4$ versus molecular weight of the chain or the arm of different linear and star-like poly(*cis*-1,4-isoprene)s at $T = 320$ K. The inset shows τ_{Linear} and τ_{Star} versus molecular weight of the chain or the arm. ●, linear chains [5a]; ■, linear chains [5b]; ○, 18-arm star; Δ, 12-arm star; □, 8-arm star; ◇, 4-arm star, *, 3-arm star. The solid lines are linear fits for $M < M_C$ (Slope 2.0, Rouse regime) and $M > M_C$ (Slope 3.7, reptation regime). The dashed line is a parallel shift of the line obtained for the reptation regime for the data of the stars polymers. Taken from [1a] with permission.

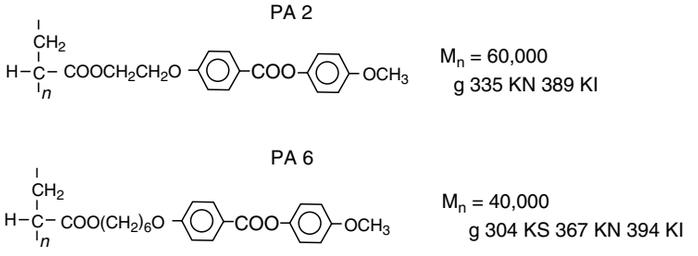

FIGURE 21.13. Scheme of the side group liquid crystalline polymer.

contrast to star-branched polymers where an arm of the system has to be comprehended as a tethered chain, which is fixed at one end. This leads to special boundary conditions for the normal mode relaxation resulting in a scaling factor of 1/4 for the relaxation rate (Fig. 21.12).

21.3.3 Liquid Crystalline Polymers

Mesogenic groups can be incorporated into polymeric systems [7]. This results in materials of novel features like main chain systems of extraordinary impact strength, side-chain systems with mesogens which can be switched in their orientation by external electric fields or—if chiral groups are attached to the mesogenic units—ferroelectric liquid crystalline polymers and elastomers. The dynamics of such systems depends in detail on its molecular architecture, i.e. especially the main chain polymer and its stiffness, the spacer molecules and their length and the mesogenic unit broadband dielectric spectroscopy enables one to unravel in detail the molecular and—for chiral systems—as well the collective fluctuations.

In side chain liquid crystalline polymers the mesogenic unit is connected to the main chain by a flexible spacer. The molecular fluctuations of the rigid mesogenic core are characterised by two librational modes, one corresponding to fluctuations around the long molecular axis (“β-relaxation”) and a libration around the short molecular axis (“δ-relaxation”). Additionally the mesogens might have an attached polar group causing a further secondary process (“γ-relaxation”). Usually the main chain has a dynamic glass transition corresponding to fluctuations of chain segments between structural substates (“α-relaxation”).

For a side chain liquid crystalline polymer [8] with a poly(acrylate) main chain and a 2- or 6-fold aliphatic spacer (Fig. 21.13) one finds three relaxation processes: The β-relaxation, the δ-relaxation, and the dynamic glass

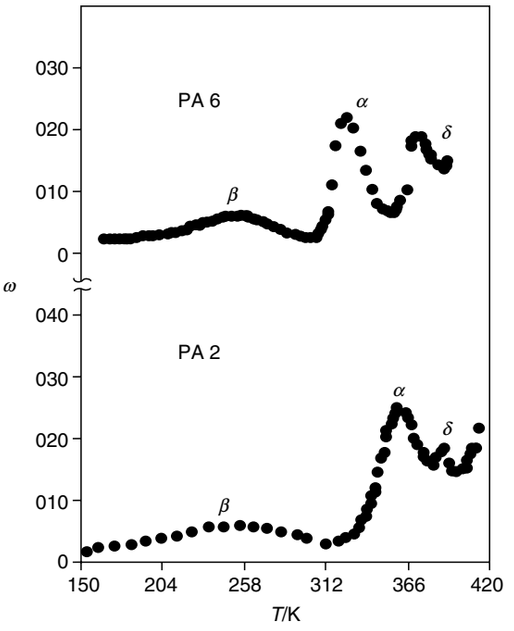

FIGURE 21.14. Dielectric loss versus temperature at 10 kHz. Sample: PA2 and PA6 (both unaligned). The error bars in this and the following figures are not larger than the size of the symbols. Taken from [8] with permission.

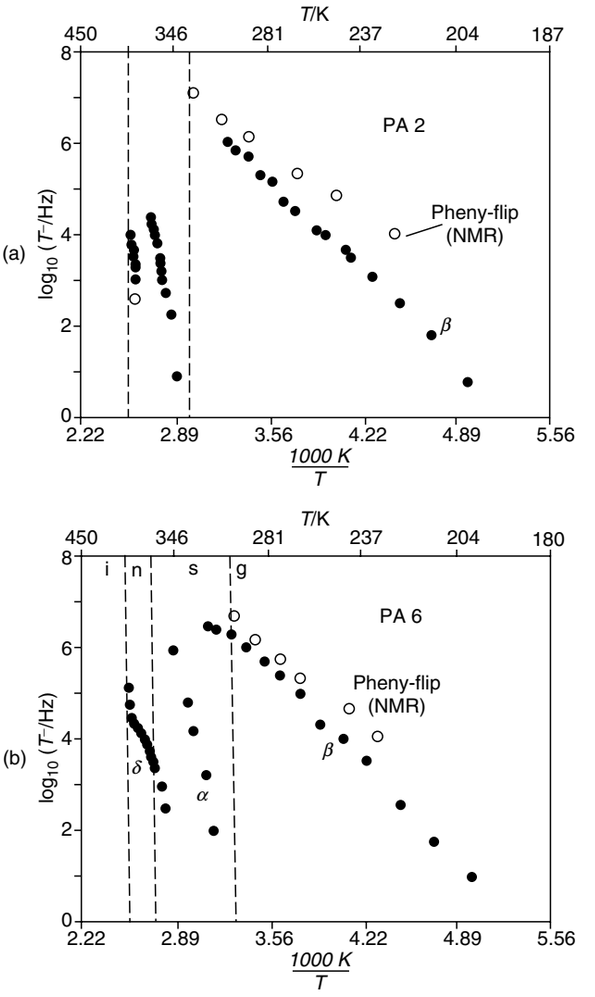

FIGURE 21.15. (a) Activation plot (relaxation rates versus inverse temperature) for unaligned PA2. ●, dielectric measurements; ○, NMR measurement for 180° phenyl-flip. (b) Activation plot (relaxation rate versus inverse temperature) for unaligned PA6. ●, dielectric measurements; ○, NMR data for the 180° phenyl-flip. Taken from [8] with permission.

transition (“α-relaxation”) (Fig. 21.14). The temperature dependence of these fluctuations is summarised in activation plots (Fig. 21.15). It is remarkable that the change from a two-fold (PA2) to a six-fold (PA6) spacer has such a strong influence on the dynamics. The δ-relaxation shows at the phase transition into the isotropic state a pretransitional change of its temperature dependence. The fluctuations in this side chain system are schematically sketched in Fig. 21.16.

For a combined main chain side group liquid crystalline polymer (Fig. 21.17) two librational β-relaxations are observed [9] originating from the two different mesogenic units (Fig. 21.18).

A δ-relaxation is not found, presumably due to the high viscosity of the system and an underlying conductivity contribution. If the sample with a chiral group in the side chain mesogen is oriented in the bookshelf geometry a completely novel dynamics takes place due to the ferroelectric order of the mesogenes [10]. One observes two collective processes a soft-mode and a Goldstone-mode corresponding to fluctuations of the phase and the amplitude of the helical superstructure (Fig. 21.19). Additionally one finds in the frequency range between 10^6 and 10^9 Hz a secondary β-relaxation being assigned to librations around the long molecular axis. This refined dynamic interplay is schematically summarised in Fig. 21.20.

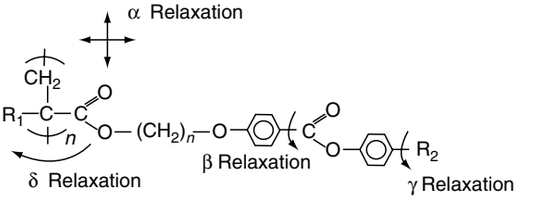

FIGURE 21.16. Scheme of the liquid–crystalline side group polymers and the fluctuations which were observed in the measurements (indicated by arrows). Taken from [8] with permission.

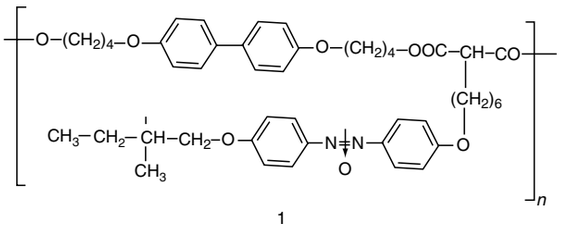

1

FIGURE 21.17. Scheme of combined main chain/side group liquid crystalline polymer. Molar mass $M = 23{,}000\,g/mol^{-1}$. Phase transition temperatures in K: S_j^* 350 S_c^* 391 S_A^* 404I.

21.3.4 Conclusions

Broadband dielectric spectroscopy enables one to analyse the dynamics of polar groups in polymeric systems. Due to its broad frequency range of more than 10 decades a manifold of different molecular fluctuations can be studied from the dynamic glass transition (spanning already more than 10 decades in times) to secondary relaxations. Additionally one finds in chiral liquid crystals cooperative processes like soft- and Goldstone modes.

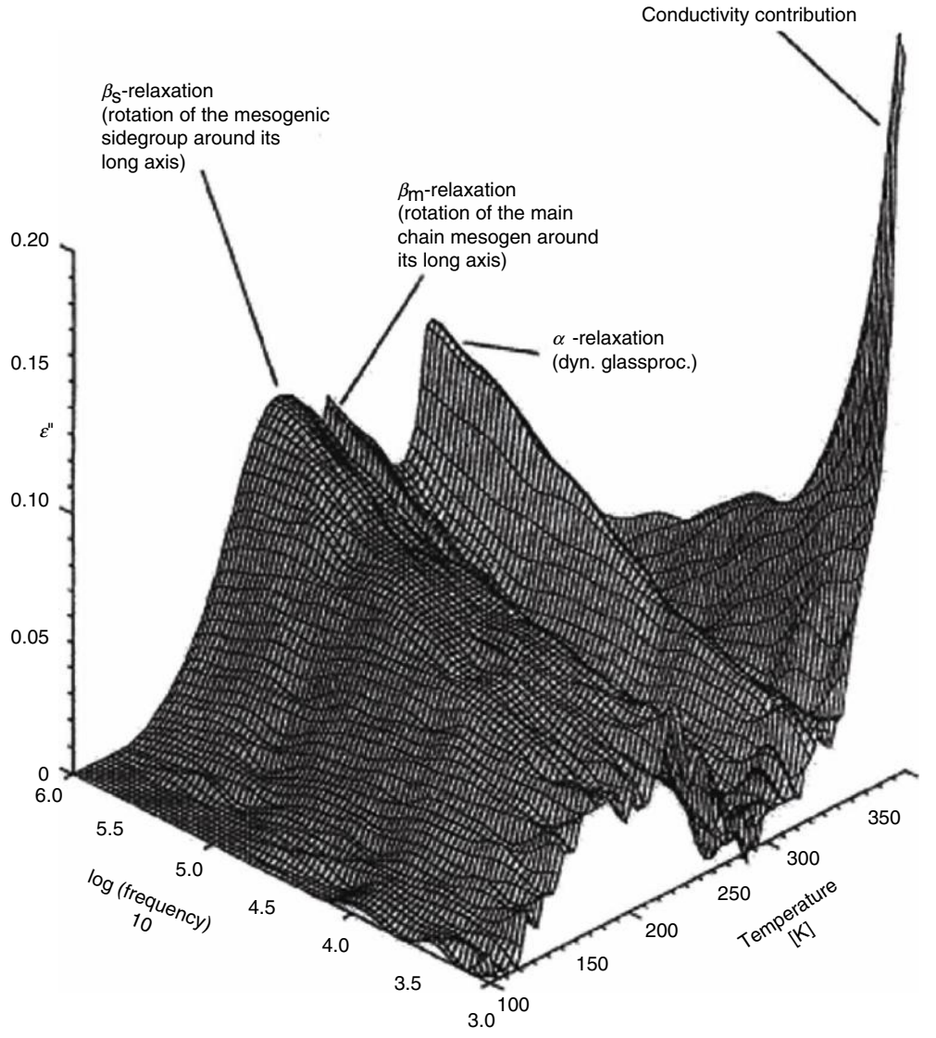

FIGURE 21.18. Dielectric loss ε'' versus temperature and logarithm of frequency using an *unaligned* (200 μm thick) sample (Fig. 21.17) (only dielectric relaxation processes are observable). Taken from [9] with permission.

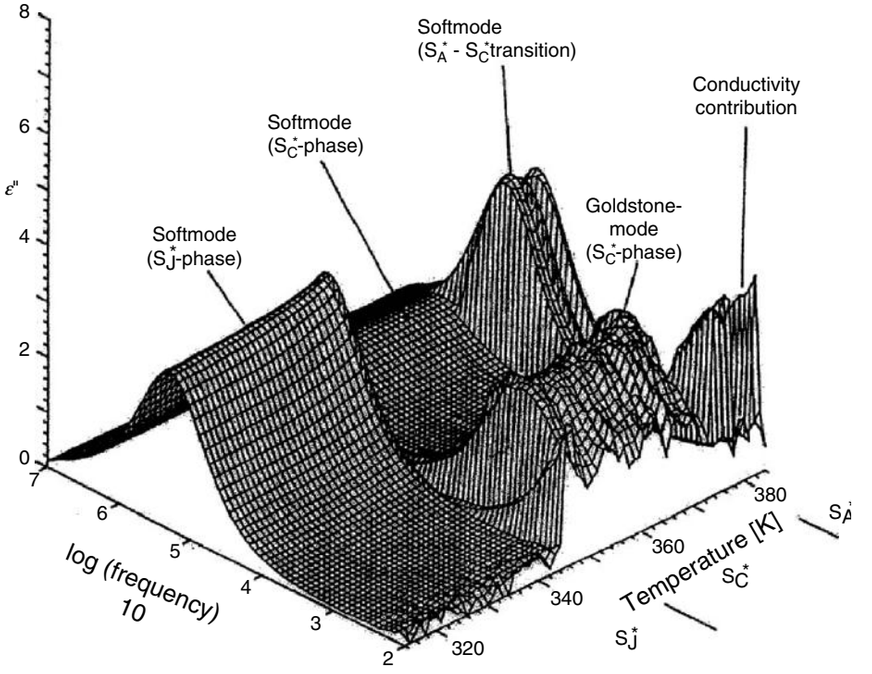

FIGURE 21.19. Dielectric loss ε'' versus temperature and logarithm of frequency using a thin (10 μm) *aligned* sample (ferroelectric modes are observable). Note the different ε''-scale as compared with Fig. 21.18. Taken from [10] with permission.

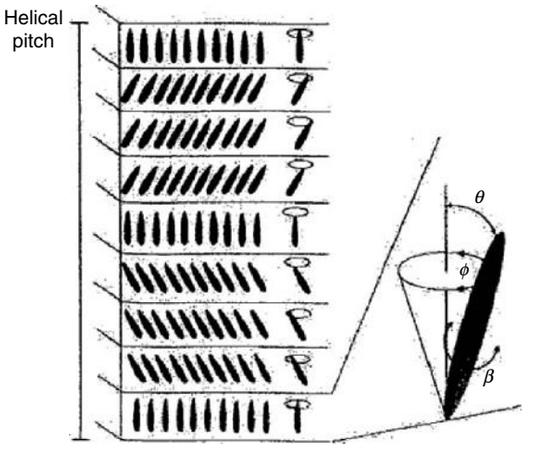

FIGURE 21.20. Scheme of the collective and molecular dynamics in FLC: The Goldstone-mode corresponds to fluctuations of the phase Φ (phason) and the soft-mode of the amplitude θ (amplitudon) of the helical superstructure. The high frequency β-relaxation is assigned to librations of the mesogen around its long molecular axis.

REFERENCES

1a. Kremer F, Schönhals A (Eds) (2002) In: Broadband Dielectric Spectroscopy. Springer, Berlin, Heidelberg, New York
1b. McCrum NG, Read BE, Williams G (1967) In: Anelastic and Dielectric Effects in Polymeric Solids. Dover Publications, New York
2. Boese D, Momper B, Meier G, Kremer F, Hagenah JU, Fischer EW (1989) Macromolecules 22: 4416
3. Kremer F, Boese D, Meier G, Fischer EW (1989) Prog. Colloid Polym. Sci. 80: 129
4. Kirst U, Kremer F, Pakula T, Hollingshurst J (1994) J. Colloid Polym. Sci. 272: 1420
5a. Adachi K, Kotaka T (1985) Macromolecules 18: 466
5b. Boese D, Kremer F (1990) Macromolecules 23: 829
6a. Boese D, Kremer F, Fetters LJ (1990) Macromolecules 23: 1826
6b. Boese D, Kremer F, Fetters LJ (1990) Polymer 31: 1831
7. Spiess HW, Vill V (1998) In: Handbook of Liquid Crystals. Demus D, Groby J, Webray G (Eds) Wiley-VCH, Vol. 3
8. Vallerien SU, Kremer F, Boeffel C (1989) Liquid Cryst. 4: 79
9. Kremer F, Vallerien SU, Zentel R, Kapitza H (1989) Macromolecules 22: 4040
10. Vallerien SU, Zentel R, Kremer F, Kapitza H, Fischer EW (1989) Makromol. Chem. Rapid. Commun. 10: 333

CHAPTER 22

Group Frequency Assignments for Major Infrared Bands Observed in Common Synthetic Polymers

I. Noda*, A. E. Dowrey†, J. L. Haynes*, and C. Marcott†

*The Procter & Gamble Company, Beckett Ridge Technical Center, 8611 Beckett Road, West Chester, OH 45069
†The Procter & Gamble Company, Miami Valley Innovation Center, 11810 E. Miami River Rd., Cincinnati, OH 45252

22.1 INFRARED SPECTROSCOPY OF POLYMERS

Infrared (IR) spectroscopy plays a very important role in the physical characterization of polymers. IR absorption bands are well known for their marked specificity to individual chemical functionalities. Furthermore, the unique sensitivity toward the configuration, conformation, and other local sub- and supramolecular environments (e.g., different phases of semicrystalline polymers, moieties participating in specific interactions of miscible blends, and block polymer segments undergoing different stages of relaxation processes) makes IR spectroscopy a very powerful probing tool for numerous scientific investigations in polymer physics.

One of the limitations of IR spectroscopy often cited by polymer physicists has been the lack of unambiguous band assignments of chemical moieties for IR spectra of different polymers. The assignment of IR absorption bands for specific modes of molecular vibrations in polymers is not always straightforward. While, it is true there have been numerous published IR spectroscopic studies of polymeric materials, relatively little is provided for the useful and practical tabulation of specific group-frequency band assignments for typical synthetic polymers commonly studied by polymer physicists.

In this section, mode assignments of IR absorption bands for 24 selected solid polymers most often encountered by polymer physicists are compiled. Only frequencies of relatively well-assignable bands actually observed at room temperature are listed. No attempts were made to include information on intensity or band shape. IR bands can be strongly affected by various physical factors such as phase, morphology, sample history, and IR sampling techniques. Tables 22.1–22.24 are intended for physicists interested in

TABLE 22.1. *Polyethylene, linear [1–9].*

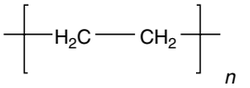

Frequency (cm^{-1})	Phase	Transition moment orientation[a]	Assignment
720	Crystalline	∥ *b*-axis	Out-of-phase CH_2 rock of the two chains in the unit cell
	Amorphous	⊥ *b*-axis	CH_2 rock $(tttt)_n$ $n > 4$
731	Crystalline	∥ *a*-axis	In-phase CH_2 rock of the two chains in the unit cell
888	Amorphous	∥	CH_2 rock
1,050	Crystalline	∥	CH_2 twist
1,078	Amorphous	⊥	Skeletal C–C stretch (*g* and *t* confirmation)
1,176	Crystalline	∥	CH_2 wag

TABLE 22.1. *Continued.*

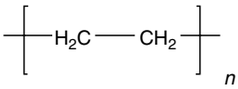

Frequency (cm^{-1})	Phase	Transition moment orientation[a]	Assignment
1,303	Amorphous	∥	CH_2 wag (*gtg* conformation)
1,353	Amorphous	∥	CH_2 wag (*gtg* conformation)
1,368	Amorphous	∥	CH_2 wag (*gtg* conformation)
1,463	Crystalline	∥ *b*-axis	CH_2 bend
	Amorphous		CH_2 bend
1,473	Crystalline	∥ *a*-axis	CH_2 bend
1,820	Crystalline	∥	Combination of 1,100 or 1,130 + 720, 730 (weak)
1,894	Crystalline	⊥	Combination of CH_2 rock, 1,168 + 720, 730 (weak)
2,016	Both	∥	Combination of 1,294 + 720, 730 (weak)
2,150	Both	⊥	Combination of CH_2 1,440 + 720, 730 (weak) or 1,100 + 1,050
2,850			CH_2 symmetric stretch
2,918			CH_2 symmetric stretch

[a]With respect to uniaxial stretch.

TABLE 22.2. *Polyethylene, linear low density [23].*

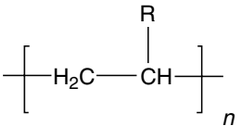

$R = CH_3$ (methyl)
$R = CH_2CH_3$ (ethyl)
$R = CH_2CH_2CH_2CH_3$ (*n*-butyl)
$R = CH_2CH_2CH_2CH_2CH_3$ (*n*-hexyl)
$R = CH_2CH_2CH_2CH(CH_3)CH_3$ (Isobutyl)

Frequency (cm^{-1})	Assignment
720/730	CH_2 deformation (rock) split when PE is crystalline
937	CH_3 rock
890	*n*-hexyl rock
894	*n*-butyl rock
920/952	Isobutyl rock
1,365.5	Isobutyl symmetrical
1,375	CH_3 symmetric deformation
1,377	Methyl symmetrical
1,378.1	*n*-butyl symmetrical
1,377.9	*n*-hexyl symmetrical
1,379	Ethyl symmetrical
1,383.6	Isobutyl symmetrical
1,475/1,462	CH_2 deformation (scissors) split when PE is crystalline
2,850	CH_2 symmetric C–H stretch
2,916	CH_2 asymmetric C–H stretch

TABLE 22.3. *Polypropylene, isotactic [1–3,7,10].*

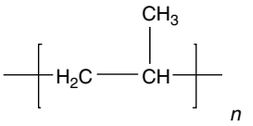

Frequency (cm^{-1})	Species[a]	Phase	Polarization[b]	Assignment
809	*E*	Crystalline	⊥	CH_2 rock + C–C chain stretch + C–CH stretch
841	*A*	Crystalline	∥	CH_2 rock + C– CH_3 stretch
899	*E*	Crystalline	⊥	CH_3 rock + CH_3 rock + CH bend
941	*E*	Crystalline	⊥	CH_3 rock + C–C chain stretch
973	*A*	Amorphous	∥	CH_3 rock + C–C chain stretch
998	*A*	Crystalline	∥	CH_3 rock + CH_3 wag + CH bend
1,045	*A*	Crystalline	∥	C– CH_3 stretch C–C chain stretch + CH bend
1,104	*E*	Crystalline	⊥	C–C chain stretch + CH_3 rock + CH_2 wag + CH twist + CH bend
1,168	*A*	Crystalline	∥	C–C chain stretch + CH_3 rock + CH bend
1,220	*E*	Crystalline	⊥	CH_2 twist + CH bend + C–C chain stretch
1,256	*A*	Both	∥	CH bend + CH_2 twist + CH_3 rock
1,377	*E*	Both	⊥	CH_3 symmetric bend + CH_2 wag
1,458				CH_2 scissors
2,837				CH_2 symmetric stretch
2,868				CH_3 symmetric stretch
2,919				CH_2 asymmetric stretch
2,951				CH_3 asymmetric stretch

[a] *A* species are vibrating in phase and *E* species have a phase difference $2p/3$ between adjacent monomer unit.
[b] With respect to helix.

TABLE 22.4. *Poly(tetrafluoroethylene) [2,9,10].*

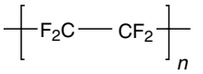

Frequency (cm^{-1})	Assignment
516	C–C–F bend
553	CF_2 bend
636	C–C–F bend
1,150	CF_2 stretch + CF_2 bend (?)
1,210	CF_2 symmetric stretch
1,240	CF_2 asymmetric stretch
2,450	Combination of CF_2 stretch

TABLE 22.5. *Polybutadiene [1,2].*

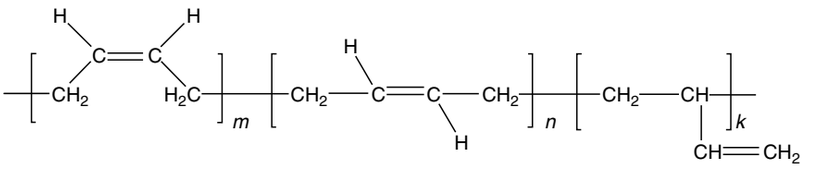

Frequency (cm^{-1})	Repeating unit type	Assignment
730	*cis*-1,4	In-phase out-of-plane CH wag
910	1,2	In-phase out-of-plane CH_2 wag

TABLE 22.5. *Continued.*

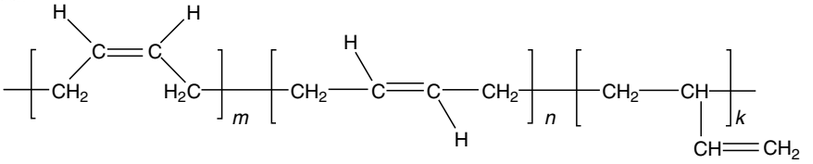

Frequency (cm^{-1})	Repeating unit type	Assignment
967	*trans*-1,4	In-phase out-of-plane CH wag
990	1,2	In-phase out-of-plane CH wag
1,230	*trans*-1,4	CH_2 wag
1,310	*cis*-1,4	CH_2 wag
1,437	*trans*-1,4	CH_2 bend
1,451	*cis*-1,4	CH_2 bend
1,640	1,2	C=C stretch
1,655	*cis*-1,4	C=C stretch
1,820	1,2	Overtone of CH_2 wag
2,840		Backbone CH_2 symmetric stretch
2,916		Backbone CH_2 asymmetric stretch
2,965	1,2	Vinyl CH_2 symmetric stretch
3,000		Olefinic CH stretch
3,065	1,2	Vinyl CH_2 asymmetric stretch

TABLE 22.6. *Polyisoprene, cis [1–3,15,19].*

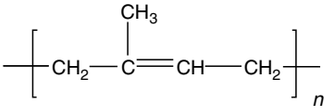

Frequency (cm^{-1})	Assignment
836	Trisubstituted olefin out-of-plane CH wag[a]
1,129	CH_3 rock
1,300	CH_2 wag
1,376	CH_3 symmetric (umbrella) deformation
1,450	CH_2 symmetric (scissors) + CH_3 asymmetric deformation
1,664	C=C stretch
2,720	Overtone of CH_2 umbrella
~ 2,850	CH_2 and CH_3 symmetric stretch
2,920	CH_2 asymmetric stretch
2,962	CH_3 asymmetric stretch
3,030	Olefin CH stretch

[a]Intensity increases with crystallinity.

TABLE 22.7. *Poly(dimethyl siloxane) [1,2].*

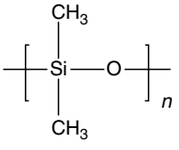

Frequency (cm^{-1})	Assignment
800	CH_3 rock
1,000–1,150	Si–O–Si stretch
1,260	CH_3 symmetric (umbrella) deformation
2,905	CH_3 symmetric stretch
2,960	CH_3 asymmetric stretch

TABLE 22.8. *Poly(ethylene terephthalate) [1,3,10–13].*

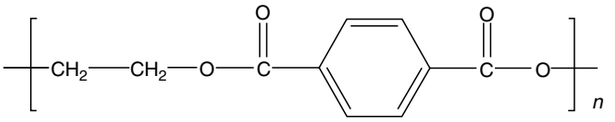

Frequency (cm^{-1})	Phase	Polarization	Assignment
730		⊥	Aromatic in-phase CH wag
795		⊥	C═O rock + –C–O deformation
875	Crystalline	⊥	Aromatic out-of-plane CH wag
896	Amorphous	∥	Gauche configuration CH_2 rock
975	Both	∥	Trans configuration C–O stretch
1,019		∥	Aromatic ring in-plane CH bend
1,102–1,127			C–O stretch + others
1,260			C–O stretch
1,343	Crystalline	∥	CH_2 wag
1,410			Ring semicircle stretch
1,504			Ring semicircle stretch
1,725		⊥	C═O stretch
2,969			CH_2 asymmetric stretch

TABLE 22.9. *Poly(lactic acid) [24].*

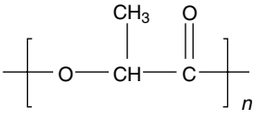

Frequency (cm^{-1})	Assignment
716	Skeletal vibration
755	Skeletal vibration
812	C–C–O stretch
870	O–H deformation
1,048	Symmetric C–O stretch (ether)
1,092	Asymmetric C–O stretch (ether)
1,132	Symmetric C–O stretch (ester)
1,184	Asymmetric C–O stretch (ester)
1,268	O–H deformation w/C–O stretch
1,364	CH_3 symmetric deformation
1,384	CH_3 symmetric deformation
1,456	CH_3 asymmetric deformation
1,759	C═O stretch
2,881	CH_3 symmetric stretch
2,948	CH_3 asymmetric stretch
2,997	CH_3 asymmetric stretch
3,506	O–H stretch (acid terminator)

TABLE 22.10. *Poly(vinyl chloride) [1–3,14,15].*

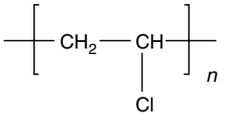

Frequency (cm^{-1})	Phase	Polarization	Assignment
603	Crystalline	∥ (⊥)[a]	C–Cl stretch
610	Amorphous	⊥	C–Cl stretch, syndiotactic segment . . . *ttt* . . .

TABLE 22.10. *Continued.*

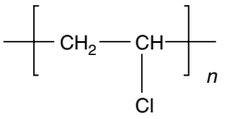

Frequency (cm^{-1})	Phase	Polarization	Assignment
620	Amorphous	⊥	C–Cl stretch, isotactic segment (*tg*)*tt*(*gt*)
685	Amorphous	⊥	C–Cl stretch, isotactic segment (*tg*)*tg*(*tg*)
693	Amorphous	∥	C–Cl stretch, syndiotactic segment (*tt*)*gg*(*tt*)
957	Crystalline	∥ (⊥)[a]	CH_2 rock
970	Amorphous	⊥	CH_2 rock
1,243	Amorphous	⊥	CH bend
1,254	Crystalline	∥ (⊥)[a]	CH bend
1,333	Crystalline	⊥	CH bend
1,354	Crystalline	∥ (⊥)[a]	CH_2 wag
1,424	Crystalline	⊥	
1,431	Amorphous	⊥	CH_2 symmetric (scissors) deformation
2,837			CH_2 symmetric stretch
2,904			CH_2 asymmetric stretch
2,965			CH stretch next to Cl (?)

[a](⊥) Dichroism observed at high draw ratios.

TABLE 22.11. *Poly(vinyl alcohol) [24].*

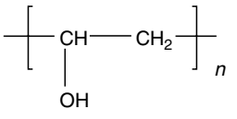

Frequency (cm^{-1})	Assignment
851	C–C–O stretch (alcohol)
945	C–C–O stretch (acetate)
1,026	CH_3 rock
1,096	C–O stretch
1,138	CH_2 deformation (twist or wag)
1,255	C–O stretch (acetate)
1,324	CH deformation (wag)
1,375	CH_3 symmetric deformation (acetate)
1,433	CH_2 deformation (scissors) coupled with O–H deformation (alcohol)
1,734	C=O stretch (acetate)
2,940	CH_2 asymmetric stretch (C–H stretch)
3,360	O–H stretch (alcohol)

TABLE 22.12. *Polyacrylonitrile [3].*

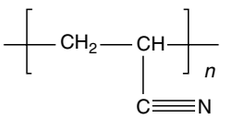

Frequency (cm^{-1})	Polarization	Assignment
1,247		CH bend
1,358		CH_2 asymmetric bend
1,452	⊥	CH_2 bend
2,241	⊥	C ≡ N stretch

TABLE 22.12. *Continued.*

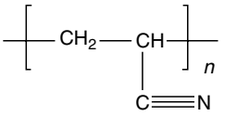

Frequency (cm^{-1})	Polarization	Assignment
2,243		C ≡ N stretch
2,870	⊥	CH_2 symmetric stretch
2,940	⊥	CH_2 asymmetric stretch

TABLE 22.13. *Poly(vinyl acetate) [1,2].*

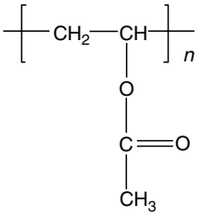

Frequency (cm^{-1})	Assignment
1,022	C–O stretch
1,239	C–O stretch
1,373	CH_3 symmetric (umbrella) deformation
1,432	CH_2 symmetric (scissors) deformation
1,737	C=O stretch
2,850	CH_2 symmetric stretch
2,920	CH_2 asymmetric stretch
2,970	CH_3 asymmetric

TABLE 22.14. *Poly(methyl methacrylate) [1,2,9,16].*

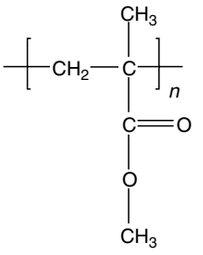

Frequency (cm^{-1})	Assignment
753	Skeletal $+CH_2$ rock
841, 964	Skeletal
988	C–O–C stretch
1,150, 1,195	C–O stretch
1,241, 1,277	C–O stretch
1,387	CH_3 symmetric (umbrella) deformation
1,448	CH_2 symmetric (scissors) deformation, O–CH_3 deformation
1,485	CH_3 (α-methyl) asymmetric deformation
1,732	C=O
2,850	Overtone of ester CH_3 deformation
2,950	CH_3 (ester methyl) stretch
2,998	CH_3 (α-methyl) stretch

TABLE 22.15. *Polystyrene, atactic [1,2,9,17].*

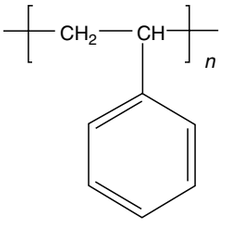

Frequency (cm^{-1})	Assignment
540	Out-of-plane ring bend
697	Mono-substituted ring out-of-plane bend
758	Mono-substituted ring in-phase H wag
1,029	Ring in-phase CH bend
1,220	Ring in-phase CH bend
1,454	Ring semicircle stretch + CH_2 symmetric (scissors) deformation
1,494	Ring semicircle stretch
1,601	Ring quadrant stretch
2,850	CH_2 symmetric stretch
2,924	CH_2 asymmetric stretch
3,000 ~ 3,100	Aromatic CH stretch

TABLE 22.16. *Polysulfone [1,22].*

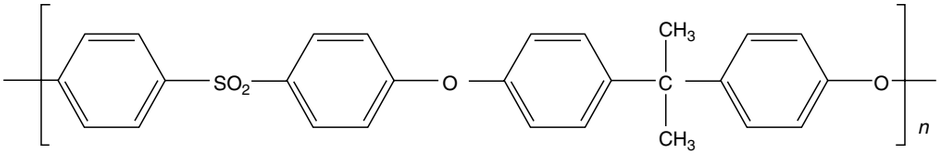

Frequency (cm^{-1})	Assignment
560	SO_2 scissors deformation
690	Aromatic ring bend
834	*Para* out-of-plane aromatic CH wag, two adjacent Hs
1,014	*Para* in-plane aromatic CH bend
1,105	*Para* in-plane aromatic CH bend
1,151	SO_2 symmetric stretch
1,175	SO_2 symmetric stretch
1,244	Aryl-*O*-aryl C–O stretch
1,294	SO_2 asymmetric stretch
1,325	SO_2 asymmetric stretch
1,365	CH_3 symmetric (umbrella) deformation
1,410	*Para* aromatic ring semicircle stretch
1,490	*Para* aromatic ring semicircle stretch
1,505	*Para* aromatic ring semicircle stretch
1,585	*Para* aromatic ring quadrant stretch
2,875	CH_3 symmetric stretch
2,970	CH_3 asymmetric stretch
3,000–3,200	Aromatic CH stretches

TABLE 22.17. *Polycarbonate [1,22].*

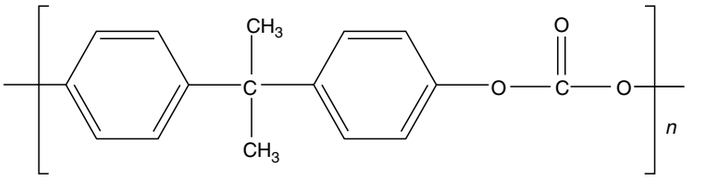

Frequency (cm^{-1})	Assignment
830	*Para* out-of-plane aromatic CH wag, two adjacent Hs
1,015	*Para* in-plane aromatic CH bend
1,080	$(CH_3)_2$ rock/ C–C stretch
1,160	Carbonate C–O stretch
1,193	Carbonate C–O stretch
1,230	Carbonate aryl-*O*-aryl C–O stretch
1,362	CH_3 symmetric (umbrella) deformation
1,405	*Para* aromatic ring semicircle stretch
1,505	*Para* aromatic ring semicircle stretch
1,600	*Para* aromatic ring quadrant stretch
1,775	Carbonate C=O stretch
2,875	CH_3 symmetric stretch
2,970	CH_3 asymmetric stretch
3,000–3,200	Aromatic CH stretches

TABLE 22.18. *Poly(vinyl methyl ether) [1,18].*

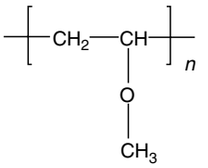

Frequency (cm^{-1})	Assignment
785	CH_2 rock
950	C–O–C symmetric stretch
1,090	C–O–C asymmetric stretch (ether)
1,189	CH_3 rock
1,381	CH_3 deformation
1,460	CH_2 symmetric (scissors) deformation
2,830	O–CH_3 symmetric stretch
2,934	CH_2 asymmetric stretch
2,970	CH_3 asymmetric stretch

TABLE 22.19. *Poly(ethylene oxide) [1,2,20,21].*

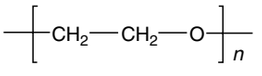

Frequency (cm^{-1})	Assignment
840	C–O–C symmetric stretch, CH_2 rock
947	CH_2 rock
963	CH_2 rock
1,102	C–O–C asymmetric stretch
1,345	CH_2 wag
1,467	CH_2 symmetric (scissors) deformation
2,883	CH_2 asymmetric stretch

TABLE 22.20. *Polyvinylpyrrolidone [1,22].*

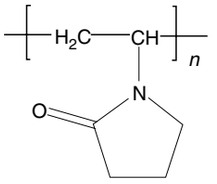

Frequency (cm^{-1})	Assignment
750	CH_2 rock
1,285	C–N stretch
1,420	CH_2 symmetric scissors deformation (CH_2 next to C=O)
1,460	CH_2 symmetric scissors deformation
1,490	CH_2 symmetric scissors deformation (CH_2 next to N)
1,680	Cyclic amide C=O stretch
2,880	CH_2 symmetric stretch
2,920	CH_2 asymmetric stretch
2,951	Cyclic CH_2 asymmetric stretch

TABLE 22.21. *Cellulose acetate [1,22].*

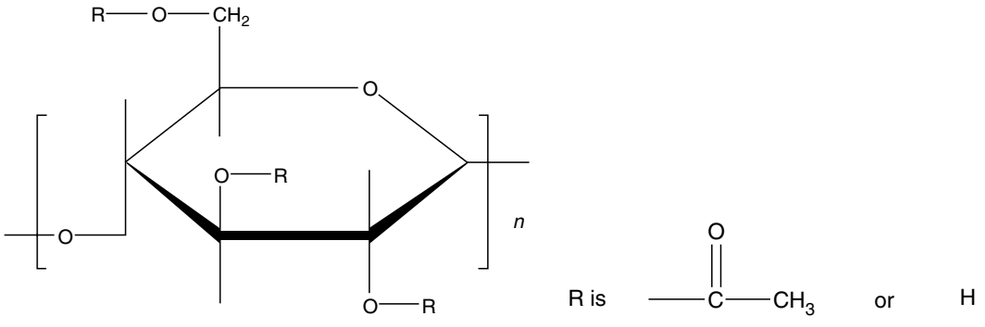

Frequency (cm^{-1})	Assignment
1,050	C–O stretch
1,235	Acetate C–C–O stretch
1,370	CH_3 symmetric (umbrella) deformation
1,432	CH_3 asymmetric deformation
1,750	C=O stretch
2,860	CH_3 symmetric stretch
2,950	CH_3 asymmetric stretch
3,300	OH stretch
3,500	2 × C=O stretch (1,750) overtone

TABLE 22.22. *Nylon 6 [1,22].*

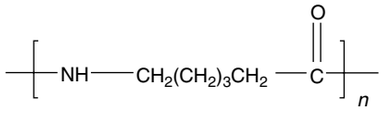

Frequency (cm^{-1})	Assignment
700	NH wag (broad)
722	CH_2 rock
1,170	N–C=O/skeletal vibration
1,200	N–C=O/skeletal vibration
1,370	CH_2 wag

TABLE 22.22. *Continued.*

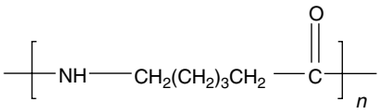

Frequency (cm^{-1})	Assignment
1,420	CH_2 symmetric scissors deformation (CH_2 next to C=O)
1,440	CH_2 symmetric scissors deformation (CH_2 next to N)
1,460	CH_2 symmetric scissors deformation
1,540	NH bend/C–N stretch
1,640	Amide C=O stretch
2,860	CH_2 symmetric stretch
2,920	CH_2 asymmetric stretch
3,100	2 × NH bend (1,540) overtone
3,300	NH stretch

TABLE 22.23. *Polyurethane (polyester based) [1,22].*

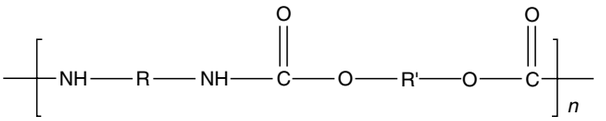

Frequency (cm^{-1})	Assignment
1,060	C–O stretch
1,215	N–C–O stretch
1,460	CH_2 symmetric (scissors) deformation
1,540	C–N stretch
1,590	N–H bend
1,690	C=O stretch (amide)
1,735	C=O stretch (ester)
2,860	CH_2 symmetric stretch
2,925	CH_2 asymmetric stretch
3,320	NH stretch

TABLE 22.24. *Poly(hydroxy butyrate), PHB [1,25].*

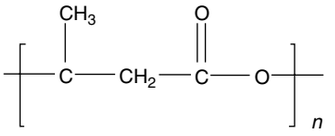

Frequency (cm^{-1})	Assignment
1,050	C–O stretch, ether
1,096	C–O stretch, ether
1,128	C–O stretch, ester
1,180	C–O stretch, ester
1,228	C–O–C stretching mode, crystalline
1,259	C–O–C stretching mode, amorphous
1,263	C–O–C stretching mode, crystalline
1,278	C–O–C stretching mode, crystalline
1,289	C–O–C stretching mode, crystalline
1,302	C–O–C stretching mode, amorphous
1,378	CH_3 symmetric deformation

TABLE 22.24. *Continued.*

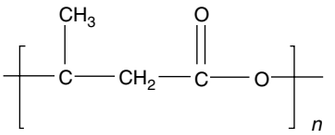

Frequency (cm^{-1})	Assignment
1,449	CH_3 asymmetric deformation
1,458	CH_2 deformation
1,723	C=O stretch, crystalline
1,740	C=O stretch, amorphous
2,875	CH_2,CH_3 symmetric stretch
2,933	CH_2 asymmetric stretch
2,967	CH_3 asymmetric stretch, crystalline
2,974	CH_3 asymmetric stretch, crystalline
2,983	CH_3 asymmetric stretch, amorphous
2,995	CH_3 asymmetric stretch, crystalline
3,009	CH_3 asymmetric stretch, crystalline
3,436	1st overtone, C=O stretch, crystalline

using the information for spectroscopic studies of known polymers. Some assignments are not absolutely conclusive. For analytical identification, entire reference spectra must be used instead. To further guide those who need more in-depth information on this subject, a set of general references is also provided.

REFERENCES

1. N. B. Colthup, L. H. Daly, and S. E. Wiberley, *Introduction to Infrared and Raman Spectroscopy*, 2nd ed. (Academic, New York, 1975).
2. *The Infrared Spectra Atlas of Monomers and Polymers* (Sadtler Res. Labs., Philadelphia, 1980).
3. B. Jasse and J. L. Koenig, J. Makromol. Sci.-Rev. Macromol. Chem. **C17**, 61 (1979).
4. R. G. Snyder and J. H. Schachtschneider, Spectrochim. Acta **20**, 853 (1964).
5. R. S. Stein, J. Chem. Phys. **23**, 734 (1955).
6. J. R. Nielsen and R. F. Holland, J. Mol. Spectrosc. **6**, 394 (1961).
7. G. Zerbi and L. Piseri, J. Chem. Phys. **49**, 3840 (1968).
8. R. G. Snyder and J. H. Schachtschneider, Spectrochim. Acta **21**, 1527 (1965).
9. P. C. Painter, M. M. Coleman, and J. L. Koenig, *The Theory of Vibrational Spectroscopy and Its Applications to Polymeric Materials* (Wiley, New York, 1982).
10. L. J. Bellamy, *The Infra-red Spectra of Complex Molecules*, Vol. 1 (Chapman and Hall, London, 1975).
11. S. Krimm, Fortschr. Hochpolym. Forsch. **2**, 51 (1960).
12. A. Miyake, J. Polym. Sci. **38**, 479 (1959).
13. I. V. Yannas and A. C. Lunn, J. Polym. Sci., Part B **9**, 611 (1971).
14. S. Krimm, L. F. Folt, J. J. Shipman, and A. R. Berens, J. Polym. Sci., Part A **1**, 2621 (1963).
15. Y. Shindo, B. E. Read, and R. S. Stein, Makromol. Chem. **118**, 272 (1968).
16. I. Lipschitz, Polym. Plast. Technol. Eng. **19**, 53 (1982).
17. C. Y. Liang and S. Krimm, J. Polym. Sci. **27**, 241 (1958).
18. M. M. Satkowski, J. T. Grothaus, S. D. Smith, A. Ashraf, C. Marcott, A. E. Dowrey, and I. Noda, in *Polymer Solutions, Blends, and Interfaces*, edited by I. Noda and D. N. Rubingh, (Elsevier, New York, 1992), p. 89.
19. R. Gotoh, T. Takenaka, and N. Hayama, Kolloid Z. **205**, 18 (1965).
20. C. Y. Liang, in *Newer Methods of Polymer Characterization*, edited by B. Ke (Wiley, New York, 1964).
21. H. Matsuura and K. Fukuhara, J. Polym. Sci., Part B: Polym. Phys. **24**, 1383 (1986).
22. C. J. Pouchert, *The Aldrich Library of FT-IR Spectra* (Aldrich Chemical, Mikwaukee, 1985).
23. T. Usami and S. Takayama, Polym. J. **16**(10), 733 (1984)
24. *The Infrared Spectra Atlas of Monomers and Polymers* (Sadtler Res. Labs., Philadelphia, 1980).
25. H. Sato, R. Murakami, A. Padermshoke, F. Hirose, K. Senda, I. Noda and Y. Ozaki, Macromolecules, **37**, 7203 (2004).

GENERAL REFERENCES ON POLYMER IR SPECTROSCOPY

D. I. Bauer and W. F. Maddams, *The Vibrational Spectroscopy of* Polymers (Cambridge University, New York, 1989).

L. J. Bellamy, *The Infra-red Spectra of Complex Molecules*, Vols. 1 and 2 (Chapman and Hall, London, 1975 and 1980).

N. B. Colthup, L. H. Daly, and S. E. Wiberley, *Introduction to Infrared and Raman Spectroscopy*, 2nd ed. (Academic, New York, 1975).

A. Elliot, *Infrared Spectra and Structure of Organic Long-Chain Polymers* (Arnold, London, 1969).

D. O. Hummel, Ed., *Polymer Spectroscopy* (Verlag Chemie, Weinheim, 1974).

J. L. Koenig, *Chemical Microstructure of Polymer Chains* (Wiley, New York, 1980).

J. L. Koenig, *Spectroscopy of Polymers* (ACS, Washington, 1992).

P. C. Painter, M. M. Coleman and J. L. Koenig, *The Theory of Vibrational Spectroscopy and Its Applications to Polymeric Materials* (Wiley, New York, 1982).

CHAPTER 23

Small Angle Neutron and X-Ray Scattering

George D. Wignall

Neutron Scattering Sciences Division, Oak Ridge National Laboratory, Oak Ridge, Tennessee TN 37831-6393

23.1 INTRODUCTION

Scattering in the context of this article means the deflection of a beam of radiation (neutrons/x-rays/light, etc.) from its original direction by interaction with the nuclei or electrons of polymer/solvent molecules in a sample. The angular distribution of the intensity reflects the structure of the sample and such techniques have been employed since the beginnings of polymer science to provide information on the spatial arrangements of macromolecules [1]. The first measurements were made in the 1920s using x-rays to determine crystal structures via the Bragg law

$$n\lambda = 2D \sin\theta, \tag{23.1}$$

where D is the distance between crystallographic planes, λ is the wavelength of the radiation used, 2θ is the angle of scatter, and n is the (integer) order of reflection. The intensity is conventionally measured as a function of the momentum transfer, Q, which is related to 2θ via

$$Q = 4\pi\lambda^{-1} \sin\theta \tag{23.2}$$

although several different symbols have been used to denote this parameter in the literature for the different types of radiation used (e.g., Q, K, h, k, s, q, μ etc.). Combining Eqs. (23.1) and (23.2) gives

$$D = 2\pi/Q \tag{23.3}$$

which indicates the distance scale probed by a measurement at a given value of Q. Experiments in the range $0.6 < Q < 15$ Å^{-1} contain most of the information relevant for the determination of unit cell dimensions and are conventionally referred to as wide-angle scattering, which probe a distance scale $\sim 0.4 < D < 10$ Å. Wide-angle x-ray scattering (WAXS), with a wavelength ~ 1 Å, has been the principal technique for the determination of polymer crystal structures [2]. Unit cell dimensions [3], along with details of the WAXS technique [4] are given in standard reference works [2–4]. Subsequently, neutron diffraction or wide-angle neutron scattering (WANS) has supplemented these measurements of crystal structures [5,6].

In the amorphous state, the intermolecular correlations are more diffuse, and the information available from wide-angle scattering is less precise. A Fourier transform of the data gives a radial distribution function (RDF) which is a weighted sum of interatomic pair correlation functions $g_{ij}(r)$, which express the probability of finding atomic species i and j separated by a distance r. In the crystalline regions of polymers the $g_{ij}(r)$ reduce to a series of delta-functions defining the interatomic distances in the unit cell. For amorphous materials, the RDFs are generally featureless for $r > 10$ Å, indicating the absence of long range order between neighboring chains [7].

Although Bragg's law does not apply to amorphous materials, the Fourier or inverse relationship between the structure in real-space (r) and the scattering in Q-space, means that Eq. (23.3) may be applied to first order for all types of scattering. Thus, data at lower Q-values probe longer length scales, and x-ray methods have been widely used to determine chain dimensions in dilute solution, lamellar spacings in crystalline polymers, etc. These measurements are conventionally referred to as small-angle x-ray scattering (SAXS), though it is the Q-range (typically $10^{-3} < \mathrm{Q} < 10^{-1}$ Å^{-1}) which determines the size of objects studied and radiation with other wavelengths (e.g., light, neutrons) can

provide similar information in different angular ranges. For example, light scattering (LS), with $\lambda \sim 2$–6,000 Å, probes a much smaller Q-range ($\sim 2 \times 10^{-6} < Q < 2 \times 10^{-3}$ Å^{-1}) than SAXS, even though the angular range can be quite large (up to $2\theta \sim 160°$). Hence, the measurements probe distance scales, via Eq. (23.3), up to $\sim 10\,\mu$m and the technique has been used extensively since the 1940s, to determine the molecular weight and global dimensions of polymer molecules, for example in dilute solution.

For over two decades, small-angle neutron scattering (SANS), with a wavelength $\lambda \sim 5$–20 Å, has proven to be extremely useful for the evaluation of polymer chain conformation. Due to a combination of high bulk penetrating power, the ability to manipulate scattering amplitudes through isotopic labeling (e.g., deuteration), or an appropriate choice of solvent (contrast variation), SANS has developed into a powerful tool for the study of polymers, particularly in systems inaccessible to SAXS or LS (e.g., bulk polymers, concentrated solutions etc.).

For most applications in polymer science, neutron, x-ray, and light scattering are examples of predominantly elastic scattering, where the incident and scattered radiation have the same energy or wavelength. Such experiments give information on the time-averaged structure and conformation of polymer molecules and form the bulk of the work undertaken on polymers. There has been less work involving inelastic processes, where there is a change of energy on scattering, and the incident and scattered radiation have different wavelengths. This technique gives valuable information on polymer dynamics, though this methodology is beyond the scope of this article [8–10]. Also, due to space limitations, is not possible to survey all contributions to the understanding of polymer structure by all types of radiation (neutrons, x-rays, light, electrons etc.) in different Q-ranges (small-angle, wide-angle, etc.). Similarly, it is not possible to derive the scattering theory, which will be quoted from existing reviews of neutron [8,11–13], x-ray [14,15], and light scattering techniques [12,16]. Most of the work on polymers has been undertaken at small Q-values to probe the longer length scales associated with these materials. The article will illustrate the type of information provided by SANS and SAXS, along with analogies and differences between neutron and photon scattering.

The treatment will emphasize the importance of placing data on an absolute scale, typically in the form of a differential scattering cross section $d\Sigma/d\Omega(Q)$, per unit sample volume (in units of cm^{-1}) for SAXS and SANS. The equivalent quantity for LS is the Rayleigh ratio, which is directly analogous to $d\Sigma/d\Omega$ [8,17,18]. The use of absolute units is not essential for the measurement of spatial dimensions (e.g., the determination of the radius of gyration of polymer molecules). However, it forms a valuable diagnostic tool for the detection of artifacts, to which scattering techniques are particularly vulnerable.

Because the cross-section varies as the sixth power of the dimensions [14], it is a very sensitive indicator of whether an appropriate structural model has been chosen. Thus, absolute SANS measurements of melt-crystallized blends of normal (hydrogenous) and deuterium-labeled polyethylenes showed that the scattering could exceed the expected intensity for randomly mixed molecules by three orders of magnitude. This indicated that some kind of previously unsuspected aggregation or clustering phenomenon was taking place [19]. Similarly, scattering studies of colloidal micellar solutions may be modeled by calculation of the interparticle correlations between spherical micelles as a function of a set of parameters describing the particle structure (inner/outer radius, degree of ionization etc.). On an arbitrary intensity scale, it is possible to produce excellent fits of the particle shape, which may be in error by as much as 3–4 orders of magnitude in intensity [20]. Thus, absolute calibration allows such artifacts to be recognized, and the model parameters may be restricted to those which reproduce the observed cross section. Because the literature often contains general formulae, as opposed to practical examples of how such calculations are actually accomplished, this article will illustrate such comparisons via a range of examples on different polymeric systems.

Figure 23.1 illustrates the relationship between the neutron energy and wavelength. The kinetic energy of a neutron of particle velocity $\sim 750\,$m/sec (wavelength $\lambda = 5.3$ Å) is $\sim 3\,$meV or 4.7×10^{-15} ergs [8]. Such energies are of the same order as the vibrational and diffusional energies of molecular systems and much lower than x-ray photons ($\sim 10\,$keV). For LS, the scattering patterns are very dependent on the polarization directions, though because of the much higher energies of x-rays, chemical bonding has little effect on SAXS and there is negligible influence of the differences between the directions of radiation polarization and molecular orientation [21]. Hence polarization effects,

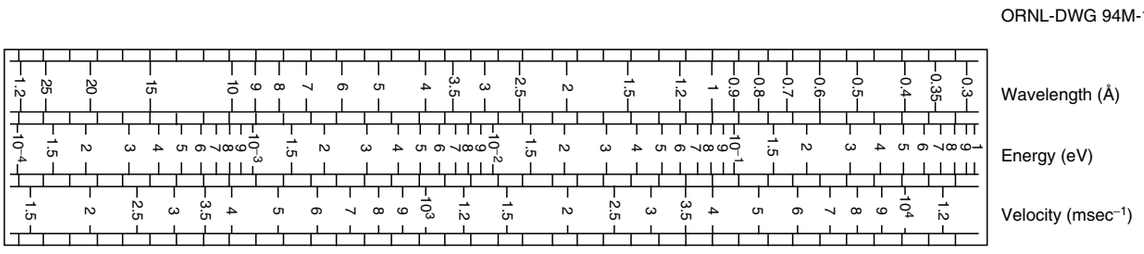

FIGURE 23.1. Conversion chart for neutron wavelength, energy, and velocity.

which are important for LS, can be neglected in SAXS and also for SANS experiments on polymers[1].

SANS, SAXS, and LS all involve interference phenomena between the wavelets scattered by different elements in the system. When a plane wave, described by a wave function of unit density [8] interacts with a single nucleus, the scattered wave is given by

$$\Psi_1 = -\frac{b}{r}\exp(ikr). \tag{23.4}$$

The quantity b has the dimensions of length and is called the scattering length, which may be regarded as a real (known) constant for a given nucleus (isotope). The scattered single atom cross section is given [8,22,23] by

$$\sigma = 4\pi b^2. \tag{23.5}$$

It can be seen from Eq. (23.5) that σ has the dimensions of area. The magnitude of b is typically of the order of 10^{-12}cm, and this gives rise to the usual unit for a cross section which is called a barn (10^{-24}cm^2).

Neutrons are scattered isotropically from individual nuclei, whereas for LS and SAXS, the scattering originates in the electron cloud, so the atomic form factors are in principle Q-dependent. However, the variation is very small in practice ($< 1\%$ for $Q < 0.1$ Å^{-1}) for SAXS and LS, and is usually neglected [4]. The Thompson scattering amplitude of a classical electron is $r_T = 0.282 \times 10^{-12}$cm [24], so the x-ray scattering length of an atom, f, is proportional to the atomic number ($f = r_T Z$) and increases with the number of electrons per atom. For neutrons, there is no general trend throughout the periodic table in the values of b, which vary from isotope to isotope. If the nucleus has nonzero spin, it can interact with the neutron spin, and the total cross section (σ_{coh}) splits into coherent and incoherent components defined by

$$\sigma_{coh} = 4\pi < b >^2 , \tag{23.6}$$

$$\sigma_{inc} = \sigma_{tot} - \sigma_{coh} = 4\pi[< b^2 > - < b >^2], \tag{23.7}$$

where the brackets $<>$ represent a thermal average over the spin state population.

If the isotope has no spin, then $< b^2 > = < b >^2$ as $< b > = b$ and there is no incoherent scattering for neutrons. Only coherent scattering contains information on the structure of the sample. The incoherent cross section contains no information on interference effects and forms an isotropic (flat) background which must be subtracted off in SANS structural investigations. While most of the atoms encountered in neutron scattering from polymers are mainly coherent scatterers (e.g., carbon, oxygen, deuterium), there is one important exception [8,22,23]. In the case of hydrogen (H^1)

$$\sigma_{coh} = 1.76 \times 10^{-24}\text{cm}^2, \tag{23.8}$$

$$\sigma_{inc} = 79.7 \times 10^{-24}\text{cm}^2. \tag{23.9}$$

For photons, there is no strict analog of incoherent scattering of neutrons due to nonzero spin in the scattering nucleus. Compton scattering which occurs for x-rays is similar in that it contains no information on interference effects, i.e., the structure of the sample, and forms a background to the coherent signal. However, to a good first approximation this background goes to zero in the limit $Q \to 0$ and is usually neglected in SAXS and LS studies.

Table 23.1 gives the cross sections and scattering lengths for atoms commonly encountered in synthetic and natural polymers. These cross sections refer to bound protons and neglect inelastic effects arising from interchange of energy with the neutron. For coherent scattering which is a collective effect arising from the interference of scattered waves over a large correlation volume, this approximation is reasonable [8]. However, for incoherent scattering, inelastic effects become increasingly important for long wavelength neutrons with the result that the H^1 incoherent cross section, and hence the sample transmission, is a function of both the

TABLE 23.1. *Bound atom scattering lengths and cross sections for typical elements in synthetic and natural polymers.*

Atom	Nucleus	$b_{coh}(10^{-12}\text{cm})$	$\sigma_{coh} = 4\pi b_{coh}^2(10^{-24}\text{cm}^2)$	$\sigma_{inc}(10^{-24}\text{cm}^2)$	$\sigma_{abs}(10^{-24}\text{cm}^2)$	$f_{x\text{-ray}}(10^{-12}\text{cm})$
Hydrogen	^{1}H	−0.374	1.76	79.7	0.33**	0.28
Deuterium	^{2}H(D)	0.667	5.59	2.01	0	0.28
Carbon	^{12}C	0.665	5.56	0	0	1.69
Nitrogen	^{14}N	0.930	11.1	0	1.88**	1.97
Oxygen	^{16}O	0.580	4.23	0	0	2.25
Fluorine	^{19}F	0.556	4.03	0	0	2.53
Silicon	^{28}Si	0.415	2.16	0	0.17**	3.94
Chlorine	Cl*	0.958	11.53	5. 9	33.6**	4.74

*Values are for the naturally occuring element and are an average over the mixture of isotopes; $f_{x\text{-ray}}$ is given for $\Theta = 0$, though the angular dependence is small (<1%) for $Q < 0.1$ Å^{-1}.

**Values of the absorption cross section (σ_{abs}) are a function of wavelength (λ) and are given at $\lambda = 1.8$Å. As $\sigma_{abs} \sim \lambda$, values at other wavelengths may be estimated by scaling via the ratio $\lambda/1.8$.

[1] Except in the hypothetical case of a material containing elements with unpaired spins (e.g., Fe, Mn, rare earths etc.), where polarization effects can theoretically occur, due to the interaction with the neutron spin. In practice, polymers do not contain such elements, so polarization effects can also be neglected in SANS.

incident neutron energy and sample temperature [25]. In addition, because of inelastic effects due to torsion, rotation, and vibration, the effective incoherent cross section is a function of the particular chemical group (methyl, hydroxyl etc.) in which the proton is situated [26]. This is illustrated in Table 23.2, which shows the total hydrogen atom cross section (σ_{tot}) in various liquids and polymers. σ_{tot} is dominated by the incoherent component (σ_{inc}), and hence is also a strong function of λ and only approaches ~ 80 barns at $\lambda \sim 4.5$ Å. Thus, the cross sections given in Table 23.1 cannot be used to calculate the incoherent background because although $\sigma_{inc} = 79.7 \times 10^{-24}\text{cm}^2$ is widely quoted in the literature, this value almost never applies to real polymer systems.

It may be seen from Table 23.1 that there is a large difference in the coherent scattering length between deuterium and hydrogen and that the latter value is actually negative. This arises from a change of phase of the scattered wave and results in a marked difference in scattering power (contrast) between molecules synthesized with deuterated or protonated monomer units.

The majority of neutron scattering experiments undertaken on polymers fall into the category of SANS from a fraction of deuterated chains in a matrix of normal (protonated) polymer and such experiments are examples of predominantly coherent elastic scattering, which gives information on the time-averaged structure (e.g., chain configuration or orientation in the bulk, polymer compatibility, segregation etc.). Similarly, for x-ray scattering, the energy changes are much less than the incident energy, so SAXS and WAXS are effectively elastic processes, which give complementary information (e.g., lamellar spacings, chain configuration in solution, crystal structures etc.).

As LS probes longer length scales, the most commonly observed pattern for unoriented samples is due to spherulites, which may be interpreted in terms of the scattering of anisotropic spheres to investigate the spherulite size as a function of the crystallization conditions [21]. For liquids, it is well known that LS is particularly sensitive to contaminants (dirt, dust etc.), and that samples must be carefully filtered. This has meant that LS methods have been largely restricted to dilute solutions, though SANS is much less sensitive to this artifact. Accordingly, SANS has been the preferred technique to investigate concentrated solutions [27,28] and bulk polymers [8,13,21,29].

For such experiments, we can define a coherent scattering length of the repeat monomer unit (segment) by

$$a_H = \Sigma_k b_k, \tag{23.10}$$

where the summation runs over all the atoms in an unlabeled monomer unit and a similar equation may be written for the coherent scattering length of a labeled monomer unit a_D. If the two polymers, with polymerization index (N) and segment (monomer) volume (V) are blended together so that the volume fraction of H- and D-labeled components are φ_H and φ_D, respectively, the coherent cross section is given [8] by

$$\frac{d\Sigma}{d\Omega}(Q) = V^{-1} N \varphi_H \varphi_D (a_H - a_D)^2 P(Q) \tag{23.11}$$

after subtracting off the incoherent signal (principally due to H^1 atoms) and the coherent background due to heterogeneities (voids, catalyst residues) or density fluctuations (crystal–

TABLE 23.2. *Experimental (total) hydrogen atom cross sections (σ_{tot}) in various liquids and polymers at room temperature.*

Compound	Formula	Cross section per H^1 atom $\sigma_{tot}(10^{-24}\text{cm}^2)$	
		$\lambda = 9.0$ Å	$\lambda = 4.75$ Å
Methanol	CH_3OH	137	
Ethanol	CH_3CH_2OH	124	
Isopropanol	$CH_3CHOHCH_3$	123	
n-Butanol	$CH_3CH_2CH_2CH_2OH$	117	
n-Propanol	$CH_3CH_2CH_2OH$	113	
Ethanediol	$HOCH_2CH_2OH$	108	
Propanetriol	$HOCH_2CHOHCH_2OH$	100	
Polyvinylalcohol	$-(CH_2CHOH)_n-$	97	
Polymethylmethacrylate	$-(CH(CH_3)-CH_2)_n-$ (CO$_2$CH$_3$ side group)	115	92[a]
Polyethylene	$-(CH_2CH_2)_n-$	113	89[b]
Water ($T = 23$ °C)	H_2O	114	89[c]

Values of σ at $\lambda = 9.0$ Å are taken[2] from reference [26].
[a]Reference [68].
[b]Reference [69].
[c]Reference [66].

[2] By permission of Butterworth-Heinemann Ltd.©

amorphous boundaries, thermal vibrations). The coherent scattering is governed by the single chain form factor, $P(Q)$, which originates from monomer pairs belonging to the same chain [$P(0) = 1$].$d\Sigma/d\Omega(Q)$ is directly analogous to the Rayleigh ratio, used in light scattering [18] and contains information on the single chain (intramolecular) scattering function, $P(Q)$. The mole fraction of each component modulates the coherent cross section and $P(Q)$ may be obtained from the measured intensity at labeling levels up to 50%, though this result was not appreciated in the earliest SANS studies of bulk polymers and concentrated solutions. These experiments relied on analogies with LS where the limit of zero concentration was required to eliminate interchain interference. It may be seen that for $\varphi_D \ll 1$, $\varphi_H \sim 1$ and the cross section is proportional to the concentration [14,32], as assumed in the Guinier [14] and Zimm [30] approximations.

23.2 CONTRAST

The quantity $(a_D - a_H)^2$ is related to the difference in scattering power between labeled and unlabeled chains and is called the contrast factor. In general, radiation incident on a medium whose scattering power is independent of position is scattered only into the forward direction ($\theta = 0$), and all scattering cancels unless the scattering power fluctuates from point-to-point in the sample. X-rays and light photons interact with electrons in the sample and hence are scattered by fluctuations in the electron density (ρ_e). Neutrons on the other hand, have no interaction with electrons, so the contrast arises from fluctuations in scattering length density (ρ_n). Because each nucleus has a different scattering amplitude (Table 23.1), the scattering length density (SLD) is defined as the sum of coherent scattering lengths over all atoms lying in a given volume ΔV, divided by ΔV [31]. For example, in bulk polymers, the SLD is given by the coherent neutron scattering length [Eq. (23.10)] divided by the monomer volume. The coherent cross sections of a system of uniform scattering length density is zero, though fluctuations may be introduced by means of isotopic substitution, thus giving rise to a finite cross section which is proportional to $(a_H - a_D)^2$. Table (23.3) shows values of the SLDs of some H- and D-labeled polymers and solvents.

The parameter used to describe the overall size of a polymer chain is the radius of gyration (R_g), the root mean square distance of all scattering elements from the center of gravity

$$R_g^2 = \frac{\Sigma f_k \, r_k^2}{\Sigma f_k}. \tag{23.12}$$

The summation runs over all scattering elements (k), which are the electrons in the case of SAXS or LS. For SANS, the summation runs over all nuclei, and is weighted by the scattering length of each atom. Thus in principle, the R_g may be different when measured via different techniques. However, in practice each monomer has the same scattering power for a given incident radiation, so for large polymerization indices the differences between SANS, SAXS, and LS radii are negligible. R_g may be derived by expanding $P(Q)$ [Eq. (23.11)] in a power series for low Q ($Q < R_g^{-1}$) and plotting $d\Sigma^{-1}(Q)/d\Omega$ versus Q^2 (30). Alternatively, these parameters may be obtained by plotting ln $[d\Sigma(Q)/d\Omega]$ versus Q^2 at low Q [14]. These types of plots are conventionally referred to as Zimm and Guinier plots, respectively, and the former is generally used for investigating polymer configurations as it has been found to be linear over a wider Q-range. As mentioned earlier, the first measurements in bulk amorphous polymers and concentrated solutions were generally performed in the limit of low relative labeling ($\varphi_D \ll 1$), and extrapolated to zero concentration. In this range, Eq. (23.11) may be expanded to give

$$\frac{d\Sigma^{-1}}{d\Omega}(Q) = \frac{V}{(a_H - a_D)^2 N \varphi_D}\left[1 + \frac{Q^2 R_g^2}{3} + \ldots\right]. \tag{23.13}$$

TABLE 23.3. *Comparison of the scattering length densities of various polymers and solvents.*

Polymer or solvent	Density[3], ρ (at $T \simeq 23$ °C unless otherwise stated) (gm cm^{-3})	Scattering length density, ρ_n (10^{10}cm^{-2})
Carbon disulfide	1.63	1.24
Water	1.0	−0.56
D_2O		6.4
Xylene	0.880	0.79
Xylene-d_{10}		6.04
Toluene	0.867	0.94
Toluene-d_8		5.66
Benzene	0.8765	1.18
Benzene-d_6		5.4
Polybutadiene	0.89	0.41
Polyethylene	0.78 ($T = 145$ °C)	−0.28
Polyethylene-d_4		6.71
Polymethylmethacrylate	1.2	1.06
PMMA-d_8		7.09
Polystyrene	1.05	1.41
Polystyrene-d_8		6.47

23.3 EXAMPLES OF THE APPLICATION OF SANS AND SAXS TO POLYMERS

23.3.1 SANS from Amorphous Polystyrene

Figure (23.2) shows a Zimm plot for 5.0 wt% ($\varphi_D = 0.047$) deuterated polystyrene (PSD) in a matrix of hydrogenous (normal) polymer (PSH). The coherent

[3] The values of SLD are calculated at the indicated densities, which may vary slightly with temperature, tacticity (e.g., for PMMA), degree of crystallinity (e.g., for polyethylene) etc. For different densities, the SLD is proportional to ρ and may be scaled from the values shown. For deuterated materials, it is assumed that the number of monomers per unit volume is independent of deuteration.

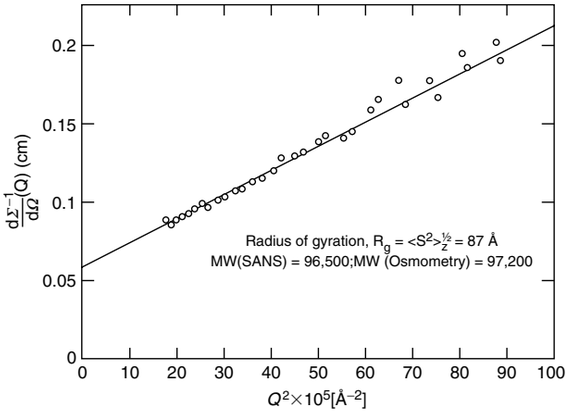

FIGURE 23.2. $\frac{d\Sigma^{-1}}{d\Omega}(Q)$ VS Q^2 for sample containing 5 wt % labeled PSD molecules in polystyrene (PSH).

scattering lengths of the labeled (C_8D_8) and unlabeled (C_8H_8) are 2.328×10^{-12}cm and 10.66×10^{-12}cm, respectively, [via Eq. (23.10) and Table 23.1]. Given a density, $\rho \simeq 1.05$ gm cm^{-3}, the segment volume is 164.5×10^{-24}cm^3 and the extrapolated cross section [$d\Sigma/d\Omega(0) = 17.4 \pm 0.5\,\text{cm}^{-1}$], leads to a polymerization index of the labeled chains of $N_D = 928 \pm 30$ or a molecular weight of $(96.5 \pm 3) \times 10^3$, in reasonable agreement with independent determinations via osmometry [32]. The radius of gyration is close to that measured in ideal Θ-solvents [8,21] and this supports the unperturbed Gaussian coil as a good approximation to the molecular configuration in amorphous polymers [8,13,32].

23.3.2 SANS and SAXS from Melt-Crystallized Polyethylene

Figure 23.3 shows a Zimm plot of the SANS differential scattering cross section for 6.0 wt% ($\varphi_D = 0.053$) of deuterated polyethylene (PED) in a matrix of unlabeled PEH after rapidly quenching from the melt. The coherent scattering lengths of C_2H_4 and C_2D_4 are -0.166×10^{-12} and 4.00×10^{-12}cm^{-1}, respectively, [via Eq. (23.10) and Table 23.1], and based on an average density of $\rho \simeq 0.94$ gm cm^{-3}, the segment volume is 49.5×10^{-24}cm^3. Thus the extrapolated

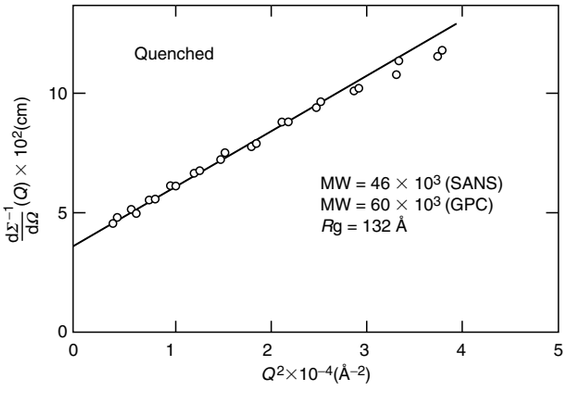

FIGURE 23.3. Typical Zimm plot for 6 WT % PED molecules in PEH matrix quenched from the melt.

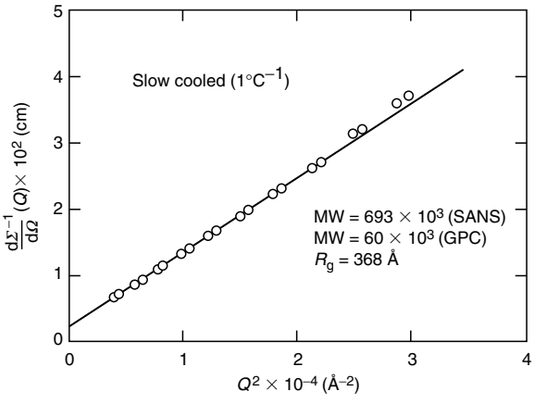

FIGURE 23.4. Typical Zimm plot for 6 wt% PED molecules in PEH matrix slow cooled (1°C^{-1}) from the melt.

cross section [$d\Sigma/d\Omega(0) = 28.0 \pm 2\,\text{cm}^{-1}$] leads to a polymerization index (N) of 1,600, which is of the same order as the value from gel permeation chromatography [33]. However, when the same sample is slow cooled from the melt [Fig. 23.4], the extrapolated cross section increases by over an order of magnitude. It is clear that these data do not originate in the scattering from single molecules, and it has been shown that the excess intensity is caused by aggregation or clustering of the labeled molecules [19], though this would not be apparent if the data were in arbitrary units. This behavior illustrates the point referred to above that the intensity is extremely sensitive to the particle or molecular dimensions and even an approximate ($\pm 25\%$) absolute calibration is sufficient to reveal the presence of such artifacts.

Figure 23.5 shows SAXS data from the polyethylene sample described above. Because PED and PEH have the same electron density, there is no contrast between the different isotopes and PEH, PED and partially labeled

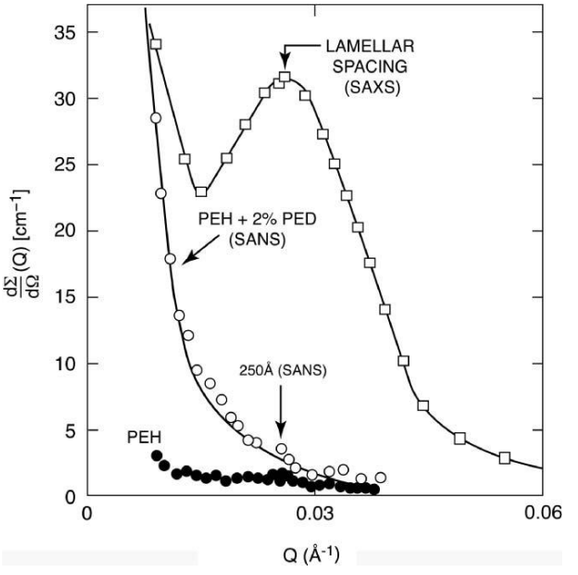

FIGURE 23.5. $\frac{d\Sigma}{d\Omega}(Q)$ vs Q for SAXS and SANS data from melt crystallized polyethylenes.

samples all have the same SAXS profile. The background due to Compton scattering is virtually zero in this Q-range [4] and the signal arises from density fluctuations [13]. The interlamellar peak at $Q \sim 0.025\,\text{Å}^{-1}$ is proportional to the square of electron density difference between the amorphous and crystalline regions (lamellae). The upturn as $Q \to 0$ probably arises from voids and other large scale structures such as spherulites. Figure 23.5 also shows the SANS data for PEH (solid circles), where the coherent signal is superimposed on a flat (incoherent) background $\sim 1\,\text{cm}^{-1}$. The open circles show the extra (coherent) cross section produced by adding 2% deuterated molecules (PED), which is proportional to the contrast difference $(a_H - a_D)^2$ between deuterated and protonated segments.

Departures from the flat incoherent background of the PEH sample (solid circles) are caused by density fluctuations in the sample and it is just possible to see the peak at $Q \sim 0.025\,\text{Å}-1$, due to the periodic stacking of crystalline lamellae alternating with amorphous regions. The SANS coherent signal in PEH is very weak, however, due to the cancellation between the scattering lengths of carbon and hydrogen (Table 23.1), which makes the SLD very small for PEH (Table 23.3).

In the case of PED, there is no cancellation between the coherent scattering lengths of carbon and deuterium (Table 23.1), and the incoherent background is very much smaller than for PEH. Thus, PED should have virtually identical SAXS and SANS cross sections apart from a scale factor. Figure 23.6 shows absolute SAXS and SANS data for the same sample of PED, which should scale as the ratio of the electron density to the scattering length density. As the number of segments per unit volume is the same for SAXS and SANS, this term cancels and the ratio (R) reduces to

$$R = \frac{(0.282 \times 10^{-12} \times 16)^2}{(4.00 \times 10^{-12})^2} = 1.27, \tag{23.14}$$

where $r_T = 0.282 \times 10^{-12}$cm is the Thompson scattering factor of one electron, and 4.00×10^{-12}cm is the neutron scattering length of a C_2D_4 monomer, which contains 16 electrons. Thus the measured (1.31 ± 0.1) and theoretical ratios are in good agreement [34].

23.3.3 Application of Contrast Variation Methods to Core–Shell Latex Structures

Contrast variation methods can sometimes be used to remove a component of the scattering by matching its scattering power with that of the medium in which it is dispersed. This principle can be used in SANS experiments via isotopic solvent mixtures (e.g. H_2O/D_2O) to adjust the scattering power of the medium, as for example in studies of polymer latexes. Grancio and Williams [35] postulated a polymer-rich spherical core surrounded by a monomer-rich shell which serves as the major locus of polymerization, thus giving rise to core–shell morphology. Thus, the first formed polymer constitutes the core and the second formed polymer makes up the shell, and neutron scattering has been used to test this hypothesis by isotopically labeling chains generated at specific points in the polymerization process [36–40].

For a homogeneous particle, suspended in a solvent, the neutron scattering cross section is given by

$$\frac{d\Sigma}{d\Omega}(Q) = (\rho_{np} - \rho_{ns})^2 N_p V_p^2 P(Q), \tag{23.15}$$

where ρ_{np} and ρ_{ns} are the neutron scattering length densities of the particle and solvent, respectively, N_p is the number of particles per unit volume, V_p is the particle volume, and $P(Q)$ is the particle form factor [$P(0) = 1$]. According to Grancio and Williams [35], polymerization takes place in a surface shell and thus if the monomer feed is changed from protonated to deuterated material, this will result in a predominantly D-labeled shell. When examined by SANS in an H_2O–D_2O mixture which matches the scattering length density of the protonated core, the scattering will arise from a hollow sphere with a particle form factor [41] given by

$$P(Q) = 9\frac{[\sin(QR) - \sin(QR1) - QR\cos(QR) + QR1\cos(QR1)]^2}{Q^6R^6(1-l)^6}, \tag{23.16}$$

where R and a are the outer and inner radii, respectively, $(l = a/R)$.

Figure 23.7 shows SANS data from a 4.6 vol% latexes with a fully deuterated PMMA-D shell, (thickness 30 Å) polymerized on a PMMA-H core (radius, $a = 498$ Å), after desmearing corrections for the finite instrumental resolution [37,42]. The absolute intensity at zero scattering angle is given by Eq. (23.15) with $P(0) = 1$ and Vp equal to the volume of the D-labeled polymer in the shell with SLD[4], $\rho_{np} = 6.97 \times 10^{10}\text{cm}^{-2}$. The SLD of the solvent is close to that of the PMMA-H core ($\rho_{ns} = 1.06 \times 10^{10}\text{cm}^2$) and thus

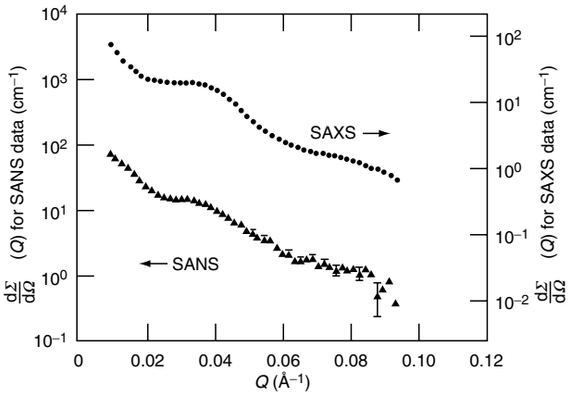

FIGURE 23.6. $\frac{d\Sigma}{d\Omega}(Q)$ vs Q for deuterated polyethylene sample after subtraction of incoherent background.

[4] This value is slightly different to that quoted in Table 23.3, based on a density of 1.2 gm cm^{-3}, which is an average over the atactic, isotactic and syndiotactic homopolymers. For atactic PMMA, $\rho \simeq 1.18$ gm cm^{-3}.

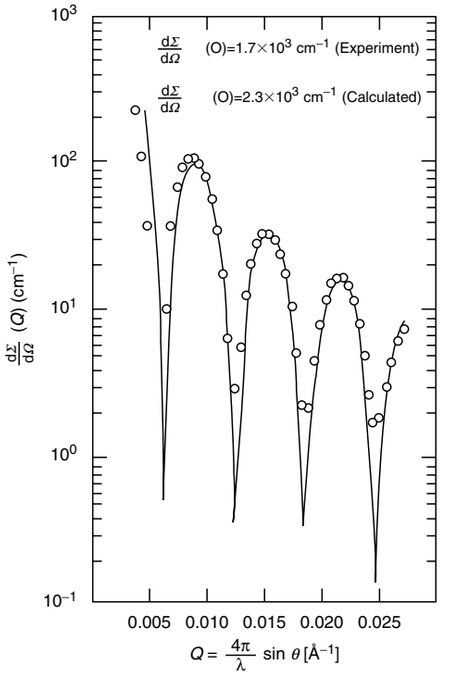

FIGURE 23.7. Desmeared SANS data (O) for PMMA Latex CI (4.6 vol%) with 30 Å D-DMMA shell on surface (core contrast matched) compared with theoretical hollow shell scattering. Reprinted from the Journal of Colloid and Interface Science, **123**, L. W. Fisher, S. Melpolder, J. M. O'reilly, V. Ramakrishnan, and G. D. Wignall, "Neutron Scattering from Interfacially polymerized Latexes", 29–33, Copyright (1988) with permission of Elsevier.

the core contrast is negligible compared to the PMMA-D shell. The extrapolated cross section, $d\Sigma/d\Omega(0) = 1.7 \times 10^3 cm^{-1}$, is in good agreement with the calculated value of $(2.3 \times 10^3 cm^{-1})$, in view of the extreme sensitivity of the calculations to slight variations in shell thickness, mismatches in SLD, surface roughness etc. [37,42]. Similarly the particle dimensions from SANS are in excellent agreement with independent techniques (e.g., LS).

23.3.4 SAXS and SANS from 2-Phase Systems

Blends of High- and Low-Density Polyethylenes

SANS experiments have indicated that blends of high density (linear) and long-chain branched low density polyethylenes (HDPE/LDPE) are homogeneous in the melt, though the components may separate on slow cooling due to the difference in crystallization mechanisms [43]. The semicrystalline blends form effectively two-phase systems in the solid state, and it was shown [43, 44] that the Debye–Bueche (DB) [45,46] model was appropriate to describe the morphology, with a SANS cross section of the form

$$\frac{d\Sigma}{d\Omega}(Q) = \frac{8\pi a^3 \varphi_1 \varphi_2 [\rho_{n1} - \rho_{n2}]^2}{(1 + Q^2 a_1^2)^2}, \qquad (23.17)$$

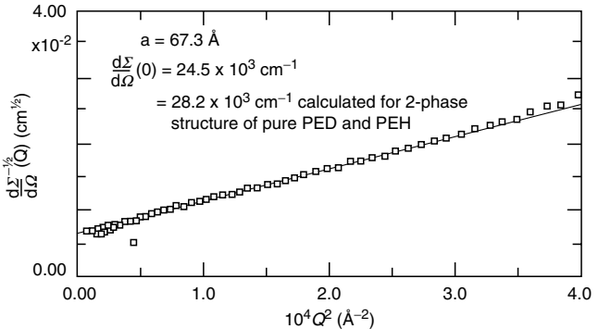

FIGURE 23.8. Debye–Bueche plot for phase separated blend of deuterated HDPE and protonated LDPE slow cooled from the melt AT 0.75 °C^{-1}. Reprinted with permission from R. G. Alamo, J. D. Londono, L. Mandelkern, F. C. Stehling and G. D. Wignall, Macromolecules, **27**, 411 (1994). Copyright (1994) American Chemical Society.

where a_1 is a length characterizing the structure, φ_1 and φ_2 are the volume fractions, and ρ_{n1} and ρ_{n2} are the neutron scattering length densities of the two phases [43,44]. Figure 23.8 shows a DB plot $[d\Sigma/d\Omega(Q)^{-1/2} \text{vs} Q^2]$ of the data for a 50/50 blend after cooling from the melt at 0.75°C min^{-1}. The extrapolated cross section $[d\Sigma/d\Omega(0) = 24.5 \times 10^3 cm^{-1}]$ is well over an order of magnitude higher than in the melt, indicating that the components have phase-separated on cooling. The plot is reasonably linear and the $(Q = 0)$ cross section is given by Eq. (23.17) where the correlation length (a) is derived from the ratio of slope/intercept of the DB plot [44–47]. Assuming complete separation of the H- and D-labeled components, the SLDs in the solid state can be scaled (via the density) from the melt values shown in Table 23.3, to give a calculated cross section of $28.2 \times 10^3 cm^{-1}$. In view of the fact that the experiments are independently calibrated with no arbitrary fitting factors in the intensity scale, the agreement with the absolute cross sections calculated from the DB theory is excellent.

Interpenetrating Polymer Networks

Figure 23.9 shows DB plots of SANS data from polystyrene–polybutadiene interpenetrating polymer networks [47].

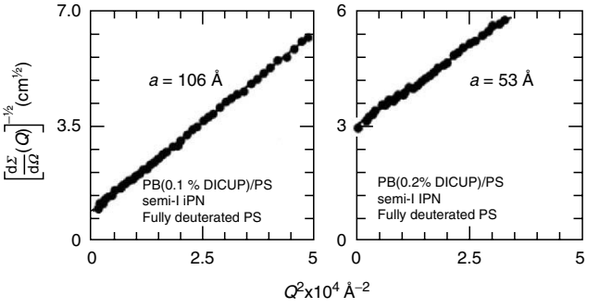

FIGURE 23.9. $\left[\frac{d\Sigma}{d\Omega}(Q)\right]^{-1/2}$ vs. Q^2 for two PB/PS semi-I-IPN systems with different amounts of cross-linker (DICUP).

Assuming complete segregation of the components, $d\Sigma/d\Omega(0)$ may be calculated from Eq. (23.17), via the measured correlation lengths (Fig. 23.9) and the SLDs given in Table 23.3. For the data from the two samples shown in Fig. 23.9, this leads to calculated values of $17.2 \times 10^3 cm^{-1}$ and $2.7 \times 10^3 cm^{-1}$, compared to experimental determinations of $21.6 \times 10^3 cm^{-1}$ and $2.0 \times 10^3 cm^{-1}$. The discrepancies are not unreasonable in view of the strong dependence of the cross section on the domain dimensions, which is a general feature of absolute intensity comparisons. However, this illustrates the point made earlier that even an approximate ($\pm$ 25%) absolute calibration is sufficient to test the assumption of complete phase separation of the blend components.

In the limit $Qa \gg 1$, Eq. (23.17) reduces to $d\Sigma/d\Omega \sim PQ^{-4}$

$$P = 2\Pi(\rho_{n1} - \rho_{n2})^2 S/V, \tag{23.18}$$

where P is the Porod constant, which contains information on the specific surface of the material, i.e., the total interphase surface (S) area per unit volume (V). By comparison of Eqs. (23.17) and (23.18)

$$S/V = 4\varphi_1\varphi_2/a. \tag{23.19}$$

For the data shown in Fig. 23.9, this leads to specific surface values in the range $(58–150) \times 10^4 cm^{-1}$ or $(58–150) m^2 gm^{-1} (\rho \simeq 1.0\, gm\ cm^{-3})$.

Void Content of Hompolymers via SAXS Invariant Analysis

Figure 23.10 shows a Kratky plot [$(Q^2 d\Sigma/d\Omega(Q)$ vs Q] for a polyimide sample made from the condensation of pyromellitic-dianhydride and oxydianiline (PMDA-ODA). The integrated area under this curve is the invariant which for a 2-phase system is given by

$$\mathbf{Q_0} = \int_0^\infty Q^2 d\Sigma/d\Omega(Q) dQ = 2\pi^2 \varphi_1 \varphi_2 r_T^2 [\rho_{e1} - \rho_{e2}]^2, \tag{23.20}$$

where φ_1, φ_2, and ρ_{e1}, ρ_{e2} are the volume fractions and electron densities of the two phases, respectively. PMDA-ODA may be regarded as a 2-phase system consisting of polymer and voids [48], with $\varphi_1 \ll 1$ and $(1 - \varphi_1) \simeq 1$. The polymer has a density of $1.4\, gm\ cm^{-3}$ and the repeat unit (mass 382) contains 196 electrons, so $\rho_{e2} = 0.43 \times 10^{24}$ electrons cm^{-3} and $\rho_{e1} = 0$. From Fig. 23.10 the invariant, $\mathbf{Q_0} = 0.25 \times 10^{-4} cm^{-1} Å^{-3}$, or $0.25 \times 10^{20} cm^{-4}$, giving a void fraction, $\varphi_1 \simeq 8.7 \times 10^{-5}$, which is typical for such materials [48].

An alternative estimate for φ may be obtained via Guinier analysis if the voids are reasonably monodisperse, as indicated in Fig. 23.11. Assuming that the voids are spherical, the radius (R) may be obtained from the measured R_g via $R = (5/3)^{0.5} R_g \simeq 348$ Å. The extrapolated cross section $d\Sigma/d\Omega(0) \simeq 142\, cm^{-1}$ is given by

$$\frac{d\Sigma}{d\Omega}(0) = N_P V^2 r_T^2 \varphi_1 \varphi_2 [\rho_{e1} - \rho_{e2}]^2, \tag{23.21}$$

where $V = 4/3\pi R^3 = 176 \times 10^6$ Å^3 (or $176 \times 10^{-18} cm^3$) is the particle (void) volume and N_p is the number of particles per unit volume. For $\varphi_1 \ll 1$, $N_p V \simeq \varphi_1$ and Eq. (23.21) gives $\varphi_1 \simeq 5.6 \times 10^{-5}$. The two estimates from the invariant and Guinier analysis are of the same order, and the difference probably results from the Guinier assumption of a relatively monodisperse void distribution. Departures from nonlinearity in the Guinier plot observed at the higher Q-values in Fig. 23.11 may reflect polydispersity effects, and thus the estimate via invariant analysis (which is independent of such assumptions) is probably more accurate.

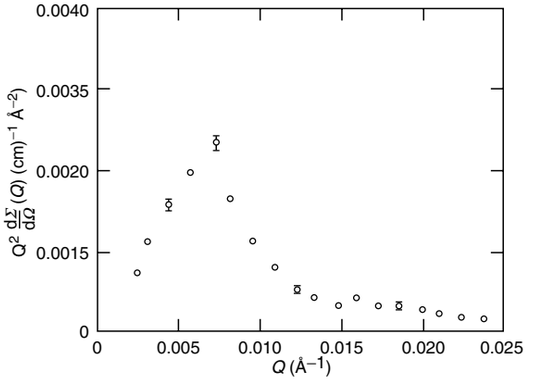

FIGURE 23.10. Integrated scattering curve for PMDA–ODA imidized at 350 °C.

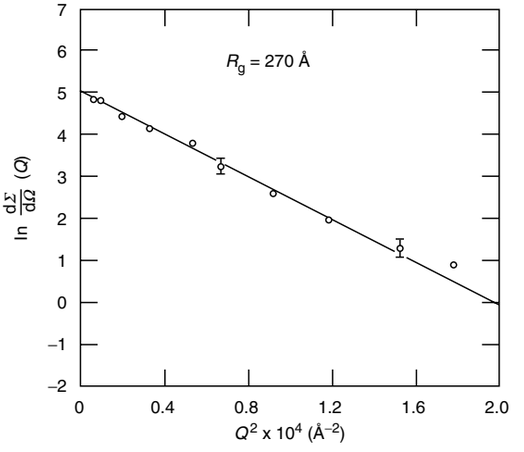

FIGURE 23.11. SAXS Guinier plot for PMDA–ODA Imidized at 350 °C.

23.3.5 Characterization of Multiphase Systems by SANS and SAXS

Blends of High-Density and Linear Low-Density Polyethylenes

Equations (23.17)–(23.20) are strictly valid only for two-phase morphologies, and for multiphase systems, an extension of the SAXS invariant analysis may be employed by generalizing Eq. (23.20) and summing over the number of phases involved

$$\mathbf{Q_0} = 2\pi^2 \sum_{i \neq j} r_T^2 \varphi_i \varphi_j [\rho_{e1} - \rho_{e2}]^2. \tag{23.22}$$

Such an analysis has been applied to semicrystalline blends of polycaprolactone and polycarbonate via SAXS [49] and complementary SANS experiments [50] have employed the DB analysis described above [see Sections ''Blends of High-and Low-Density Polyethylene'' and ''Interpenetrating Polymer Networks'']. For semicrystalline blends of high density and short-chain branched linear low density polyethylenes (LLDPE), complementary DSC and TEM techniques indicate that the compositions of the various crystals and surrounding amorphous regions are such that the system cannot be described by a two-phase model [51]. The ($Q = 0$) cross section [$d\Sigma/d\Omega(0)$] cannot be calculated for multiphase systems, though it may be estimated via a ''pseudo two-phase'' model to a good approximation. For example, with deuterated HDPE-D and protonated LLDPE-H (to provide SANS contrast), the SLD of the HDPE-D crystal is $8.57 \times 10^{10}\text{cm}^{-2}$, whereas the SLDs of the mixed (HDPE-D/LLDPE-H) crystals and amorphous are 0.44 and 0.46 ($\times 10^{10}\text{cm}^{-2}$). Thus, the SANS cross section [$d\Sigma/d\Omega(0)$] can be calculated to a good approximation by grouping the mixed phases into an average background ($\rho_{av} = 0.45 \times 10^{10}\text{cm}^{-2}$) surrounding pure HDPE-D crystal in a pseudo two-phase model. The SANS invariant may be calculated for a multiphase morphology [Eq. (23.22)] by substituting the neutron scattering length densities (ρ_n) for the x-ray scattering length density ($r_T\rho_{e1}$) and summing over the various phases [51]. The ($Q = 0$) cross section may be estimated via Eq. (23.17) for the pseudo two phase model. For series of HDPE-D/LDPE-H samples isothermally crystallized from the met at 117 °C, the experimental data are compared with calculations for two possible morphologies suggested by DSC and TEM analysis:

A. A fraction of the HDPE-D component segregates during isothermal crystallization and the remainder co-crystallizes with LLDPE-H on cooling.

B. HDPE-D partially segregates from the LLDPE-H during isothermal crystallization and the remainder also segregates on cooling. A compositionally mixed homogeneous amorphous phase was assumed to surround the crystals in both cases.

The experimental and calculated Q_0 values are listed in Table 23.4, and for the 18/82 (vol%) blend the calculated Q_0 and the experimental data are identical for morphology type A. Similarly, the value of $d\Sigma/d\Omega(0)$ calculated from the pseudo two-phase model and Eq. (23.1) is $41.4 \times 10^3\text{cm}^{-1}$ for morphology type A, which agrees closely with the experimental value of $39.3 \times 10^3\,\text{cm}^{-1}$. When morphology type B is assumed, the calculated values do not agree with the experimental data for this blend. Thus, SANS supports the idea that predominantly LLDPE-rich blends crystallize isothermally with morphology A, where a fraction of the HDPE-D component segregates during isothermal crystallization and the remainder co-crystallizes with the LLDPE-H on cooling.

For the linear-rich, 78/22 blend the agreement between the experimental and calculated Q_0 and $d\Sigma/d\Omega$ (0) values is closer for morphology type B. SANS indicates that for this blend the intensity and invariant conforms a more segregated morphology of the linear and branched components than for the LLDPE-rich blend. For 50/50 blends, the measured and calculated values of Q_0 and $d\Sigma/d\Omega(0)$ indicate an intermediate between the A and B types, where part of the HDPE component that crystallizes on cooling is co-crystallized with the branched LLDPE and part crystallizes as pure HDPE [51].

In view of the fact that the experiments are independently calibrated with no arbitrary fitting factors in the intensity scale and that the crystal/amorphous compositions are obtained from DSC, the general agreement with the SANS data is excellent. Thus, the two-phase approximation is able to reproduce not only the SANS invariant, but also the ($Q = 0$) cross section with good accuracy.

TABLE 23.4. *Measured and calculated cross sections and invariants for HDPE-D/LDPE-H blends isothermally crystallized at 117 °C.*

Composition (% volume) HDPE-D/LLDPE-H	$d\Sigma/d\Omega(Q=0)$ $\times 10^{-3}(\text{cm}^{-1})$ expt.	Q_0 $\text{cm}^{-1}\text{Å}^{-3}$ expt.	Proposed morphology	$d\Sigma/d\Omega(Q=0)$ $\times 10^{-3}(\text{cm}^{-1})$ calc.	Q_0 $\text{cm}^{-1}\text{Å}^{-3}$ calc.
18/82	41.4	0.009	A	39.2	0.009
			B	58.1	0.013
78/22	36.1	0.0158	A	18.4	0.007
			B	33.1	0.013

Carbon-filled polyethylenes

Other multiphase systems involving polymers include composite materials produced by mixing with filler particles to modify their mechanical properties or conductivity. For example, carbon black has been extensively used as a reinforcing filler in a number of applications such as automotive tires and can also be blended with insulators such as semicrystalline polyethylene (PE) to produce conductive composites used in electrical products. When the concentration of carbon black at room temperature is above the percolation threshold, the composite is conducting. However, at higher current loading, the system heats and expands the polyethylene (PE) matrix, and when this approaches the percolation threshold it becomes highly resistive [52]. This results in a lower current and the device cools to its original state, so a mixture of carbon black and polyethylene acts as a resettable fuse [53].

For materials with particle sizes in the range $\sim$ 10–1,000 Å, both SANS and SAXS may be used to explore the morphology and a combination of these techniques can provide greater insight than either technique in isolation. For example, combined SAXS/SANS studies of carbon-PE composites [52] suggested the presence of a third phase (voids) and subsequent experiments using the contrast options available from deuterium-labeling of the PE-matrix were designed to quantify the void fraction and its variation with temperature [53]. Figure 23.12 illustrates schematically the contrast options available from the combination of SAXS/SANS and deuterium labeling in the study of the three-phase system (polymer, carbon black, and voids), and makes it clear that one cannot resolve void morphology solely with SAXS. However, if one examines a normal composite (with protonated or H-labeled polymer) via SANS, the sample is essentially two-phase because the neutron scattering length densities of polyethylene and voids are virtually identical (see Table 23.5). For such a two-phase system, it has been shown that the morphology may be described by an extension of the DB theory [45,46] and Eq. (23.17) is modified to

$$\frac{d\Sigma}{d\Omega}(Q) = \frac{8\pi a_1^3 \varphi_1 \varphi_2 f[\rho_{n1} - \rho_{n2}]^2}{(1 + Q^2 a_1^2)^2} + \pi^{3/2} a_2^3 \varphi_1 \varphi_2 (1 - f)[\rho_{n1} - \rho_{n2}]^2 \exp\frac{-Q^2 a_2^2}{4}, \tag{23.23}$$

where a_2 is a second correlation length characterizing long range structural features. $(1 - f)$ and f are the fractional contribution of long ranged ($a_2 \sim$ 500–860 Å) and short ranged ($a_1 \sim$ 130–290 Å) components of the structural model, respectively, [46,52,53]. As before, φ_1 and φ_2 are the volume fractions and ρ_{n1} and ρ_{n2} are the neutron scattering length densities of the effectively two-phase system of carbon (SLD $= 6.4 \times 10^{10}$cm^{-2}) and polyethylene/voids (SLD ~ 0); see Table 23.5. Typically f is in the range $0.82 < f < 0.97$ for $0.27 < \varphi < 45.5$ vol% and for $f = 1$, Eq. (23.23) reduces to Eq. (23.17). Thus, a "pseudo two-phase model" may be again applied to this three-phase composite material, as in section "Blends of High-Density and Linear Low-Density Polyethylenes", and it was shown [52] that Eq. (23.23) gives excellent fits to the SANS data over a wide range of carbon black compositions. Table 23.6 compares the measured and calculated cross sections at $(Q = 0)$ and it may be seen that the discrepancies for any given concentration are in the range $\pm$ 25%. Such fluctuations are not unexpected in view of the extreme sensitivity of the cross section to the fitted correlation lengths, both of which are cubed to calculate $d\Sigma/d\Omega(0)$. However, the overall agreement is excellent, as there is no systematic distortion and the deviations are both positive and negative in virtually equal proportions.

If one blends carbon black with deuterated polyethylene, it may be seen from Fig. 23.12, that presence of voids is highlighted within the carbon black/*d*-polyethylene matrix. Through a combination of SAXS/SANS experiments, one can extract information about void size and quantity [53] using the theoretical formalism developed by Wu [54] to model microvoids in composite materials. Typical void concentrations $\sim$ 2 vol%, 400–500 Å in size were measured at room temperature in composite materials containing 30–40 vol% carbon. These voids decrease significantly in concentration during the melt transition however, dropping by an order of magnitude to $\sim$ 0.2 vol%. This decrease might be expected and suggests that the polyethylene domains

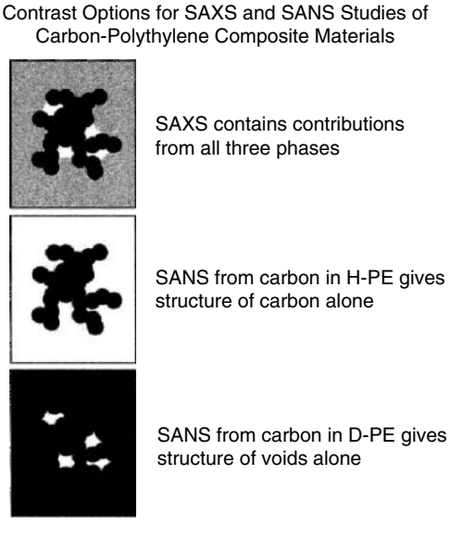

FIGURE 23.12. Contrast options for SAXS and SANS studies of carbon–polyethylene composite materials.

TABLE 23.5. *Neutron (ρ_n) and X-ray ($\rho_x = r_T\rho_{e1}$) scattering length densities of components of carbon-polyethylene composite materials.*

Species	Density, ρ(gm cm^{-3})	X-Ray scattering length density, $\rho_x(10^{10}\text{cm}^{-2})$	Neutron scattering length density, $\rho_n(10^{10}\text{cm}^{-2})$
Carbon black	1.92	16.2	6.4
Voids	0.0	0.0	0.0
Polyethylene	0.95	9.12	−0.34
Polyethylene-d_4	1.08	9.12	8.13

grow at the expense of the voids as the temperature is brought above the melting point.

23.3.6 Isotope Effects in SANS

SANS studies of deuterium labeled polymers were based initially on the assumptions that the molecular configurations and interactions are independent of deuteration, and the interaction parameter between D-labeled and unlabeled segments of the same species χ_{HD} is zero. Nevertheless, there have been several experimental observations which suggested that isotopic substitution does influence polymer thermodynamics and Buckingham and Hentschell [55] suggested that this might arise from a finite interaction parameter ($\chi_{HD} \sim 10^{-4} - 10^{-3}$) between H- and D-labeled segments. Subsequently, SANS was used to measure χ_{HD} for a range of isotopic mixtures [56–58], to delineate the circumstances under which demixing can occur.

For a blend of two polymer species (A and S), one of which (A) is deuterium labeled, the coherent cross section (after subtracting the incoherent background) is given [8,13] by

$$\frac{d\Sigma}{d\Omega}(Q) = V^{-1}(a_H - a_D)^2 S(Q), \tag{23.24}$$

where $S(Q)$ is the structure factor, which contains information regarding both molecular architecture and thermodynamic interactions. In the mean field random phase approximation [59], $S(Q)$ is given by

$$S^{-1}(Q) = [\varphi_A N_A P_A(QR_{gA})]^{-1} + [(1-\varphi_A)N_S P_S(QR_{gS})]^{-1} - 2\chi, \tag{23.25}$$

where $\varphi_A = \varphi_D$ is the volume fraction of the A species and R_{gA}, R_{gS}, N_A and N_S are the radii of gyration and polymerization indices of the two species. The intra-chain functions $P_A(Q)$ and $P_S(Q)$ are represented by Debye functions [60], based on the assumption of a Gaussian distribution of chain elements.

$$P(Q) = 2[R_g^2\, Q^2 + \exp(-R_g^2\, Q^2) - 1]/(R_g^4 Q^4). \tag{23.26}$$

By regarding the H- and D- molecules as different species with volume fractions φ_H and φ_D, the random phase approximation [Eq. (23.19)] may be fitted to the data with χ_{HD} as the only adjustable parameter [56–58]. Complementary experiments on polystyrene [61] and poly (dimethyl siloxane) [62] confirm the existence of a universal isotope effect, arising from the small differences in volume and polarizability between C–H and C–D bonds [63]. Table (23.7) lists typical values of the isotopic interaction parameter for various polymers in the concentration range $0.2 < \varphi_D < 0.8$,

TABLE 23.6. *Comparison of measured and calculated values of the absolute SANS cross section at $Q = 0$ for carbon–polyethylene composite materials.*

Vol % carbon black	$d\Sigma/d\Omega(Q=0)$ $\times 10^{-3}(\text{cm}^{-1})$ measured	$d\Sigma/d\Omega(Q=0)$ $\times 10^{-3}(\text{cm}^{-1})$ calculated
44.5	98	77
39.5	159	118
34.8	177	166
26.3	237	200
16.5	317	380
12.4	247	345
5.6	178	182
1.08	49	50
0.53	32	24
0.27	8	11

TABLE 23.7. *Isotopic interaction parameter for various polymers.*

Polymer	φ_D	T °C	$10^4\chi_{HD}$
Polystyrene	0.5	160	1.8[a] 2.3[b]
1,4 Polybutadiene	0.31	50	7.2[c]
1,2 polybutadiene (polyvinyl ethylene)	0.5	47	6.8[d]
1,2 Polybutene (Polyethyl ethylene)	0.5	47	8.8[d]
Polydimethylsiloxane		∼296	17[e]
Polyethylene	0.5	160	4.0[f]

[a] Reference [56].
[b] Reference [61].
[c] Reference [56].
[d] Reference [58].
[e] Reference [62].
[f] Reference [65].

where χ_{HD} has been shown to be relatively independent of concentration [58,61].

The above results raise the important question of how SANS studies are influenced by isotope effects. As explained earlier, initial SANS experiments on polymers relied on analogies with LS, where the limit of zero concentration was required to eliminate inter-chain scattering. Under such conditions, the isotope effect contributes almost insignificantly to the intensity, and this may be illustrated by calculating $d\Sigma/d\Omega(0)$ via Eqs. (23.24) and (23.25) for the sample of 5.0 wt% PSD in PSH as in Section 23.3.1. The inclusion of an isotopic interaction parameter $\chi_{HD} = 1.8 \times 10^{-4}$ changes $d\Sigma/d\Omega(0)$ to $17.5\,cm^{-1}$ compared to $17.4\,cm^{-1}$ calculated from Eq. (23.11) in the absence of isotope effects. Upon recognizing that information on chain statistics could equally well be obtained from concentrated isotopic mixtures, many experiments were conducted under such conditions in order to enhance the intensity. It is under these conditions that isotope-induced segregation effects are manifested.

In the bulk state many of the systems studied are solids at room temperature and have been exposed for only a limited time in the liquid state, as for example during melt pressing. For polybutadiene, with a glass transition temperature below $-90\,^{\circ}C$, isotopic blends are liquid at room temperature, and this facilitates the attainment of equilibrium. Hence, isotope effects can be particularly dramatic in this system and Fig. (23.13) shows the scattering cross section of mixtures of deuterated ($N_D = 4{,}600$) and protonated ($N_H = 960$) as a function of temperature. It can be seen that the extrapolated zero-Q cross section exceeds by large factors the value it would have ($\sim 100\,cm^{-1}$) if the H–D interactions were negligible. For sufficiently high molecular weight, this system will even phase separate [64], as will other isotopic mixtures (e.g., polyethylene [65]). Thus, it is prudent to evaluate future experiments, based on measured values of χ_{HD} (Table 23.7), and to check for excess scattering. This is best accomplished by calibrating data on an absolute scale and comparing the measured and theoretical intensities [66].

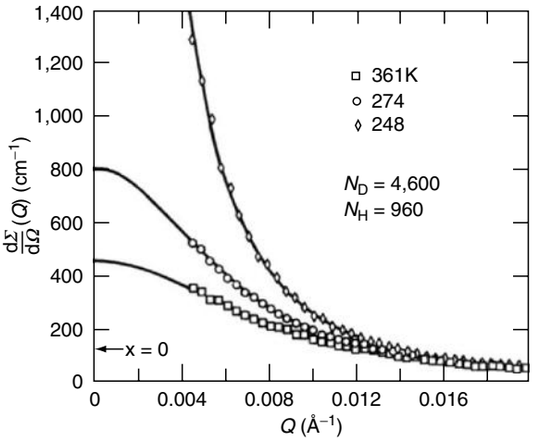

FIGURE 23.13. $\frac{d\Sigma}{d\Omega}(Q)$ VS Q for blend of 69 vol% protonated and 31% deuterated 1, 4-Polybutadiene at the critical composition. The curves were obtained from the homogeneous mixture scattering function by adjusting χ_{HD} (one adjustable parameter). Reprinted with permission from F. S. Bates, G. D. Wignall and W. C. Koehler, Phys Rev. Lett., **55**, 2425 (1985). Copyright (1985) American Physical Society.

Table 23.8 summarizes the formulae for the scattering parameters defined in the above examples. Scattering techniques have been one of the main sources of structural information since the beginnings of polymer science. Over the past two decades, SANS has been extensively applied to complement existing scattering methods (SAXS, WAXS, LS etc.) and the above examples illustrate the new information which it has provided. The complementary aspects of neutron, light, and X-ray scattering, as applied to polymers and colloids, have been surveyed in a current volume edited by Lindner and Zemb [12]. A wide range of applications of neutron scattering to study polymer structure have been described by Higgins and Benoit [29], and Gabrys [67].

TABLE 23.8. *Scattering parameters and formulae.*

Scattering parameter	Particular assumptions of Model[a]	Formula	Equation
Forward ($Q = 0$) cross section, $d\Sigma/d\Omega(0)$	Guinier model (relatively monodisperse particles)	$\frac{d\Sigma}{d\Omega}(0) = N_p V_p^2 (\rho_{n1} - \rho_{n2})^2$ (SANS[b])	(23.15)
Forward ($Q = 0$) cross section, $d\Sigma/d\Omega(0)$	Debye–Bueche model (randomly intermixed phases)	$\frac{d\Sigma}{d\Omega}(0) = 8\pi a^3 \varphi_1 \varphi_2 (\rho_{n1} - \rho_{n2})^2$ (SANS[b])	(23.17)
Invariant, $\mathbf{Q}_0 \int_0^\infty Q^2 d\Sigma/d\Omega(Q) dQ$		$\mathbf{Q}_0 = 2\pi^2 \varphi_1 \varphi_2 r_T^2 [\rho_{e1} - \rho_{e2}]^2$ (SAXS[b])	(23.20)
Porod constant $P = Q^4 d\Sigma/d\Omega(Q)$		$P = 2\pi(\rho_{n1} - \rho_{n2})^2 S/V$ (SANS[b])	(23.18)

[a] The Guinier, Debye–Bueche, Invariant and Porod analyses are all based on the assumption of well defined phases with sharp interfacial boundaries. In addition, the Guinier approach is based on the assumption that the length distribution function (23.15), or probability $P_{00}(r)$ that a randomly placed rod (length, r) can have both ends in the same scattering particle (phase) is zero beyond a well defined limit. For example, for monodisperse spheres, diameter D, $P_{00} = 0$, for $r > D$. In the Debye–Bueche model, P_{00} has no cut off and approaches zero via an exponential correlation function only in the limit $r \to \infty$ [45,46].

[b] For SAXS, the neutron scattering length density (ρ_n) is replaced by the product of the electron density (ρ_e) and the Thompson scattering length ($r_T = 0.282 \times 10^{-12}$ cm), and vice-versa.

ACKNOWLEDGMENTS

The author wishes to thank W. L. Wu and P. A. Egelstaff for permission to include Table 23.2 and Fig. 23.1, respectively. This research was supported by the Division Materials Science, US Department of Energy under contract DE-AC05-00OR22725 with the Oak Ridge National Laboratory, managed by UT-Battelle, LLC.

REFERENCES

1. P. J. Flory, Principles of Polymer Chemistry, Cornell Press, Ithaca, New York p. 22 (1953).
2. L. E. Alexander, X-Ray Diffraction Methods in Polymer Science, Krieger Publishing Co. Inc., London (1969).
3. Chapter IV, Polymer Handbook, ed. J. Brandrup and E. H. Immergut, Wiley Interscience, New York (1975).
4. Chapter 3, International Tables for X-ray Crystallography, ed. C. H. Macgillavry and G. D. Rieck, Kynoch Press, Birmingham (1968).
5. A. Avitabile, R. Napolitano, B. Pirrozzi, K. D. Rouse, M. W. Thomas and B. T. M. Willis, J. Polym. Sci., Polym. Lett. Ed., **13**, 351 (1975).
6. M. Stamm, J. Polym. Sci., Polym. Phys. Ed., **20**, 235 (1982); M. Stamm, E. W. Fischer, M. Dettenmaier, and P. Convert, Discuss. Faraday Soc. **68**, 263 (1979).
7. G. D. Wignall, Chapter 4 in Applied Fiber Science ed. F. W. Happey, Academic Press, London (1978).
8. G. D. Wignall, Encyclopedia of Polymer Science and Engineering, ed. M. Grayson and J. Kroschwitz, Wiley and Sons, New York, 10, 112 (1978).
9. G. Allen and J. S. Higgins, Rep. Prog. Phys. **36**, 1073 (1973).
10. K. Nicholson, Contemp. Phys. **22**, 451 (1981).
11. J. S. Higgins and A. Maconnachie, Chapter 22 in Neutron Scattering, eds. K. Skold and D. L. Price, Academic Press, New York, p. 287 (1987).
12. Neutron, X-Ray and Light Scattering, ed. P. Lindner and T. Zemb, North-Holland Delta Series, Elsevier Publishers, New York, (1991).
13. G. D. Wignall, Chapter 7, p. 313 in The Physical Properties of Polymers, ed. J. E. Mark, ACS Books (1993).
14. A. Guinier and G. Fournèt, Small-Angle Scattering of X-Rays, John Wiley, New York (1955).
15. O. Glatter and O. Kratky, Small-Angle X-Ray Scattering, Academic Press, London (1982).
16. M. G. Huglin, Light Scattering from Polymer Solutions, Academic Press, London (1982).
17. G. Hadziioannou and R. S. Stein, Macromolecules, **17**, 567 (1984); Macromolecules, **17**, 1059 (1984).
18. R. G. Kirste, W. A. Kruse and K. Ibel, Polymer, **16**, 120 (1975).
19. J. Schelten, G. D. Wignall, D. G. H. Ballard and G. W. Longman, Polymer, **18**, 1111 (1977).
20. J. B. Hayter and J. Penfold, Colloid Polym. Sci. **261**, 1022 (1983).
21. J. S. Higgins and R. S. Stein, J. Appl. Cryst. **11**, 346 (1978).
22. V. E. Turchin, Slow Neutrons, Israel Program for Scientific Translations, Jerusalem (1965).
23. G. E. Bacon, Neutron Diffraction, Clarendon Press, Oxford, England (1971).
24. R. W. James, The Optical Principles of the Diffraction of X-rays, Bell, London (1958).
25. A. Maconnachie, Polymer, **25**, 1068 (1984).
26. L. D. Coyne and W. Wu, Polym. Commun. **30**, 312 (1989).
27. J. P. Cotton, B. Farnoux, G. Jannink, J. Mons and C. Picot, C. R. Acad. Sci. (Paris), 275, 3C, 175 (1972).
28. J. S. King, W. Boyer, G. D. Wignall and R. Ullman, Macromolecules, **18**, 709 (1985).
29. J. S. Higgins and H. Benoit, Neutron Scattering from Polymers, Clarendon Press, Oxford (1994).
30. B. H. Zimm, J. Chem. Phys. **16**, 157 (1948).
31. J. B. Hayter in V. Degiorgio and M. Corti, eds. Proceedings of Enrico Fermi School of Physics Course XC, North Holland, Amsterdam (1985), p. 59.
32. G. D. Wignall, D.G.H. Ballard and J. Schelten, Eur. Polym. J., **10**, 861 (1974).
33. J. Schelten, D.G.H. Ballard, G. D. Wignall, G. Longman, and W. Schmatz, Polymer, **27**, 751 (1976).
34. T. P. Russell, J. S. Lin, S. Spooner and G. D. Wignall, J. Appl. Cryst. **21**, 629 (1988).
35. M. P. Grancio and D. J. Williams, J. Polym. Sci. (Al), **8**, 2617 (1970).
36. M. P. Wai, R. A. Gelman, M. G. Fatica, R. H. Hoerl and G. D. Wignall, Polymer, **28**, 918 (1987).
37. L. W. Fisher, S. M. Melpolder, J. M. O'Reilly, V. R. Ramakrishnan and G. D. Wignall, J. Colloid Interface Sci. **123**, 24 (1988).
38. J. W. Goodwin, R. H. Ottewill, N. M. Harris and J. Tabony, J. Colloid and Polym. Sci. **78**, 253 (1980); J. Colloid Interface Sci. **78**, 253 (1980).
39. K. Alexander, D. J. Cebula, J. W. Goodwin, R. H. Ottewill and A. Parentich, Colloids Surf. **7**, 233 (1983).
40. D. J. Cebula, J. W. Goodwin, R. H. Ottewill, G. Jenkin and J. Tabony, Colloid and Polym. Sci. **261**, 555 (1983); Discuss. Faraday Soc. **76**, 37 (1983).
41. Lord Rayleigh, Proc. R. Soc. London A. **84**, 24 (1911).
42. G. D. Wignall, V. R. Ramakrishnan, M. A. Linne, A. Klein, L. H. Sperling, M. P. Wai, R. A. Gelman, M. G. Fatica, R. H. Hoerl, L. W. Fisher, S. M. Melpolder and J. M. O'Reilly, Mol. Cryst. Liq. Cryst. **180A**, 25 (1990).
43. R. G. Alamo, J. D. Londono, L. Mandelkern, F. C. Stehling and G. D. Wignall, Macromolecules, **27**, 411 (1994).
44. G. D. Wignall, J. D. Londono, J. S. Lin, R. G. Alamo and L. Mandelkern, Macromolecules, **28**, 3156 (1995).
45. P. Debye and A. M. Bueche, J. Appl. Phys. **20**, 518 (1949).
46. P. Debye, H. R. Anderson and H. Brumberger, J. Appl. Phys. **28**, 679 (1957).
47. A. M. Fernandez, L. H. Sperling, and G. D. Wignall, Multicomponent Polymer Materials, ACS Advances in Chemistry Series 211 (1985).
48. T. P. Russell, Polym. Eng. Sci. **24**, 345 (1984).
49. Y. W. Cheung, R. S. Stein, J. S. Lin and G. D. Wignall, Macromolecules, **27**, 2520 (1994).
50. Y. W. Cheung, R. S. Stein, G. D. Wignall and H. E. Yang, Macromolecules, **26**, 5365 (1993).
51. G. D. Wignall, R. G. Alamo, J. D. Londono, J. S. Lin, L. Mandelkern, M. H. Kim and G. M. Brown, Macromolecules, **33**, 551–561 (2000).
52. G. D. Wignall, N. R. Farrar, and S. Morris, J. Mater. Sci. **25**, 69–77 (1990).
53. D. W. Marr *et al*., Macromolecules, **30**, 2120–2130 (1997).
54. W.-L. Wu, Polymer, **23**, 1907–1912 (1982).
55. A. B. Buckingham and H. G. E. Hentschel, J. Polym. Sci. Polym. Phys. Ed. **18**, 853 (1984).
56. F. S. Bates, G. D. Wignall and W. C. Koehler, Phys. Rev. Lett. **55**, 2425 (1985).
57. F. S. Bates and G. D. Wignall, Macromolecules **19**, 932 (1986).
58. F. S. Bates, M. Muthukumar, G. D. Wignall and L. J. Fetters, Macromolecules, **89**, 535 (1988); Macromolecules, **21**, 1086 (1988).
59. P. G. deGennes, Chapter 5 in Scaling Concepts in Polymer Physics, Cornell University Press, Ithaca (1979).
60. P. Debye, J. Appl. Phys. **15**, 338 (1944).
61. D. Schwahn, K. Hahn, J. Streib and T. Springer, J. Chem Phys. **93**, 8383 (1989).
62. A. Lapp, C. Picot and H. Benoit, Macromolecules, **18**, 2437 (1985).
63. F. S. Bates and G. D. Wignall, Phys. Rev. Lett. **57**, 1429 (1986).
64. F. S. Bates, S. B. Dierker and G. D. Wignall, Macromolecules, **19**, 1938 (1986).
65. J. D. Londono, A. H. Narten, G. D. Wignall, K. G. Honnell, E. T. Hsieh, T. W. Johnson and F. S. Bates, Macromolecules, **27**, 2864 (1994).
66. G. D. Wignall and F. S. Bates, J. Appl. Cryst. **20**, 28 (1987).
67. Applications of Neutron Scattering to Soft Condensed Matter (Edited by Barbara J. Gabrys), Gordon and Breach Science Publishers (2000).
68. J. M. O'Reilly, D. M. Teegarden and G. D. Wignall, Macromolecules **18**, 2747 (1985).
69. B. Crist and G. D. Wignall, J. Appl. Cryst. **21**, 701 (1988).